Electronic states in disordered topological insulators

Thesis by

Kun Woo Kim

In Partial Fulfillment of the Requirements

for the Degree of

Doctor of Philosophy

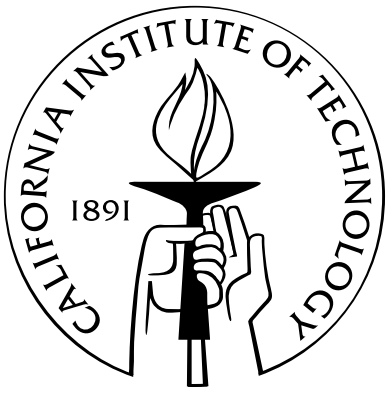

California Institute of Technology

Pasadena, California

2014

(Defended May 27, 2014)

Acknowledgements

I would like to thank my academic advisor Gil Refael. I took his course in 2010 spring which motivated me to pursue a Ph.D degree in condensed matter theory. During my study at Caltech, he has been very inspiring and supportive whenever I was stuck on various problems. I appreciate Tami Pereg-Barnea, Israel Klich, and Roger Mong for their mentorship. I was fortunate enough to work closely with them on different projects. I really enjoyed discussions with my fellow graduate students. Especially, I am grateful to Tony Lee, Tiamhock Tay, Paraj Titum, Shu-Ping Lee, Min-Feng Tu, Scott Geraedts, Karthik Seetharam, David Aasen, and Shankar Iyer. I also want to thank the brilliant postdocs at Caltech to whom I could ask random physics questions and they often supplied precise answers. In particular, I thank Andrew Essin, Torsten Karzig, Chang-Yu Hou, Eyal Kenig, David Pekker, Johannes Reuther, and Ling Wang. I want to thank my collaborators Alex Junck, Doron Bergman, and Marcel Franz whose input was very valuable. I would also like to thank Lesik Motrunich, Michael Cross, Oskar Painter, and David Hsieh for serving my thesis and oral candidacy committee, and Loly Ekmekjian for all her help over the years. Above all, I thank my father and mother for their tremendous love and encouragement for me to develop my own interests and dreams. I also thank my brother and extended families in Korea and California for their support.

Abstract

We present a theoretical study of electronic states in topological insulators with impurities. Chiral edge states in 2d topological insulators and helical surface states in 3d topological insulators show a robust transport against nonmagnetic impurities. Such a nontrivial character inspired physicists to come up with applications such as spintronic devices [1], thermoelectric materials [2], photovoltaics [3], and quantum computation [4]. Not only has it provided new opportunities from a practical point of view, but its theoretical study has deepened the understanding of the topological nature of condensed matter systems. However, experimental realizations of topological insulators have been challenging. For example, a 2d topological insulator fabricated in a HeTe quantum well structure by Konig et al. [5] shows a longitudinal conductance which is not well quantized and varies with temperature. 3d topological insulators such as Bi_2Se_3 and Bi_2Te_3 exhibit not only a signature of surface states, but they also show a bulk conduction [6]. The series of experiments motivated us to study the effects of impurities and coexisting bulk Fermi surface in topological insulators. We first address a single impurity problem in a topological insulator using a semiclassical approach. Then we study the conductance behavior of a disordered topological-metal strip where bulk modes are associated with the transport of edge modes via impurity scattering. We verify that the conduction through a chiral edge channel retains its topological signature, and we discovered that the transmission can be succinctly expressed in a closed form as a ratio of determinants of the bulk Green's function and impurity potentials. We fur-

ther study the transport of 1d systems which can be decomposed in terms of chiral modes. Lastly, the surface impurity effect on the local density of surface states over layers into the bulk is studied between weak and strong disorder strength limits.

Contents

Chapter 1

Introduction

Condensed matter in nature and laboratories shows rich phenomena that has intrigued generations of physicists. In the introduction, a non-technical survey of the field is introduced to invite general readers of physical science to experience its beauty and challenge. First, the main concept of a topological insulator and its exotic phenomena are introduced. Then, experimental probes identifying the signatures of topological insulators are surveyed in section 1.2. Furthermore, fascinating impurity-related behavior in physics is discussed in section 1.3 and the Green's function methods to deal with random potentials is presented in section 1.4. Lastly, we provide an overview of the thesis.

1.1 Insulators classified by Chern invariants

The purpose of this section is to introduce a topological insulator that has attracted enormous attention in the condensed matter community in the last decade. The important and inspiring concepts for understanding the specific studies presented in later chapters are explained in a qualitative manner, mainly in order to attract people in the field of physical science outside of condensed matter theory. Those who are more interested in further details are referred to the original papers cited in the bibliography.

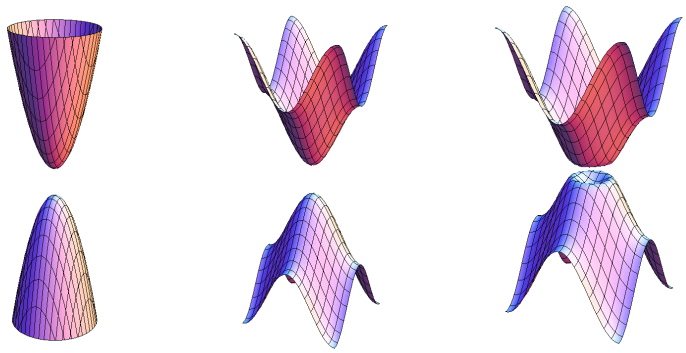

(a) (b) (c)

Figure 1.1: Vacuum as described by Dirac continuum Hamiltonian (a), Eq.(1.1), and band model on 2d lattice (b), Eq.(1.2) with $B > 0$. To generate the particle-antiparticle pair, a minimum energy $2mc^2$ is required corresponding to the energy gap between bands. The other insulating phase is described using the same 2d lattice model with $B < 0$ in (c).

1.1.1 'Topologically' different insulators

An insulator is a medium that cannot conduct charged particles. A vacuum is perhaps most the well-known insulator. The celebrated Dirac Hamiltonian describes the particle-antiparticle excitation in continuum space. For concreteness, let us consider the two-spatial dimension and spinless particle:

$$H = \begin{pmatrix} mc^2 & \hbar c(k_x - ik_y) \\ \hbar c(k_x + ik_y) & -mc^2 \end{pmatrix} \tag{1.1}$$

The vacuum is after all a two band model, as shown in Fig.1.1a. The minimum energy needed to create the particle and anti-particle pair is $2mc^2$, which is the energy gap between two bands. Let us put the vacuum on the lattice. A Hamiltonian of electrons on the 2d square lattice that can hop around the nearest neighbor sites is:

$$H = \begin{pmatrix} m + 2B[2 - cos(k_x a) - cos(k_y a)] & A[sin(k_x a) - isin(k_y a)] \\ A[sin(k_x a) + isin(k_y a)] & -m - 2B[2 - cos(k_x a) - cos(k_y a)]. \end{pmatrix} \tag{1.2}$$

Here the vacuum Hamiltonian acquired a little more structure in momentum space and regularized by introducing the lattice spacing a, which is the minimal step electrons can take on the lattice. For positive parameter A and B, we can see that the above two Hamiltonians essentially share the same feature of gapped bands up to microscopic details. The lattice Hamiltonian is more convenient to play with, since the discretization of the space enables us to use computational power. But the basis used here is electron-hole instead of particle-antiparticle in Dirac Hamiltonian. In fact, this shows one of the advantages of condensed matter systems: we can create a system that retains the same physics in nature but that has a different basis. This allows us to explore the fundemental physics in table-top experiments. Examples of such realizations include Majorana fermion [4], Dyon [7], magnetic mopole [8], and axions [9]. Recent developments of cold atom experiments offer other opportunities to probe more exotic phenomena in laboratories [10].

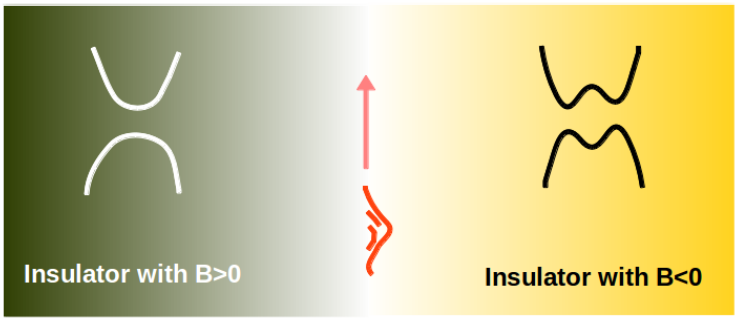

Figure 1.2: Two insulators on the 2d lattice model are positioned to interface each other. Interestingly, a single gapless mode appears within the energy gap at the interface.

A surprising behavior takes place when we put two insulators together with different signs of parameter B: one with $H(B > 0)$ and the other with $H(B < 0)$ (Fig.1.1b and Fig.1.1c). Each Hamiltonian maintains well-defined energy gaps. But when two are next to each other, a single gapless mode appears at the boundary. In other words, near the boundary it takes infinitesimally small amount of energy to create an electron-hole pair,

and therefore the system becomes metallic at the interface. Also, the appearance of the single chiral mode suggests that the electronic transport within the energy gap is robust against impurity scattering; an electron on that chiral mode has no other eigenstates to scatter into but itself. This is indeed the central interest of studying conduction through disordered topological insulator in Chapter 3. Lastly, such an appearance of the single chiral mode breaks time reversal symmetry: imagine we reverse the direction of time flow. Then the electron will flow in opposite direction and the original system will not be recovered under this symmetry transformation. This type of band insulator that exhibits a nonzero Hall conductance but preserves the lattice translational symmetry is called a Chern insulator. The topological insulator, which will be introduced soon, preserves the time-reversal symmetry, and retains a pair of chiral modes with different momentum and spins at the boundary.

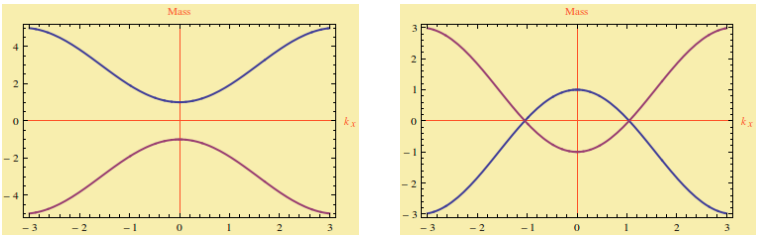

(a) (b)

Figure 1.3: Mass terms in the diagonal in Eq. (1.2) are plotted for $B > 0$ (left) and $B < 0$ (right) to explain the appearance of the gapless mode between two insulators.

Qualitative understanding of the appearance of the gapless chiral mode is followed by the band inversion model. Even though both systems are gapped with non-zero mass term in the diagonal parts of Hamiltonian, the sign of mass, $m + 2B[2 - cos(k_x a) - cos(k_y a)]$, differs for a range of momentum when $B < 0$ (see Fig.1.5b). Imagine that we bring the Hamiltonian from the left to right across the interface. The transition of Hamiltonian always accompanies the closing of the energy gap as the sign of mass term changes in the range

of momenta. For a more complete analysis from a similar perspective, see the study by Roger et al. [11]. This example introduces the topologically equivalent class of insulators: if one insulator can be transformed into the other insulator without closing the energy gap by local modification of the Hamiltonian, then we say the two insulators are topologically equivalent. If not, just as the example described above, they are topologically distinct. Directly following questions are, i) how many distinct topological insulators exist, and ii) whether we can look at the bulk instead of boundary to classify the topological character.

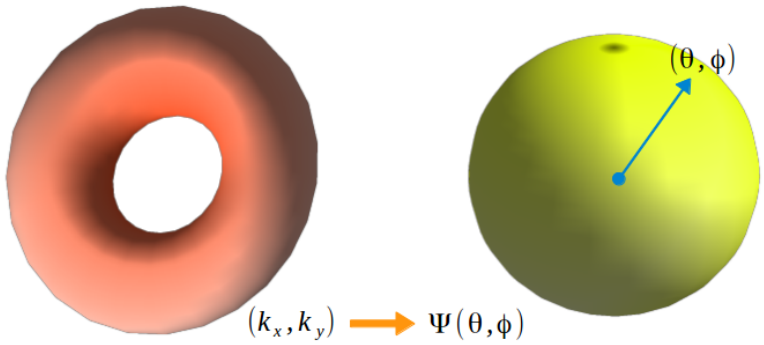

Figure 1.4: A two level system in 2d has a simpler interpretation of Chern invariants. Two complex components of a wave function can be parametrized by two angles, θ and ϕ. The torus on the left represents the Hilbert space where wave functions reside. The Chern invariant measures how many times the wave function vector wraps around the sphere as it moves over the whole surface of the torus.

The Chern invariant quantifies the concept of topology in the insulators. For a system with translation invariance, the Chern invariant of the j_{th} band is expressed in terms of the Bloch wave function, $u_j = u_j(k_x, k_y)$, of j_{th} band derivatives with respect to momentum k_x and k_y:

$$n_j = \int_{BZ} \frac{d^2k}{(2\pi)^2} \Omega^{(j)}_{k_x k_y} = \int_{BZ} \frac{d^2k}{(2\pi)^2} \left[\langle \frac{\partial u_j}{\partial k_x} | \frac{\partial u_j}{\partial k_y} \rangle - \langle \frac{\partial u_j}{\partial k_y} | \frac{\partial u_j}{\partial k_x} \rangle \right]. \tag{1.3}$$

The integrand of the right side is the local curvature of the Bloch wave function parametrized

by two momenta. For a spinless two level system, the wave function has two complex orbital components and it can be mapped on to a sphere up to an overall phase, just like a vector with three components (Figure 1.4). Then, the Chern invariant describes how many times the Bloch wave function vector wraps around the sphere as it is being integrated out in Brillouin zone, which is a torus for the 2-dimensional case. According to the remarkable relation made by Gauss and Bonnet, the integration of local curvature over a closed surface is always quantized, and this ensures that the Chern invariants are integer. For two insulators with different Chern invariants n_1 and n_2, there are $|n_1 - n_2|$ gapless chiral modes that appear at the boundary between them. This is called the bulk-boundary correspondence. We can figure out the Chern invariants of bulks by looking at the chiral modes at the boundary. This classification of insulator according to the integration of local curvature of Bloch wave function reminds us of our previous two-band toy model with $B > 0$ and $B < 0$. The sign change of mass term corresponds to the direction change of $\psi(\theta, \phi)$ on the sphere. This allows wave function to explore the whole surface of the sphere and the Chern invariant becomes nonzero for $B < 0$.

1.1.2 Z_2 classification of topological insulator

In 2005 Kane and Mele suggested a theoretical model of a topologically non-trivial insulator preserving the time-reversal symmetry [12]. They introduced a spin orbit coupling to the honeycomb graphene model to open an energy gap such that the Chern invariants of each spin section of the Hamiltonian are nonzero, but their sum is zero as required by the time reversal symmetry [13]. As a result, the Kane-Mele model abutted to a trivial insulator harbors two chiral gapless modes, one for each of the spins. Instead of the quantized charge Hall conductance, now the system possesses the quantized spin Hall conductance, and

physicists found its potential applications in spintronic devices [1], thermoelectric materials [2], photovoltaics [3], etc.

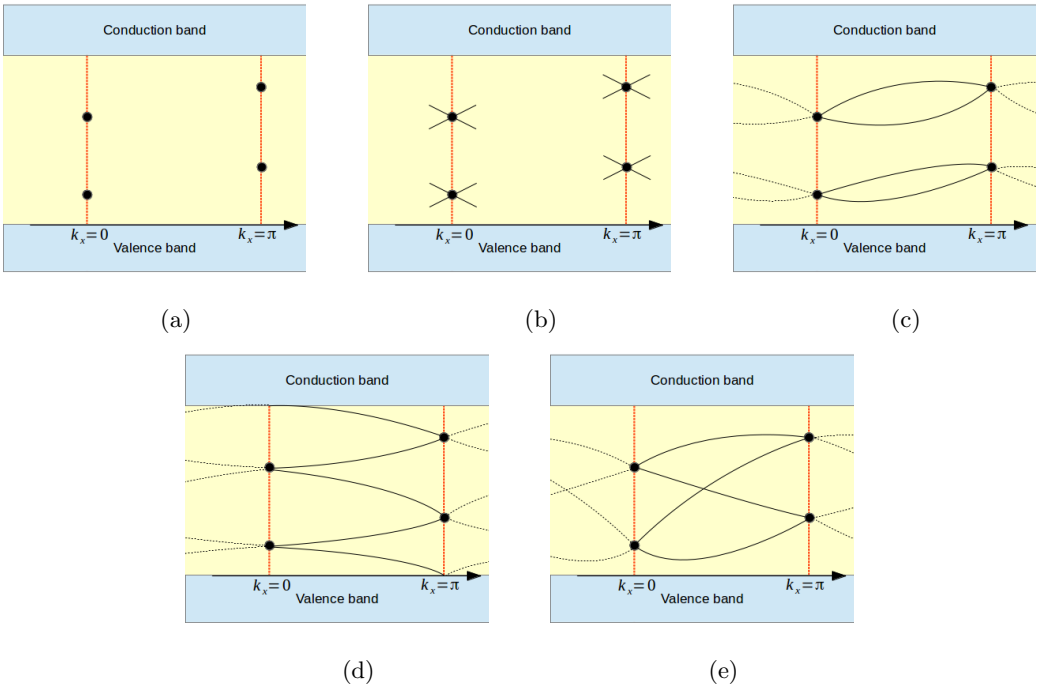

Figure 1.5: Z_2 classification of the topological insulator can be understood from the bulk-boundary correspondence. (a) shows the four Kammer pairs where the degeneracy of a state and its time-reversal copy are guaranteed. (b) Due to the spin-orbit coupling, two states split into different energies away from $k_x = 0$ and $k_x = \pi$. (c) One way to connect the states across the Brillouin zone is to connect pairwise. (d) The other way is to choose different partners, in this case the edge state is gapless. (e) There could be other pairings, but the pairing described is susceptible to local perturbation in respect to time-reversal symmetry and it is reduced to type (c) band.

The topological insulator has two inequivalent classes. Following Kane and Mele [14], we can find its explanation by appealing to the bulk-boundary correspondence: if we look what are possible configurations of edge states at the boundary, we know which are topologically distinct non-trivial bulk insulating phases. To proceed, consider an open boundary of the 2d topological insulator along x-direction and recall that in the projected band structure (k_x, E) the momentum $k_x = 0$ and $k_x = \pi/a$ are time reversal symmetric points in the Brillouin zone, so that a Bloch wave function and its time-reversal partner must be degenerated in

energy at the momenta 1.5. Away from those points, the energy bands are in general split due to the spin-orbit coupling. Now we have two options to connect a series of degenerated points at $k_x = 0$ and $k_x = \pi/a$: one is a zigzag type of connection from the valence to conduction band, Figure 1.5d, so that at every energy within the gap there is an odd number of pairs of time-reversal edge modes. The other option is to connect the Kramers degenerated points in pairwise manner so that there is an even number of time-reversal pairs at any energy within the gap. The first case yields a non-trivial spin Chern number and the second case corresponds to the trivial insulating phase. These two cases exhaust the inequivalent topological insulator classes in a 2d system, and therefore we say the classification is even or odd Z_2.

In the 3d case, we have more room to play as the number of time reversal symmetric points in the Brillouin zone is eight: $(k_x, k_y, k_z) = (\pi/2a \pm \pi/2a, \pi/2a \pm \pi/2a, \pi/2a \pm \pi/2a)$. Again, by appealing to the bulk-boundary correspondence, we can list what types of distinct connections of surface states are possible within the energy gap on the surface perpendicular to the z-axis, for example. Four time-reversal symmetric points are $(k_x, k_y) = (\pi/2a \pm \pi/2a, \pi/2a \pm \pi/2a)$, and Z_2 classification depends on the odd or even number of time-reversal pairs of surface states. The discovery of the 3d topological insulator came to physicists' surprise because its parents system, quantum Hall effect, was limited to the 2d system. Not only that, but the 3d topological insulator shows interesting phenomena not seen in its 2d counterpart that we will introduce in the following section.

1.1.3 Topological insulator phenomena

In this section, a few examples which have generated excitement and inspiration across the condensed matter community regarding the topological insulator are introduced.

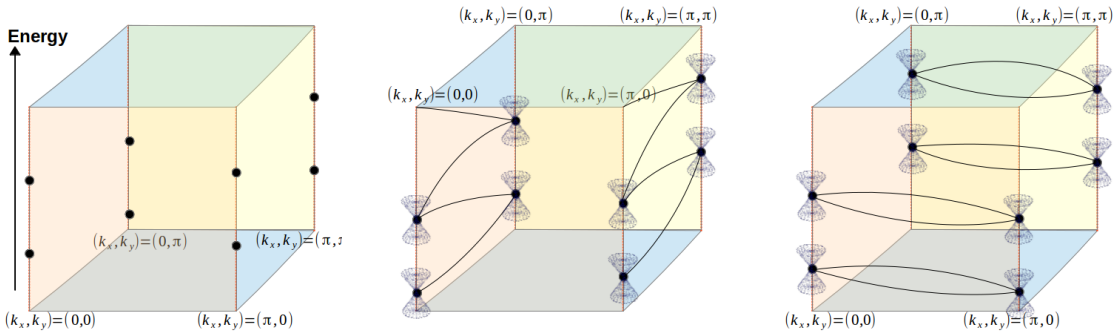

(a) (b) (c)

Figure 1.6: Z_2 classification of the 3d topological insulator can be understood in a similar manner to the bulk-boundary correspondence. Imagine we have an open boundary perpendicular to the z-axis, then surface states will be described in terms of (k_x, k_y) in clean system. (a) shows four points where a state and its time-reversal copy must be degenerated. Now we connect those four points to come up with different possibilities. (b) is the way we obtained the gapless edge state in the 2d system, and (c) leads trivial insulating phase in 2d. For 3d, we need to connect both directions along k_x and k_y. For example, if (b) and (c) are combined, we obtain a weak topological insulating phase where two Dirac surface states are present within the energy gap. If a (b)-type of connection is used for both directions, we get a strong topological insulator where a single Dirac surface state appears. A trivial insulating phase occurs when a (c)-type connection is used for both directions.

1. Magnetoelectric polarization: In solids, nuclear and bound electrons form an electric polarization under an external electric field to minimize electrostatic energy. Similarly, the effect of an external magnetic field applied to the orbital motion of bound electrons and magnetic polarization is induced. Surprisingly, in 3d the topological insulator the cross-correlated response occurs: the external electric field induces magnetization, while the external magnetic field leads electric polarization. This strange magnetoelectric response on the external fields takes place on the surface of the 3d topological insulator, and Essin et al.[15] clarified the relation of the magnetoelectric polarization and the non-trivial topological character of the system. Explicitly, they provided an alternative derivation of the Axion electrodynamics, $\Delta L_{EM} = (\theta e^2/2\pi h)\vec{E}\cdot\vec{B}$, as a contribution to magnetoelectric polarizability from extended orbitals.

2. Magnetic monopole: Paul Dirac showed that to have quantized electric charges,

magnetic monopoles should exist in the universe [16]. Here, the magnetic monopole which is not yet discovered is the source of the magnetic field, as the electric field is produced by electric charges. Qi, Li, et al. [17] suggested a system composed of a 3d topological insulator showing the effect of the image magnetic monopole. They considered a charge placed near the surface of the 3d topological insulator coated with thin magnetic film which gaps out surface states. Then, an image magnetic monopole as well as electric charge are induced to satisfy the boundary condition on the surface, when the effective field is observed outside the topological insulator. This phenomenon can be understood as magnetoelectric polarization: provided that the gapless surface states on the surface are gapped out so that the surface dynamics are dominated by the magnetoelectric coupling term, the electric field produced from the externally placed charge induces the Hall currents on the topological insulator surface in a circulating manner (see the inset of Figure 1.7a). As a result, the profile of the magnetic field just looks like a field generated from the point source in the topological insulator.

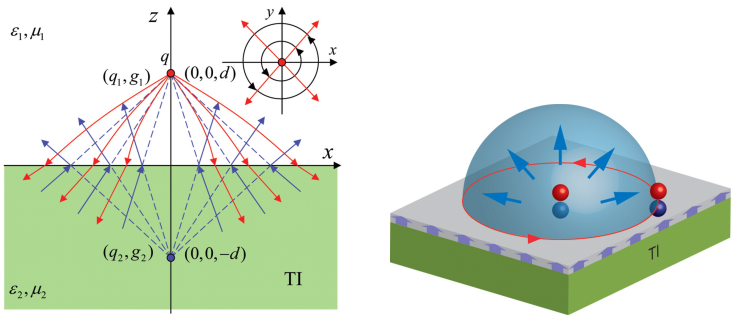

(a) (b)

Figure 1.7: An effective magnetic monopole is induced in a 3d topological insulator with a ferromagnetic coating on the surface. An external charge near the surface induces the Hall surface current that generates a magnetic field outside the topological insulator identical to the one generated by a magnetic monopole.

3. Witten effect: The exotic behavior of the topological insulator is also connected to

the fractionalization of charge. The Witten effect occurs when a unit magnetic monopole placed inside a topologically nontrivial medium with $\theta \neq 0$ is bound to a fractional electric charge $-e(\theta/2\pi + n)$ with integer n. The strong topological insulator serves as a medium of $\theta = \pi$. Rosenberg and Franz [9] prepared a magnetic monopole associate with a vortex in the exciton condensate emerging from the thin film of topological insulator with external bias. The fraction electric charge $Q = e/2$ associated with a magnetic monopole is observed using the exact diagonalization method in the lattice toy model. The other scheme of the charge fractionalization on graphene with a gap-opening term is proposed by Hou et al. [18].

4. Thermoelectric materials and photovoltaics: The applications of topological insulators to renewable energy research are particularly interesting since they may provide opportunities to break the limit of conventional materials. First, the topological insulators may be good thermoelectric materials [2] because non-magnetic impurities provide resistance to thermal transport in the system while electronic transport of edge states is not affected. Indeed, potential candidates for 3d topological insulators such as Bi_2Se_3 and Bi_2Te_3 have been used for thermoelectric engineering near room temperature for a long time [19]. On the other hand, solar cell application is another possibility where topological insulator can be useful. Lindner et al. [3] recently proposed to use topological insulator thin flims to harvest the infrared spectrum of the sun, which is unused in conventional band gap photovolataics. They pointed out that the observed surface photocurrent on topological insulator is low due to two symmetries: time-reversal and rotational symmetry. The time-reversal symmetry limits the system to absorbing circularly polarized light only, while the rotational symmetry means that the induced photocurrent has no preferred direction and therefore the net current is zero. Lindner et al. [3] proposed to put magnetic patterns on the surface

to break the two symmetries and computationally found the drastic increment of surface photocurrent.

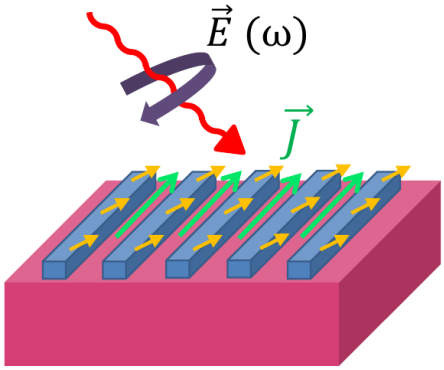

Figure 1.8: Lindner et al. [3] suggested putting a magnetic grating on the top of the topological insulator to produce a photocurrent by breaking the rotational symmetry and the time-reversal symmetry.

1.1.4 Physics at the edge

At the interface of a Chern insulator with Chern invariant n and a trivial insulator, n gapless modes appears according to the bulk-boundary correspondence. We say the chiral gapless edge modes at the boundary are robust against impurity scattering for a simple reason: every mode available to scatter into is propagating in the same direction. The relation between the quantized Hall conductance ne^2/h and the Chern invariant n of the system is established by Thouless, Kohmoto, Nightingale, and den Nijs in their seminal paper [20] in 1982 (see also section 1.3.2). This impurity-insensitive nature of transport along the boundary has captured physicists' interest, because it shows the universal quantization of conductance independent of microscopic details of devices. For the topological insulator, which is two copies of Chern insulators in time-reversal relation, there are two edge states within the energy gap and they are also time-reversal copies each other; if one edge mode is spin-up with momentum k, the other edge mode is spin-down with momentum $-k$.

Therefore, the transport is still robust against non-magnetic impurity, but a mobility gap appears in the presence of magnetic impurity. For the case of helical surface states in the 3d topological insulator, backscattering is not still allowed by non-magnetic impurities, but scatterings that deflect the direction of electron propagation lower its conductance. The transport of Dirac surface states with (non-)magnetic impurities is still an ongoing research topic [21, 22].

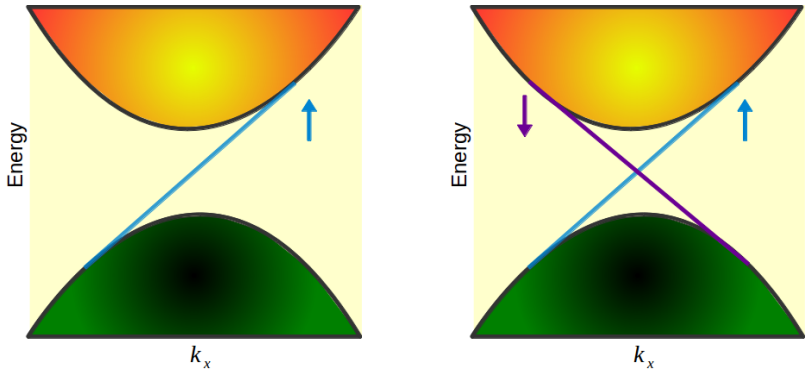

Figure 1.9: (a) a Chern insulator with a single gapless mode is shown. The edge mode is robust against impurity scatterings because there is only a single conducting mode which its own mode electrons can scatter into.(b) a topological insulator has two gapless modes in time-reversal relation. Two edge states cannot be coupled by non-magnetic impurities, while magnetic impurities can open a mobility gap.

The physics of chiral edge modes in quantum Hall systems and 2d topological insulators goes back to Tomonaga [23] and Luttinger [24], who suggested a quantum 1d model that cannot be explained by Landau's Fermi liquid theory, meaning that the picture of independent quasiparticles, which is in one-to-one correspondence with the bare electrons does not hold any longer. Significant progress has been made and the exact solution of a 1d system with interaction is found using bosonization (for the history of development, see Haldane [25]). The idea is to describe a fermion excitation in terms of bosonic languages for a system with a linear dispersion relation, $E(k) = vk$. By the Bogoliubov transformation,

1d interacting fermionic system is exactly mapped into a 1d free bosonic system for which we can derive physical observables using standard techniques. When the dispersion relation of Fermion system is not linear, it induces the coupling between bosonic excitation and mapped into interacting bosonic system [25]. The application of these theories successfully describes the dynamics of the edge excitation in fractional quantum Hall systems [26]. The tunneling conductance across an impurity in Luttinger liquid especially shows a power law scaling with temperature [27], as well as an analogous realization of Luttinger liquid in quantum Hall system with constrictions to allow scatterings between chiral modes, exhibits the universal behavior described by filling factors [26].

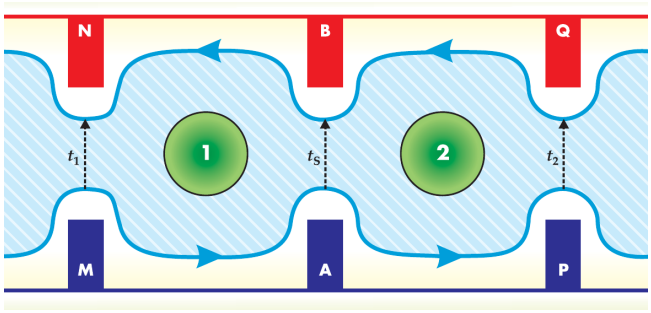

Figure 1.10: A quantum Hall interferometer suggested by Das Sarma et al. [28] is shown. Region 1 and 2 contain a number of quasiparticles that provide non-Abelian statistics for chiral edge states surrounding and tunneling between them. Three constrictions where top and bottom chiral edge states are brought close enough so that they can tunnel through are introduced to verify the braiding statistics in $\nu = 5/2$ quantum Hall system.

In practice, physicists manipulate and detect edge states in the quantum Hall system to identify the topological nature of bulks (recall the bulk-boundary correspondence). For instance, it has been theoretically suggested that the $\nu = 5/2$ quantum Hall phase contains non-Abelian statistics of quasiparticles, which makes it a strong candidate to realize a quantum computer using topologically protected qubits [29]. Das Sarma et al. [28] came up with a experimental scheme to verify the braiding statistics of $\nu = 5/2$ system through quasiparticle tunneling between chiral edge states. Here, the quasiparticle is an excitation

of the ground state. Though the Pfaffian state is assumed as a ground state in their proposal, its particle-hole conjugate state anti-Pfaffian is the other possible ground state possessing different types of quasiparticles as suggested by Lee et al. [30]. To resolve the confusion, Bishara et al. [31] et al. proposed other experiments predicting strikingly different interference patterns of edge modes depending on its ground state. Lastly, the effect of coupling between edge and bulk mode is considered by Halperin et al. [32] in the Febry-Perot quantum Hall interferometer to clarify the effect of fractional statistics as well as coulomb interactions and the Aharonov-Bohm effect. All these theoretical proposals show how edge states of exotic phases can be employed to characterize its topological nature and to build the units of unitary operations required for quantum computation.

1.2 Experimental probes of topological insulators

In this section, experimental methods to identify the signature of topological insulators are introduced, and it is impressive to follow how physicists came up with idea to identify the signature of topological insulator.

1.2.1 Transport measurements

1. Longitudinal and Hall (transverse) conductance measurement: As topological insulator harbors gapless excitations along the boundary with trivial insulator, the most direct identification of topological insulator will be the measurement of conductance with different sizes of systems. For a 2d system, the conductance through the chiral edge channel does not scale the with system width, while the conductance through the bulk channel, if present, does. Also, the presence of an energy gap can be probed by sweeping the chemical potential. The carrier of charges switches from hole to electron, so the Hall conductance

measurement will probe this change, and we can see if the system is insulating. Though this sounds straightforward, physicists have found it hard to see clear evidence of topological insulators from the longitudinal and Hall measurements. For instance, Konig et al. [5] performed the transport measurement on HgTe quantum wells, which is engineered to be 2d topological insulator, but the longitudinal conductance data shows not well-quantized and large temperature-dependent behavior. 3d topological insulators are no exception: the transport seems to be dominated by bulk conduction in Bi_2Te_3 and Bi_2Se_3 [6] due to the doping to place the Fermi level within the energy gap.

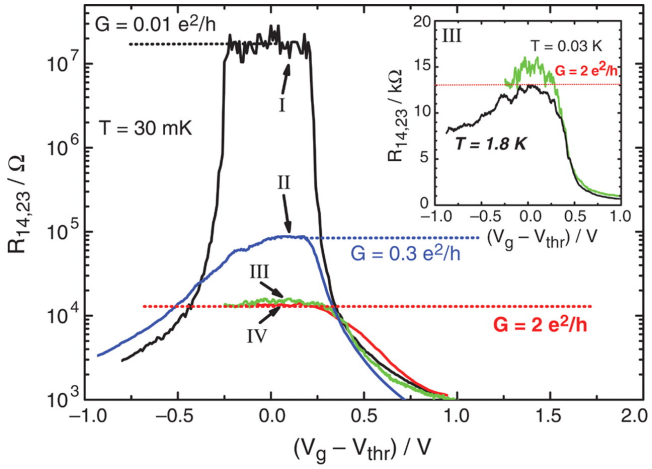

Figure 1.11: The longitudinal resistance [5] of not inverted (I) and inverted (II,III,IV) quantum well structures for different device sizes as a function of chemical potential is plotted. Though sample III shows relatively nice quantization of conductance at $2e^2/h$, it shows temperature-dependence behavior (inset).

2 Shubnikov-de-Haas oscillations measurement: In 3d topological insulator, as the transport is dominated by the bulk conduction channels, the direct longitudinal conductance measurement does not provide the definite signature of surface states. To circumvent the problem, physicists applied a strong magnetic field to the system and observed the oscillation of resistance with varying field strength. This behavior is due to the Landau quantization of electron energy levels under magnetic field. From the semiclassical point of view, free

electrons in the system undergo a circular orbiting motion and behave like simple harmonic oscillators. Their energy levels are now quantized by cyclotron frequency, and they form highly degenerate energy bands at $E_n = (n + 1/2)\hbar w_c$. As the magnetic field increases, the greater number of states that occupy a single Landau level, while at the same time the spacing between Landau levels widens. The conductance shows an oscillatory behavior as each Landau level passes through the Fermi level. Once all electrons are degenerated in the lowest Landau level, the conductance shows no more oscillations. This is why the area of the Fermi surface S is directly related to the oscillation of conductance. This is the famous Onsager's relation: $\Delta(1/B) = 2\pi e/\hbar cS$. Analytis and his colleagues [33] fabricated a sample which shows relatively weak oscillation, meaning that the bulk Fermi surface is small, and they measured the longitudinal and Hall resistance at different angles between the magnetic field and the surface of the sample. Any change of conductance as changing the angle is the signature of surface states because bulk electrons are not sensitive to the direction of the magnetic field.

3. Aharonov-Bohm interference: Another clever way to bypass the influence of bulk conduction is suggested by Peng and his colleagues [34], and uses magnetic flux through the 3d topological insulator wire. When an electron completes a closed orbit enclosing a magnetic flux Φ, it picks up a phase $\Delta\phi = (e/\hbar)\Phi$. The phase can be shown in conduction measurement by preparing a pair of coherent electrons going through different paths that meet at the end. The electrons may constructively or destructively interfere depending on the magnetic flux enclosed by their paths. The superconducting quantum interference device is indeed the device to measure a very small change of magnetic flux change through the ring of superconductors [35]. The same concept is employed to see the signature of surface states in 3d topological insulators. Imagine a magnetic flux is inserted through a

wire for which we want to check whether surface states exist along the boundary of the wire. For bulk states which most likely coexist with surface states, the resistance will show aperiodic behavior with the magnetic field since the bulk electrons do not have a well-defined cross section of the closed path perpendicular to the magnetic field. On the other hand, the surface states enclose the cross section of the wire since they always move on the boundary of the wire, and therefore their contribution to resistance will be periodic with varying magnetic field strength. Indeed, Peng et al. observed the oscillation of resistance with period of magnetic field $\Delta B = h/eA$, where A is the cross-section of the wire. The corresponding magnetic flux change $\Delta\Phi = h/e$ confirms the interference of surface states around the boundary of the wire.

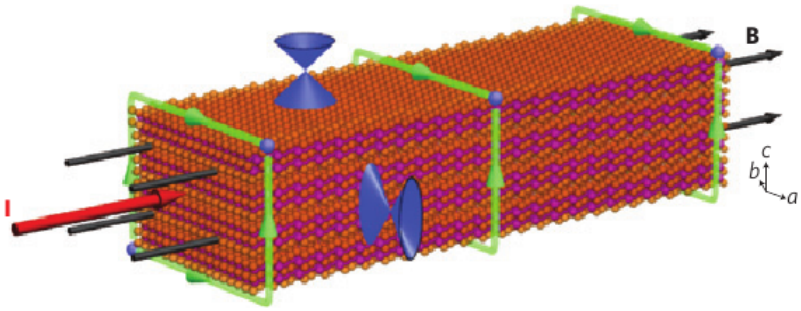

Figure 1.12: Surface states on 3d topological insulator wire enclose magnetic flux of a fixed cross-sectional area [34]. Therefore, it shows a periodic conductance change upon the change of magnetic field strength according to the Aharonov-Bohm interference effect. On the other hand, bulk states show aperiodic behavior as the cross-section is not well defined.

1.2.2 Local density of states measurements

1. Spin Angle-resolved photoemission spectroscopy (spin-ARPES): An observation of the local density of states near the surface is one of the most direct confirmations of the presence of helical surface states and the identification of topological insulators. As opposed to the transport measurement where Fermi energy should be placed within the energy gap, this

photoemission technique can probe the system and map its local density of states without doping first. Therefore, it has advantages at probing potential candidates of topological insulators regardless of its initial chemical potential. ARPES can measure the momentum vector of photo-excited electrons and therefore the reconstruction of local density of states in momentum space is available, which provides a unique opportunity to verify the Dirac dispersion relation of surface states. Furthermore, spin-ARPES [36] can resolve the spin texture of the Dirac dispersion curve, and it allows us to identify the topological nature of the system. This advanced technique certainly helped our understanding of the family of 3d topological insulators, but in the presence of impurities the local density of state is not straightforwardly translated into the conductance through surface channels. For instance, weak magnetic impurities that locally couple the time-reversal states may open the mobility gap, but not the spectral energy gap. And the transition of transport nature between the mott insulating phase and the ballistic conducting phase is not obvious from ARPES data. This is our motivation to study in Chapter 5 the surface impurity effect on surface states.

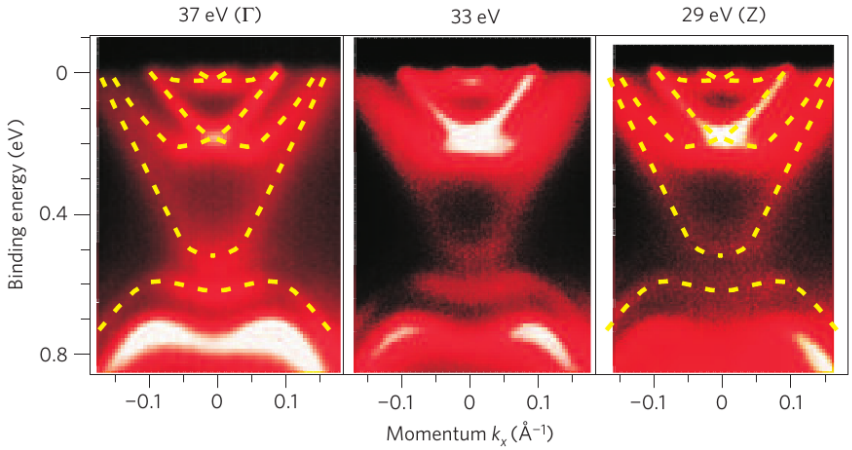

Figure 1.13: ARPES data by Wray et al. [37] showing Dirac surface states modified by the deposition of iron on the surface. Incident photon energy is changed so that it probes a cross-section of dispersion at different k_z along Γ point to Z point in the Brillouin zone. As the spectrum shows no dispersive relation along k_z, the series of ARPES shows the verification of the surface states.

2. Scanning tunneling microscope (STM): STM provides the counterpart of the local density of states in real space instead of in momentum space. This sophisticated apparatus has a very sharp nano-scale tip that can carry a current to a system in atomic resolution through quantum tunneling. By measuring the local current as a function of chemical potential over the surface of the sample, for example, Zhang et al.[38] obtained beautiful pictures of the local density of surface states in 3d topological insulator, Bi_2Te_3. On the other hand, STM can characterize scattering channels near impurities from the Fourier transformation of the local density of surface states in real space. Zhang and his colleagues introduced non-magnetic Ag trimmers, which sit right on the top of Te sites of Bi_2Te_3, and then they observed that the momentum transfer spectrum carried by the impurity shows anisotropic behavior: Among three dominant channels of warped Fermi surface, only one is visible, implying that the backscattering channel and the other channel are suppressed. Although the suppression of the latter channel needs more analysis[39], the disappearance of backscattering momentum transfer is consistent with the time-reversal protection of surface states in topological insulator.

1.3 Impurity related novel physics: Phenomena

Impurities are always present in condensed matter systems, and in most cases experimentalists have only limited control over the type of unwanted impurities and their concentration. This is one practical reason for why we want to develop theoretical frameworks predicting the effect of impurities. On the other hand, physicists discovered novel phenomena emerging through the scatterings due to impurities in systems (Examples include the Kondo effect, the quantum Hall effect, the universal conductance fluctuation, the impurity-induced phase transition, etc.). In this section, to attract readers' interest towards impurity-induced phe-

nomena, we will briefly discuss the role of impurities in the selected examples.

1.3.1 The Kondo effect

From the classical point of view, the motion of free electrons in metal is altered by the thermal vibration of the lattice. Thus, one would expect a system at lower temperature to show smaller electrical resistivity. Therefore, a strange behavior of resistivity was observed in the presence of magnetic impurities: the resistance of gold increases with lowering temperature [40]. Later, this non-trivial behavior was first explained by Kondo in 1964 [41]. Kondo explained that the interaction between conduction electrons and an electron localized around magnetic impurity forms a resonant scattering channel, which becomes stronger at lower temperatures as thermal fluctuation is reduced. Such a magnetic impurity resonant scattering channel provides conduction electrons another option to backscatter, and the resistance of the system increases with lowering temperature.

How can conduction electrons at Fermi energy interact with magnetic impurity bound state at different energy? The resonant scattering is made possible through the exchange process and Heisenberg's uncertainty principle. Imagine that a bound electron in the magnetic impurity jumps out to the conduction band. Though such a process is not allowed in a classical viewpoint, as it violates conservation of energy, if an electron in the conduction band jumps into the bound state within a short time, then the exchange process is possible within the uncertainty of energy. The state between the transition is called the virtual state. A remarkable scaling behavior [42] follows that the resistance normalized by the resistance at zero temperature is a function of the ratio of temperature normalized by the Kondo temperature, which is the onset of the Kondo effect. This scaling behavior, $R/R_0 = f(T/T_K)$, was first suggested by Anderson [43] and then confirmed by Wilson in

1974 [44] by the numerical renormalization group method.

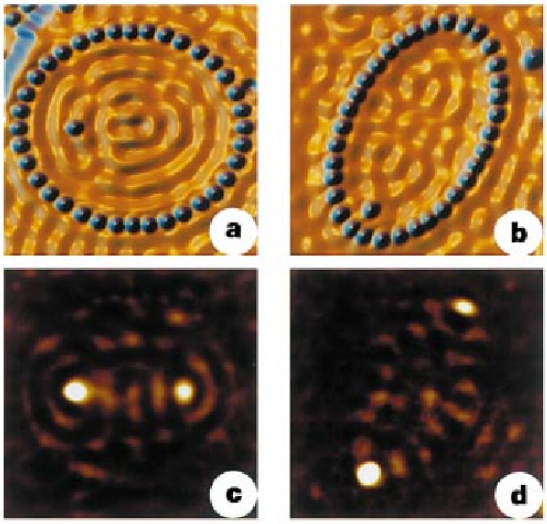

Figure 1.14: Using a scanning tunneling microscope, Manoharan et al. [45] constructed a quantum mirage made out of Cu atoms following the circumference of the ellipse and a magnetic impurity, Cobalt atom, is placed at one focal point. They observed the Kondo resonance not only at the Cobalt atom, but also at the other focal point, as shown in picture (c) and (d) above. The appearance of the image resonance confirms the interaction between conduction electrons and a magnetic bound electron.

Significant advances in nano-scale fabrication in the 1990s gave physicists extensive capabilities to control quantum tunneling strength, electron interaction in the magnetic impurity, magnetic bound state energy, etc. Quantum mirage [46] is one interesting example showing the Kondo effect and demonstrating its underlying mechanism of interaction between conduction electrons and a magnetic impurity bound state. Using a scanning tunneling microscope, Manoharan et al. [45] placed non-magnetic impurities on the circumference of ellipse 1.14, and put a (magnetic) Cobalt atom on one of the ellipse focal points. Interestingly, they found the Kondo resonance at the second ellipse focal point as well as at the Cobalt atom. The conduction electrons emitted from the STM tip at the second focal point are gathered on the Cobalt atom after being scattered at the circumference on the ellipse. Therefore, the Kondo resonance at the second focal point occurs through the magnetic im-

purity at the first focal point, and this directly supports the role of the conduction electron and the magnetic impurity discussed above.

1.3.2 Integer quantum Hall effect

Extremely well-quantized values of Hall conductance were observed under a strong magnetic field in a 2d electron gas system in 1981 by von Klitzing [47]. This robust phenomenon is independent of microscopic details including device size, precise location of Hall voltage probes, purity of the sample, value of the magnetic field, etc. This observation intrigued and inspired physicists to develop a new paradigm in condensed matter physics, topological order of matter. The robustness is in one sense related to the scaling of the resistance, $R = \rho L^{2-d}$, where ρ is resistivity, L is system size, and d is dimension. Resistance R becomes independent of system size for $d = 2$. But there are other players necessary in order to see the quantized values.

Imagine a translationally invariant system under magnetic field. One can find that the Hall resistivity of the system has to be linearly proportional to the magnetic field. This is from the following reason: consider a frame moving with a relative velocity v with respect to the original lab frame. In this moving frame, the electric field is present by Einstein's special relativity ($\vec{E} = \vec{B} \times \vec{v}/c$), and the rest of the electrons in the lab frame carry a current. Therefore, one directly discovers a Hall resistivity linearly proportional to the B-field. This is the first reason why we need disorders in the system to break the translational invariant.

More strikingly, without disorder we cannot observe energy gaps in thermodynamic limit as the external magnetic field is what we change in the actual experiments. Here is a simple argument: the number of edge modes between Landau levels is proportional to system dimension L, since the number of lattice points along the edge is what the edge state

is made out of. On the other hand, the number of bulk states is proportional to L^2. This means that whenever you try to observe some states as varying magnetic fields, the chance to observe edge states converges to zero relatively. This is why we need disorders localizing bulk states, so that they fill the energy gap between Landau levels. For a relatively clean system, one can find more plateaus at fractional filling factors. This unexpected energy gap opening due to electron-electron interaction at rational filling factor is called the fraction quantum Hall effect.

From the linear response theory, the Hall conductivity of a system is a velocity-velocity correlation. This is because the external electric field E_x can be represented as a velocity v_x, as it induces the flow of particles in a parallel direction, and the Hall current J_y, which we want to measure, is represented as a velocity v_y.

$$\sigma_{xy} = \frac{ie^2}{\hbar A} \sum_{n<0, m>0} \frac{(v_x)_{nm}(v_y)_{mn} - (v_y)_{mn}(v_x)_{nm}}{(E_n - E_m)^2} \tag{1.4}$$

where A is the area of the system, and we assume the Fermi energy $E_F = 0$. $(v_x)_{nm} = \langle \psi_n | \hat{v}_x | \psi_m \rangle$ is the velocity operator along x is sandwiched by eigenstate n and m. Though the above expression is commonly manipulated in momentum space (k_x, k_y) leading to a local curvature of Bloch wave functions parametrized by two momenta in the Brillouin zone, such an approach simply neglects the presence of disorders breaking translational invariance, and therefore it does not accurately describe the quantum Hall system. Niu, Thouless, and Wu [48] came up with a similar line of thinking that supports the quantization of Hall conductivity robust in the presence of disorders and particle interactions. Let us directly get to the essence of their argument.

Imagine a Hamiltonian containing disorders, periodic potentials, and coulomb interac-

tion:

$$\hat{H} = \sum_{i=1}^{N} \left[\frac{1}{2m_i} \left(-i\hbar\partial_{x_i}\right)^2 + \frac{1}{2m_i} \left(-i\hbar\partial_{y_i} - eBx_i\right)^2 \right] + \sum_i U(x_i, y_i) + \sum_{i,j} V(|\vec{r}_i - \vec{r}_j|) \quad (1.5)$$

where the terms in the square bracket account for kinetic energy under the magnetic field, the third term, $U(x_i, y_i)$ is random onsite potential, and the last term is coulomb interaction. Consider a many-body eigenstate $\psi_n = \psi_n(x_1, \cdots, x_N, y_1, \cdots, y_N)$ with eigenenergy E_n. To compute Hall conductance, we need a (n, m) component of velocity operator $\langle\psi_n|\hat{v}_x|\psi_m\rangle$ in many-body eigenstates basis. For a clean system with translational invariance, we can use the Bloch wave function $u_{n,k}(x, y) = e^{-i(k_x x + k_y y)}\psi_n(x, y)$. Then we compute the velocity operator $\hat{v}_x = \frac{\partial \tilde{H}}{\partial k_x}$ for a transformed Hamiltonian $\tilde{H} = e^{-i\vec{k}\cdot\vec{r}}\hat{H}_k e^{i\vec{k}\cdot\vec{r}}$. An exactly identical operation is repeated for the system with disorder and particle interaction, but this time we introduce a twisted boundary condition to the many-body wave function instead of momenta:

$$\Phi_n = e^{-i\theta(x_1+\cdots+x_N)/L_x - i\phi(y_1+\cdots+y_N)/L_y}\psi_n \quad (1.6)$$

$$\tilde{H}_{\theta,\phi} = e^{-i\theta\sum_j x_j/L_x - i\phi\sum_j y_j/L_y}\hat{H}e^{i\theta\sum_j x_j/L_x + i\phi\sum_j y_j/L_y} \quad (1.7)$$

where L_x and L_y are system dimensions, and θ and ϕ are parameters determining the boundary condition. Note that the wave function Φ_n is periodic upon the change of θ and ϕ by 2π. The velocity operators are the derivatives of the transformed Hamiltonian with respect to θ and ϕ, just like they are obtained from k_x and k_y in a clean system: $\hat{v}_x = L_x\frac{\partial \tilde{H}}{\partial \theta}$ and $\hat{v}_y = L_y\frac{\partial \tilde{H}}{\partial \phi}$. Next, using the relation $\langle\Phi_n|\frac{\partial \tilde{H}}{\partial \theta}|\Phi_m\rangle = (E_m - E_n)\langle\frac{\partial \Phi_m}{\partial \theta}|\Phi_n\rangle$, the Hall

conductivity relation is reduced:

$$\sigma_{xy} = \frac{ie^2}{\hbar}\sum_n \left[\langle\frac{\partial\Phi_n}{\partial\theta}|\frac{\partial\Phi_n}{\partial\phi}\rangle - \langle\frac{\partial\Phi_n}{\partial\phi}|\frac{\partial\Phi_n}{\partial\theta}\rangle\right] \tag{1.8}$$

Finally, we argue that the Hall conductivity which is bulk property is insensitive to the choice of boundary condition characterized by θ and ϕ. As a result, we come up with the Hall conductance expression which is geometrically quantized by averaging out the above Hall conductivity for a different boundary condition θ and ϕ :

$$\sigma_{xy} = \frac{e^2}{h}\sum_n \int_0^{2\pi} d\theta \int_0^{2\pi} d\phi \frac{1}{2\pi i}\left[\langle\frac{\partial\Phi_n}{\partial\phi}|\frac{\partial\Phi_n}{\partial\theta}\rangle - \langle\frac{\partial\Phi_n}{\partial\theta}|\frac{\partial\Phi_n}{\partial\phi}\rangle\right], \tag{1.9}$$

which is an integer multiple of conductance unit e^2/h (see Eq. (1.3)). The integrand on the right side is the local curvature of the many-body wave function parametrized by θ and ϕ, and the integration is over the torus as before.

1.3.3 Metal-insulator transition

When an electron is moving through a lattice, from the classical mechanical point of view it encounters "moguls" of atomic potentials. It seems that the mean free path along which the electron can propagate without collision is in the scale of lattice spacing. Undergoing so many collisions through the lattice, how a metallic phase where electrons are treated as free and independent can be possible. Felix Bloch in 1928 discovered that electron wave function in periodic potential can be expressed just like a plane wave in free space, but with periodic modulation of its amplitude. This is called Bloch wave function. Now a qualitatively opposite question arises: what is the origin of the electronic resistance? This is the starting point of the classical theory of electronic transport that accounts for the

thermal vibration of lattice and impurities scatterings.

A genuinely remarkable phenomenon happens when the electronic coherence length is maintained over many mean free paths. The conductance of 1d and 2d systems drops to zero as soon as impurities are introduced on the lattice in the thermodynamic limit at zero temperature. In 3d, an analogous electronic localization takes place, but at a finite critical impurity strength at which the conductance of system is e^2/h. In the classical transport viewpoint, weak impurities do not change the electronic density of states, and therefore the tranport of electrons in a diffusive manner should allow non-zero conductivity. Since Philip Anderson [43] first numerically showed this puzzling behavior in 1958, physicists took this challenge and made extensive progress from analytical and computational perspectives. This is called Anderson localization.

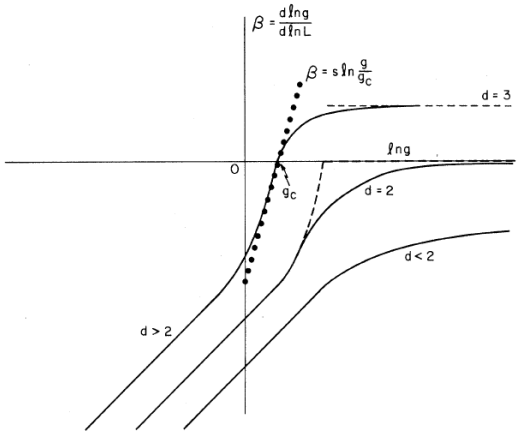

Figure 1.15: The scaling of conductance [49] with a system size for different spatial dimensions is shown. A negative $\beta = d(\ln g)/d(\ln L)$ means the conductance decreases with increasing system size: insulating phase. While a positive β means increasing conductance with system size, and a system ends up into metallic phase in the thermodynamic limit. Strikingly, the above scaling picture suggests a system in dimension $d = 1, 2$ is always insulating.

To understand how this is possible, we can appeal to the wave-like nature of electrons on lattice. Suppose we want to compute the probability of an electron moving from one to

another. We simply sum up the amplitude of all possible paths, and then take the square of the magnitude. In the presence of impurity, the phase correlation between different paths is not maintained due to the impurity scatterings, and the summation of those amplitudes vanishes on average. However, consider the probability of an electron coming back to its original location. One path and its time-reversal copy will maintain the same phase, provided that impurity potentials respect the time-reversal symmetry, nonmagnetic. As a result, we obtain double the chance of observing the electron in its original location, as opposed to the probability computed from the classical point of view which ignores the quantum interference effect. Though the field theoretic path integral approach provides qualitative hints, the summation of relevant diagrams shows divergence and the perturbative approach does not work. To this end, a self-consistent treatment is suggested by [50] that solves the problem in the thermodynamics limit. Impurity-related phenomena pose challenges, and it is truly inspiring to observe the development of analytical approaches by physicists to study impurity-related phenomena. Examples include the random matrix theory [51], the non-linear sigma model [22], supersymmetric approach [52], etc.

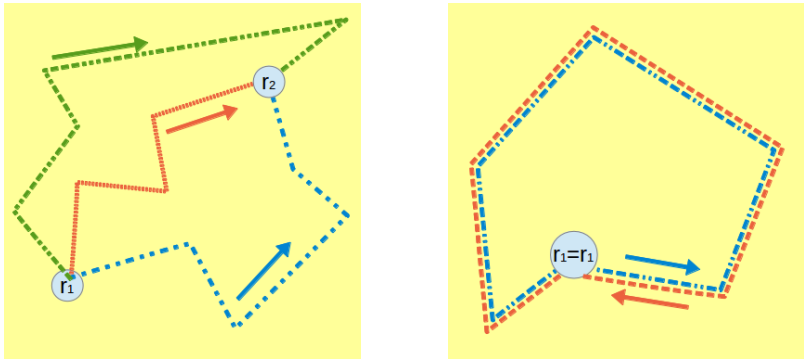

(a) (b)

Figure 1.16: A propagation of electrons from the location r_1 to r_2 through impurity scatterings. (a) When $r_1 \neq r_2$, different routes have an uncorrelated phase relationship and the summation of amplitudes is zero on average. (b) When the time-reversal symmetry is preserved in the system, a route and its time-reversal path pick up the same phase and it enhances the probability for electron to stay at the same location.

In connection to topological insulator possessing chiral edge states or surface states without backscatterings, it is one of the central questions that how these topologically protected states behave in the presence of non-magnetic and magnetic impurities. Moreover, as 3d topological insulators may contain unexpected bulk modes [53] from doping to shift the Fermi energy, how the conventional picture of the Anderson localization applies to the system with helical surface states as well as bulk modes and impurities is a question awaiting resolution. Lastly, physicists numerically found that a trivial insulator can undergo a phase transition into a topological insulator by introducing impurities that renormalize the chemical potential as well as the mass term of the Hamiltonian. The Landauer-Buttiker type conductance calculation shows a well-quantized chiral edge transport in 2d system [54], and for the 3d case by Guo, Resenberg et al.[55] the appearance of a strong topological insulating phase is verified in terms of quantized conductance and the Witten effect.

1.4 How to study disordered systems: Theory

In this section, we survey the Green's function formulation to describe the evolution wave functions in the presence of disorder potentials. The Green's function directly provides physically relevant quantities such as the density of states and the correlation functions. The self-consistent treatment of Green's function is discussed in section 1.4.1, as well as its application to an isotropic impurity, for which the exact analytic expression is available in section 1.4.2. Lastly, disorder averaging technique that allows us to evaluate thermodynamic quantities by sampling all possible configurations of impurities is introduced in section 1.4.3

.

1.4.1 Propagator of wave function: Green's function

Imagine an eigenstate $|x,t\rangle$ in a system characterized by Hamiltonian $\hat{H} = \hat{H}_0 + \hat{V}$:

$$\left[i\hbar\frac{\partial}{\partial t} - \hat{H}_0 - \hat{V} \right] |x,t\rangle = 0. \tag{1.10}$$

For our purpose, we can think of $\hat{H}_0$ as a Hamiltonian of a clean condensed matter system and $\hat{V}$ as an impurity potential operator. A wave function $\psi(x',t') = \langle x',t'|\psi\rangle$ at time t and location x can be related to the other wave function $\psi(x,t) = \langle x,t|\psi\rangle$ at different coordinate by inserting the identity operator $\hat{I} = \int dx|x,t\rangle\langle x,t|$:

$$\begin{aligned} \langle x',t'|\psi\rangle &= \int dx\langle x',t'|x,t\rangle\langle x,t|\psi\rangle & (1.11)\\ &= \int dx G(x',t';x,t)\langle x,t|\psi\rangle, & (1.12) \end{aligned}$$

where the propagator or the Green's function $G(x',t';x,t) = \langle x',t'|x,t\rangle$ is introduced, and which propagates the wave function in space and time. As we are interested in the physics of time in one direction, we assume $t' > t$. In this case, the propagator is called a retarded Green's function, and describes the physics in accordance with causality.

Evolution operator in time, $\hat{U}(t',t)$, is:

$$\langle x',t'|x,t\rangle = \langle x'|\hat{U}(t',t)|x\rangle \tag{1.13}$$

The expression of evolution operator in terms of Hamiltonian can be obtained by solving

the Schrodinger equation perturbatively:

$$\begin{aligned}
|\psi(t')\rangle &= \hat{U}(t',t)|\psi(t)\rangle \\
&= \sum_{n=0}^{\infty}\left(\frac{1}{i\hbar}\right)^n \int_t^{t'} dt_n \int_t^{t_n} dt_{n-1}\cdots\int_t^{t_2} dt_1 \hat{H}(t_n)\cdots\hat{H}(t_1)|\psi(t)\rangle \\
&= \sum_{n=0}^{\infty}\frac{1}{n!}\left(\frac{1}{i\hbar}\right)^n \int_t^{t'} dt_n \int_t^{t'} dt_{n-1}\cdots\int_t^{t'} dt_1 \hat{T}\left[\hat{H}(t_n)\cdots\hat{H}(t_1)\right]|\psi(t)\rangle \\
&= \hat{T}\left[exp\left(\frac{1}{i\hbar}\int_t^{t'} d\bar{t}\hat{H}(\bar{t})\right)\right]|\psi(t)\rangle \qquad (1.14)
\end{aligned}$$

where the summation of all orders of Hamiltonian is captured by the exponential function, with time-ordering operator $\hat{T}$ ensuring the operator at earlier time to be applied first to the wave function. This is a very nice formulation, but most of the time we know what the eigenstates of a clean Hamiltonian $\hat{H}_0$ are, and our main interest is to figure out corrections caused by disorder potential $\hat{V}$.

In the same spirit of the Bloch theorem, the unitary transformation of eigenstates can eliminate the clean Hamiltonian $\hat{H}_0$. Consider the same Schrodinger equation relation, but using a different basis: $|x,t\rangle = exp\left(\frac{1}{i\hbar}\hat{H}_0 t\right)|x,t\rangle_0$:

$$\begin{aligned}
0 &= \left[i\hbar\frac{\partial}{\partial t} - \hat{H}_0 - \hat{V}\right] e^{\frac{1}{i\hbar}\hat{H}_0 t}|x,t\rangle_0 \qquad (1.15) \\
&= e^{\frac{1}{i\hbar}\hat{H}_0 t}\left[i\hbar\frac{\partial}{\partial t} - \hat{V}_I\right]|x,t\rangle_0 \qquad (1.16)
\end{aligned}$$

where we introduce $\hat{V}_I = e^{-\frac{1}{i\hbar}\hat{H}_0 t}\hat{V}e^{\frac{1}{i\hbar}\hat{H}_0 t}$, and the notation $|\rangle_0$ indicates that we are in the eigenbasis of a clean Hamiltonian $\hat{H}_0$. In this new basis, we immediately find that the clean Hamiltonian is absent and that instead the unitary transformed disorder potential $\hat{V}_I$ is the only term present. This is called an interaction picture. This reminds us that the Bloch theorem eliminates the periodic potential in the crystal momentum basis, and that

the Bloch wave function is simply plane waves with the modulation of amplitude. We can repeat the previous perturbation approach to evaluate the evolution operator in a clean eigenstate basis. As a result:

$$|\psi(t')\rangle_0 = \hat{T}\left[exp\left(\frac{1}{i\hbar}\int_t^{t'} d\bar{t}\hat{V}_I(\bar{t})\right)\right]|\psi(t)\rangle_0, \tag{1.17}$$

which provides the perturbative corrections due to disorder potential in the basis of clean system eigenstates.

Equipped as we are with the evolution operator, now let us go back to the Green's function and see how it changes by disorder potential:

$$G(x',t';x,t) = \langle x'|\hat{T}\left[exp\left(\frac{1}{i\hbar}\int_t^{t'} d\bar{t}\hat{H}(\bar{t})\right)\right]|x\rangle, \tag{1.18}$$

$$= {}_0\langle x',t'|\hat{T}\left[exp\left(\frac{1}{i\hbar}\int_t^{t'} d\bar{t}\hat{V}_I(\bar{t})\right)\right]|x,t\rangle_0. \tag{1.19}$$

By expanding the exponential function term by term, we come up with the following self-consistent expression:

$$G(x',t';x,t) = G_0(x',t';x,t) + \frac{1}{\hbar}\int d\bar{x}\int d\bar{t}G_0(x',t';\bar{x},\bar{t})V(\bar{x},\bar{t})G(\bar{x},\bar{t};x,t). \tag{1.20}$$

where $G_0(x',t';x,t)$ is the Green's function in clean system $\hat{H}_0$, and all orders of corrections can be obtained recursively.

Lastly, let us discuss the Green's function in momentum and energy space. The representation in space and time provides the propagation of a particle picture more familiar to our intuition. However, when the Hamiltonian is independent of time and preserves the (discrete) translational invariance, the momentum-energy representation is a better option,

as it simplifies the analytic manipulation of the Green's function. Imagine the Schrodinger equation of a clean Hamiltonian with a delta function source, $\delta(x-x')\delta(t-t')$. Its solution is the Green's function. In energy-momentum space the expression of Green's function becomes simpler for time-independent and translationally invariant system:

$$G_0(p',p;E) = \frac{1}{E-\epsilon_p+i0}\delta_{p',p}, \tag{1.21}$$

$$= G_0(p;E)\delta_{p',p} \tag{1.22}$$

where the infinitesimally small positive imaginary number $i0$ ensures that $t' > t$ in time domain, as we assumed throughout this section. For time-independent disorder potential, the energy is a good quantum number since only the time difference, $t'-t$, matters in the Green's function. On the other hand, the potential can carry non-zero transfer, as its Fourier component in momentum space is non-zero. We can similarly repeat the perturbation analysis and come up with the self-consistent relation of Green's function:

$$G(p',p;E) = G_0(p',p;E) + G_0(p';E)\int dp'' V(p',p'')G(p'',p;E), \tag{1.23}$$

meaning that the amplitude of transition from a state (p,E) scattered into a state (p',E) through disorder potential $V(p',p'')$ and its higher orders. We will come back to this expression in later sections to introduce a more specific recipe of studying disordered systems.

1.4.2 T-matrix formulation

In the last section, we deduced the self-consistent expression of Green's function or propagator in the presence of disordered potential in terms of clean system Green's function G_0. It will be convenient if we can collect all multiple impurity scattering effects into a single

term. This effective impurity potential is called T-matrix, $T(p', p; E)$:

$$G(p', p; E) = G_0(p; E)\delta_{p',p} + G_0(p'; E) \int dp'' T(p', p''; E) G_0(p'', p; E), \tag{1.24}$$

Note that the right-most Green's function is replaced by the clean propagator, and that the T-matrix is solely responsible for the impurity effect. The previous self-consistent relation is now embedded in the T-matrix itself:

$$T(p', p; E) = V(p', p; E) + \int dp'' V(p', p''; E) G_0(p''; E) T(p'', p; E). \tag{1.25}$$

Note that combining (1.24) and (1.26) recovers (1.23). Because spatially uncorrelated impurities in the system are local objects, their scattering potentials are independent of momentum transfer. Especially if the concentration of impurities is dilute so that we only need to take into account a single impurity, then the self-consistent expression of the T-matrix is significantly simplified:

$$T(E) = \frac{I}{I - V(E) \int dp'' G_0(p''; E)} V(E). \tag{1.26}$$

The poles of Green's function correspond to on-shell electrons, as shown in (1.21). The poles of the T-matrix are new eigenstates created due to the impurity scatterings. In other words, bound states associated with impurities can be found by looking at the poles of the T-matrix, and their local density of state by taking the imaginary part.

Its application to the impurity effect on superconducting phase is one of the fields where T-matrix formulation has been productive (the Kondo problem in quantum mirage is an interesting application of multiple impurities[46]). First, the pairing in a conventional

superconductor is between time-reversal copies: electrons at opposite momentum with opposite spin are paired. Therefore, non-magnetic impurities cannot break the pairing and the superconducting state should be maintained. This is called Anderson's theorem, and Ma and Lee [56] proved it using T-matrix formulation. On the other hand, an unconventional superconductor with a higher-orbital momentum state (d-wave) pairing is susceptible to non-magnetic impurities, as they scatter electrons isotropically and do not respect the pairing symmetry. Balatsky and his colleagues extensively studied resonance bound states induced by either magnetic or non-magnetic impurities [57], and their local density of states profile with respect to the direction of nodes. All these signatures can be verified using a scanning tunneling microscope or the nuclear magnetic resonance technique.

1.4.3 Disorder averaging technique

Even though the T-matrix approach provides an analytic tool of studying physical quantities such as the local density of states renormalized by an impurity, when one is interested in thermodynamic quantities such as a critical temperature at phase transition or global density of states measured in planar junctions, we want to describe them in terms of the average impurity strength and its distribution. To achieve this goal in an analytical manner, physicists [58] came up with a technique called disorder averaging, which considers many different realizations of impurities from the same distribution, and computes the average of physical quantities such as conductivity or magnetic susceptibility. In this section, we will show the disorder averaging of the previously discussed Green's function, which will serve as a basic building block of physically more relevant quantities.

Imagine we have N-identical static impurities, V_{imp}, at location $r_1, \cdots, r_N$. As we want to know the Green's function in momentum and energy representation, Eq.(1.23), Fourier

transformed momentum space expression is necessary:

$$V(p,p') = V_{imp}(p-p')\sum_{i=1}^{N} e^{-\frac{i}{\hbar}(p-p')\cdot r_i} \tag{1.27}$$

$$= V(p-p') \tag{1.28}$$

What we mean by disorder averaging is to average the value in interest over all possible configurations of impurity locations in the system. For example, the disorder averaging of the potential is:

$$\langle V(p-p')\rangle_{dis} = \int \prod_{i=1}^{N} \frac{dr_i}{V}\left[V_{imp}(p-p')\sum_{i=1}^{N} e^{-\frac{i}{\hbar}(p-p')\cdot r_i}\right] \tag{1.29}$$

$$= n_i V_{imp}(0)\delta_{p,p'} \tag{1.30}$$

where $n_i = N/V$ is impurity concentration. $V_{imp}(0)$ is the spatial average of the impurity potential, which simply acts as a constant added to the Hamiltonian. The first order of the Green's function is $G^R_{(1)}(p',p) = G^R_0(p,E)\left[n_i V_{imp}(p=0)\right] G^R_0(p,E)\delta_{p',p}$. This term simply gives a shift of the whole Hamiltonian, and such a term is not important in physical quantities as it can be eliminated by adding a constant value to the Hamiltonian. The next order of the Green's function contains two scattering events in momentum space:

$$\langle G_{(2)}(p',p,E)\rangle_{dis} = G_0(p',E)\frac{1}{V}\sum_{p''}\langle V_{imp}(p'-p'')G_0(p'',E)V_{imp}(p''-p)\rangle_{dis}G_0(p,E)$$

$$= \delta_{p,p'}n_i^2[V_{imp}(p=0)]^2[G_0(p,E)]^3$$

$$+ \delta_{p,p'}n_i[G_0(p,E)]^2\frac{1}{V}\sum_{p''}|V_{imp}(p-p'')|^2 G_0(p'',E). \tag{1.31}$$

The interpretation of the disorder-averaged Green's function is not hard once we understand

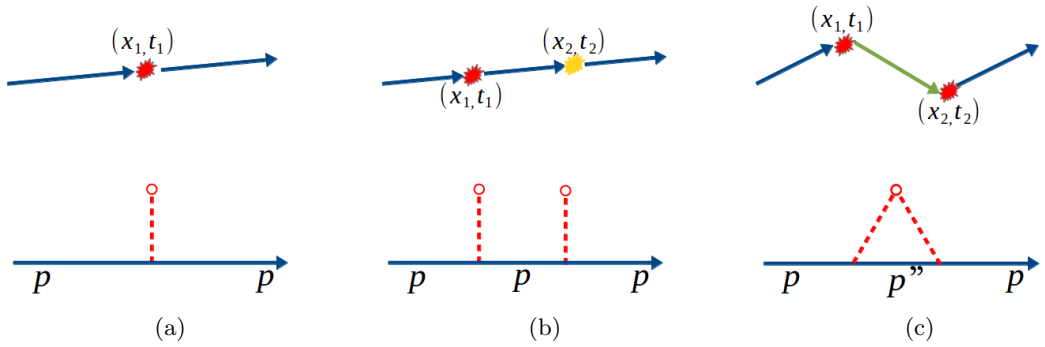

Figure 1.17: The disorder averaged impurity scattering process described in real and momentum space. (a) The first order correction shows a single scattering off from the impurity potential. Disorder averaging sums up all possible impurity configurations, which means that the coordinate (x_1, t_1) is integrated out, (1.20). But such a term does not give any change in momentum space. (b) Two independent impurity scattering events. After disorder averaging, each scattering event transfers zero momentum and in momentum space do not show a meaningful change. (c) A double scattering process from the same impurity is described. The impurity potential absorbed the momentum $p - p''$ first then give out back in the second scattering. This process produces a momentum-dependent correction, and the consistent summation of the diagrams in higher orders is crucial.

that the process of disorder averaging recovers the translational invariance by taking all possible realizations of impurity configurations. The total transferred momentum has to be zero, which is why $\delta_{p',p}$ always follows in each terms. Specifically, the first term is the case where each impurity potential carries zero momentum transfer from the scattering events, and thus it is proportional to n_i^2 and $[V_{imp}(p=0)]^2$. Again, this term is featureless in momentum space and we will not consider it seriously. The second term is the other possibility of carrying zero momentum transfer by two scatterings exchanging the same amount of momentum, $p - p''$. This process is only possible when an electron hit the same impurity twice, and therefore it is linearly dependent of the impurity concentration n_i.

In this way, we can compute the disorder averaged higher orders of Green's functions, and the number of scattering processes explodes when an increased number of scattering events is allowed. However, physicists wisely came up with a way to sum up the diagrams consistently, which carries important physical information to physical observables impurity

scatterings (Figure 1.18a). Multiple scatterings (Figure 1.18c) in which an electron scatters the same impurity more than two times are ignored, and crossing type of diagrams (Figure 1.18b) in which an electron scatters each impurities twice but in a mixed manner are also neglected.

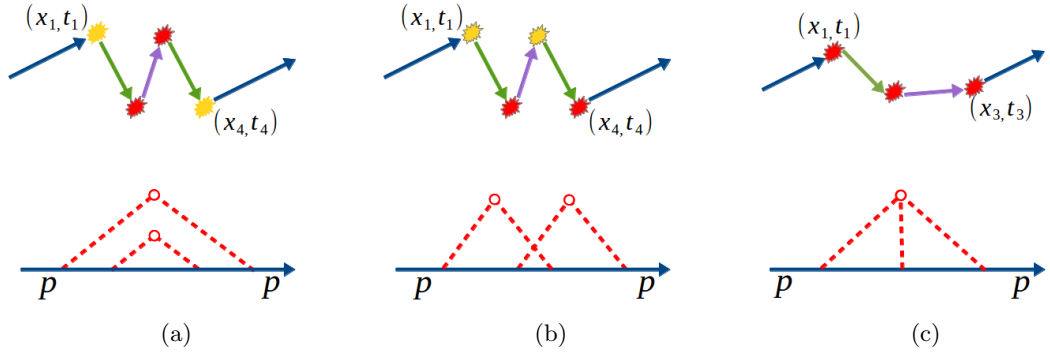

Figure 1.18: The next order corrections of Green's function due to impurity potential are described. (a) The similar type of non-crossing diagram with two different impurity scatterings. (b) Double scattering process, but the scattering order for different impurities distinguished by color is mixed. The crossing type of diagram limits the phase space volume over which electrons can explore in the process of scattering, and its contribution is less than the non-crossing type. (c) Multiple scattering events are also considered. Such an event is less likely than (a).

1.5 Overview

In the following chapters, we develop analytic tools to study disordered systems in the single particle Hamiltonian level. We apply them to topological insulators to study impurity-induced phenomena, as discussed in the introduction. More specifically, in Chapter 2, we developed a semiclassical approach obtaining bound states associated with a single impurity in topological insulators in 2d or higher dimensions. Though it is numerically straightforward to compute eigenenergies of bound states, we discovered the mapping of the 2d system with a delta-function-like single impurity to an effective 1d Hamiltonian with renormalized impurity potential. In Chapter 3, we studied the transport behavior of a topological-metal

strip. The coexistence of helical surface states and bulk states is experimentally observed [6]. Therefore, the transport through surface states in the presence of bulk modes and impurities is of interest for both experimental and theoretical perspectives. We studied the nature of transport in a 2d version of the analogous system. In the course of constructing the toy model of a topological-metal strip, we discovered a closed form of chiral edge mode Green's function coupled to bulk modes by impurities. In Chapter 4, we applied the expression to 1d disordered wire, and demonstrate its usage and advantages over conventional methods. In Chapter 5, the surface impurity effect on surface states in a topological insulator is discussed. In particular, the profile of local density of states due to the moderate to strong surface impurities is studied in a framework which is equally applicable to the arbitrary strength of impurities.

Chapter 2

Single impurity problem: Plane wave approach[†]

2.1 Background and Motivation

The presence of disorder is often considered a nuisance that degrades the quality of samples and obscures the behavior of clean physical systems. In small amounts, however, impurities may induce new phases which are interesting in their own right, and do not have a clean-system analog. Prominent examples are the metal-insulator transition induced by random on-site potential [43, 60, 61, 62], Cooper-pair breaking transition in conventional s-wave superconductors by magnetic [63, 64, 58, 65] and non-magnetic [66, 67, 56] impurities, impurity-induced spin quantum-hall effect [54, 68, 55], and the Kondo effect [69, 70].

Understanding the single impurity problem often provides strong intuition for the behavior of a disordered system with a finite impurity density. Using this as motivation, we study the problem of bound states of a single narrow impurity in a variety of host systems. For a narrow impurity, bound states could be found most straightforwardly by solving the Schrödinger equation outside and inside the impurity-affected region, and matching the wave functions at the boundary. In 1d, with a delta-function impurity potential, this is

[†]This chapter is published in [59]

particularly simple. It is also quite straightforward when dealing with 2d systems and a 1d perturbation such as an edge. However, for point-like impurities in 2d, a more complicated consideration is required.

Nevertheless, in this work we show that a 2d system with a point-like impurity could be reduced to a 1d problem on a straight trajectory, in which wavefunction matching can be applied. Furthermore, in spatially anisotropic systems (namely, lacking rotational symmetry about the impurity), we show that using a small number of incoming and outgoing beams and straight trajectories allows a remarkably accurate estimate of bound state energies.

The semiclassical approach has been instrumental in providing insightful physical pictures in terms of classical trajectories in complicated quantum systems, especially when impurity scatterers or confining potentials are involved. Examples of such applications include quasiparticle states near extended scatterers in d-wave superconductors [71], bound states in multidimensional systems with Fermi resonance [72], the low-energy spectrum of charge carriers in graphene [73], and the Berry phase in graphene [74]. The standard semiclassical methods which map complicated multidimensional quantum problems onto 1d quantum problem on simple classical trajectories, however, are approximations, and suffer from limitations that need to be addressed with more sophisticated methods [73, 75].

In the following sections we derive the mapping from 2d to an effective 1d impurity Hamiltonian, and then use it to find the bound state energies in several examples of increasing complexity. This mapping should be thought of as a semi-classical description of the 2d impurity problem, where the bound-state energies are obtained by considering a small number of classical incoming and outgoing beams. The mapping from 2d to 1d relies on the Green's function of the clean system, which indicates which 'classical' paths are necessary. Our method also approximates the bulk Hamiltonian by its form in the vicinity of minima

in momentum space, assuming a parabolic or Dirac-like dispersion. We find that with the introduction of appropriate cutoffs using the Pauli-Villars regulators, this approximation remains relatively precise.

The organization of the manuscript is as follows. In Sec. II we show how the 2d impurity problem can be reduced to a 1d problem for an isotropic Hamiltonian system. In Sec. III, the method is extended to an anisotropic Hamiltonian and then in Sec. IV to a band structure with multiple minima. While the extension of our method to any odd dimension is straightforward, the extension to even dimensions is not. In Sec. V we show how to generalize our method to all even dimensional systems.

2.2 Wave-matching for single isotropic minimum continuum band

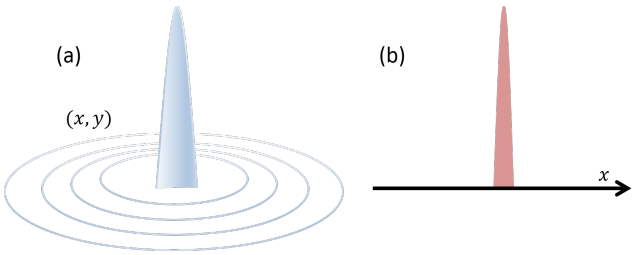

Figure 2.1: A 2d system with a point-like impurity (a) is reduced to the 1d system with a modified impurity strength. Thus, a simple picture of wavefunction matching can be applied to the 2d system to obtain a bound state energy associated with a single impurity in 2d.

Our goal in this section is to derive a method equivalent to the 1d wavefunction matching technique, for finding the bound states of an impurity in an isotropic 2d system. For this purpose, let us briefly review how a bound state associated with a single point-impurity is

obtained in a 1d system. The Schrödinger equation in this case is simply:

$$[E - H(\partial_x)]\psi(x) = \alpha\delta(x)\psi(x), \tag{2.1}$$

where Hamiltonian H is responsible for kinetic part only, and the impurity scattering strength is α. The Green's function of the operator $E - H(\partial_x)$ is given by:

$$G(x) \quad = \quad \int_{-\infty}^{\infty} \frac{dk}{2\pi} \frac{e^{ikx}}{E - \tilde{H}(k)}, \tag{2.2}$$

where $\tilde{H}(k)$ is the Hamiltonian in momentum representation. The Green's function $G(x)$ is understood as the amplitude of the propagator at x, originating from the source at $x = 0$. Eq.(2.2) can be computed using contour integration around the upper (lower) half of complex k-plane for positive (negative) x. If the energy, E, is within the band, the (real-axis) poles of the integrand each correspond to a plane wave, and the combination of these waves makes up the Green's function. If the energy is outside the band, as would be the case for a bound state, the poles are not on the real axis and therefore the wave function decays exponentially with distance. We can still think of such a Green's function as a combination of plane waves, but with complex wave vectors.

To obtain a bound state energy associated with the impurity, we could take two paths. Formally, we use the fact that the Green's function is the solution of Eq.(5.1), omitting $\alpha\psi(x)$ on the right side of the equality. Therefore:

$$\psi(x) = G(x)\alpha\psi(0), \tag{2.3}$$

and we obtain for a scalar Hamiltonian :

$$\frac{1}{\alpha} = G(0) = \int_{-\infty}^{\infty} \frac{dk}{2\pi} \frac{1}{E - \tilde{H}(k)}, \tag{2.4}$$

consistent with the T-matrix formulation [76].

For a Hamiltonian with internal structure such as sublattice or spin, the Green's function and the impurity potential are matrices. The impurity potential matrix, α, may not be invertible. In this case, for $\vec{\psi}(0)$ to have a non-trivial solution at $x = 0$, the following condition is required:

$$\mathrm{Det}[\mathrm{I} - \mathrm{G}(0)\alpha] = 0. \tag{2.5}$$

For simplicity of presentation, in most of this manuscript we consider only scalar problems. In Sec. IV, along with extending our method to the case of host systems with multiple low-gap valleys, we also assume a multi-component wave function.

An alternative to the above method is to solve the 1d equation as Eq.(5.1) simply by matching a freely propagating plane-wave solution at $x > 0$ with a different plane-wave solution at $x < 0$. Integrating the Schrödinger equation over the impurity position gives:

$$\alpha\psi(0) - \int_{-\epsilon}^{\epsilon} (E - H)\psi(x)dx = 0. \tag{2.6}$$

Indeed, the same bound energy relation as Eq.(2.4) or Eq.(2.5) is obtained from this wave function-matching approach by inserting Eq.(2.3) to the above equation.

Could we use the same notion of 'wave-function matching' in the context of a bound

state in 2d? Let us start with 2d Schrödinger equation:

$$[E - H_{2d}(\vec{r})]\Psi(\vec{r}) = \alpha\delta^2(\vec{r})\Psi(\vec{r}). \tag{2.7}$$

To solve for a bound state at energy E, we can still use Eq.(2.3), adapted to 2d with

$$G(x) \quad = \quad \int_{-\infty}^{\infty} \frac{d^2k}{(2\pi)^2} \frac{e^{ikx}}{E - \tilde{H}(k)}, \tag{2.8}$$

and

$$\frac{1}{\alpha} = G(0) = \int \frac{d^2\vec{k}}{(2\pi)^2} \frac{1}{E - \tilde{H}_{2d}(\vec{k})}, \tag{2.9}$$

where $\tilde{H}_{2d}(\vec{k})$ is the 2d Hamiltonian in momentum representation. For this section, we assume an isotropic Hamiltonian $\tilde{H}_{2d}(\vec{k}) = \tilde{H}_{2d}(k)$. Hence we can write Eq.(2.9) as:

$$\frac{1}{\alpha} = G(0) = \int \frac{d\theta}{2\pi} \int_0^{\infty} \frac{kdk}{2\pi} \frac{1}{E - \tilde{H}_{2d}(k)}. \tag{2.10}$$

Eq.(2.10) cannot simply be interpreted in terms of plane wave matching as its 1d counterpart since contour integration over a complex k can not be used: the integration range is $0 \leq k < \infty$. Nevertheless, we can proceed using the Kramers-Kronig relation along with the symmetry of the imaginary part of the integrand and obtain an expression analogous to Eq.(2.4).

The Kramers-Kronig relation connects the imaginary and real parts of a complex function, $f(s)$, which is analytical in the upper half plane, Im(s) > 0, and falls off faster than

$1/|s|$. To apply it here, we define:

$$F(s) = \int_0^\infty \frac{kdk}{2\pi} \frac{e^{iks}}{E - \tilde{H}_{2d}(k)}. \tag{2.11}$$

Note that this function is not the Green's function in real space, since there is no angular dependence taken into account in the exponent. However, $F(0) = G(0)$. Furthermore, we see that only Re[G(0)] plays a role in determining the bound-state energy of an impurity state. We use the Kramers-Kronig relation to write:

$$\mathrm{Re[F(0)]} = \int_{-\infty}^{\infty} \frac{\mathrm{ds'}}{\pi \mathrm{s'}} \mathrm{Im[F(s')]}. \tag{2.12}$$

This is helpful since the imaginary part of $F(s)$ for $\mathrm{Im(s)} = 0$ obeys:

$$\mathrm{Im[F(s)]} = \frac{1}{2} \int_{-\infty}^{\infty} \frac{\mathrm{kdk}}{2\pi} \frac{\mathrm{e^{iks}}}{\mathrm{E} - \tilde{\mathrm{H}}_{2\mathrm{d}}(\mathrm{k})}, \tag{2.13}$$

with the k integral now stretching over the entire real axis. It is assumed that the Hamiltonian $\tilde{H}_{2d}(k)$ is an even function of k.

After these steps we can rewrite the bound state energy condition as:

$$\frac{1}{\alpha} = \frac{1}{\pi} \int_{-\infty}^{\infty} \frac{ds}{s} Im \left[\int_0^\infty \frac{kdk}{2\pi} \frac{e^{iks}}{E - \tilde{H}_{2d}(k)} \right], \tag{2.14}$$

$$= \frac{1}{\pi} \int_0^\infty \frac{ds}{is} \left[\int_{-\infty}^{\infty} \frac{kdk}{2\pi} \frac{e^{iks}}{E - \tilde{H}_{2d}(k)} \right]. \tag{2.15}$$

Finally, we also eliminate the factor of k in the integrand using a derivative with respect to

s, to yield our final expression:

$$\frac{1}{\alpha} = \frac{-1}{\pi}\int_0^\infty \frac{ds}{s}\frac{\partial}{\partial s}\left[\int_{-\infty}^{\infty}\frac{dk}{2\pi}\frac{e^{iks}}{E-\tilde{H}_{2d}(k)}\right]. \tag{2.16}$$

The term in the square brackets in Eq.(2.16) is completely analogous to the expression used to find the bound state energy of a 1d solution of a point-impurity (Eq.(2.2)) and we therefore define:

$$G_{1d}(s) = \int_{-\infty}^{\infty}\frac{dk}{2\pi}\frac{e^{iks}}{E-\tilde{H}_{2d}(k)}, \tag{2.17}$$

which can be viewed as the Green's function of a 1-d Hamiltonian $H_{1d}(s) \equiv \tilde{H}_{2d}(k \to \frac{\partial}{i\partial s})$ in real space. Qualitatively, the effective real-space 1-d Hamiltonian, H_{1d}, describes a single direction of the 2-d momentum-space Hamiltonian $\tilde{H}_{2d}$.

The final result of this reasoning is that the bound-state energy E for a 2d point impurity can be obtained by solving a 1d impurity problem with a modified potential. Provided that $G_{1d}(x)$ is the solution of the 1-d Hamiltonian $H_{1d}(x)$, the wave function $\psi_{1d}(x) = G_{1d}(x)$ up to an overall normalization factor for a scalar Hamiltonian. From Eq.(2.16) and Eq.(2.17) the effective 1-d Schrödinger equation can be written with a modified impurity potential:

$$\left[E - H_{1d}(x)\right]\psi_{1d}(x) = \delta(x)\alpha'\psi_{1d}(0), \tag{2.18}$$

with α' given by:

$$\alpha' = -\alpha\left[\frac{1}{\pi}\int_0^\infty \frac{ds}{s}\frac{\partial\psi_{1d}(s)}{\partial s}\right]\frac{1}{\psi_{1d}(0)}. \tag{2.19}$$

$\psi_{1d}(s)$ on the right hand side of Eq.(2.19) emerges as the solution of the effective 1d problem,

but does not appear to have any physical significance.

The first example for our method is the free particle with quadratic dispersion. We demonstrate the method by finding the 1d effective Hamiltonian in real space, and solving it in the spirit of the wavefunction matching method. The free particle example in 2d is a bit pathological, however, since a high energy cutoff is required, and the bound state energies of point impurities depend on it. This is seen by inspecting Eq.(2.9): the momentum integration diverges, unless a cutoff is imposed. This introduces a technical challenge for our quest to use momentum integration over the entire real-axis. We resolve it by introducing the cutoff using the Pauli-Villars regularization technique [77].

Starting with the free Hamiltonian and an impurity potential,

$$H_{2d} = -\frac{\nabla^2}{2m}, \tag{2.20}$$

$$V_{imp} = \alpha\delta^{(2)}(\vec{x}). \tag{2.21}$$

We write the Green's function condition for an impurity bound state, and include the Pauli-Villars regulators $W^2/(k^2+W^2)$:

$$\frac{1}{\alpha} = \int \frac{d^2\vec{k}}{(2\pi)^2}\frac{1}{E-\tilde{H}_{2d}(k)}\left(\frac{W^2}{W^2+k^2}\right). \tag{2.22}$$

According to our recipe, this is equivalent to finding bound states of the following 1-d effective Hamiltonian:

$$\tilde{H}_{1d}(k) = \frac{k^2}{2m} - \left(E-\frac{k^2}{2m}\right)\frac{k^2}{W^2}. \tag{2.23}$$

It is interesting to consider the effective 1d Hamiltonian, Eq.(2.23) and the effect that

the Pauli-Villars regulator has. $\tilde{H}_{1d}$ preserves the original dispersion relation, and a $k^2/2m$ pole is reflected in the Green's function. In addition, the Green's function acquires an additional pair of poles at $k_p = \pm iW$.

Now we can treat the problem just like a 1-d problem with a plane wave solution, but with multiple plane waves corresponding to all solutions of $E\psi_{1d} = \tilde{H}_{1d}\psi_{1d}$ (which correspond to the poles of the Green's function). The solution must satisfy continuity conditions at $x = 0$ of the derivatives:

$$\left[\frac{\partial^m \psi(x)}{\partial x^m}\right]_{0-}^{0+} = 0, \tag{2.24}$$

for $m = 0, 1, 2$, which provides enough conditions to fix the weights of the plane waves up to an overall factor on $x < 0$ and $x > 0$:

$$\psi(x > 0) = \frac{1}{\lambda_1} e^{-\lambda_1 x} - \frac{1}{\lambda_2} e^{-\lambda_2 x}, \tag{2.25}$$

$$\psi(x < 0) = \frac{1}{\lambda_1} e^{\lambda_1 x} - \frac{1}{\lambda_2} e^{\lambda_2 x}. \tag{2.26}$$

The exponents are $\lambda_1 = \sqrt{-2mE}$ and $\lambda_2 = W$, which are the poles of the Green's function. Now we use Eq.(2.18) to find the bound state energy for a given impurity potential strength. First, we carry out the integration that yields the effective α' using Eq.(2.19):

$$\alpha' = \frac{\alpha}{\pi} \frac{\lambda_1 \lambda_2}{\lambda_2 - \lambda_1} \log\left(\frac{\lambda_2}{\lambda_1}\right). \tag{2.27}$$

With this modified impurity potential and the 1d effective Hamiltonian Eq.(2.23) in real

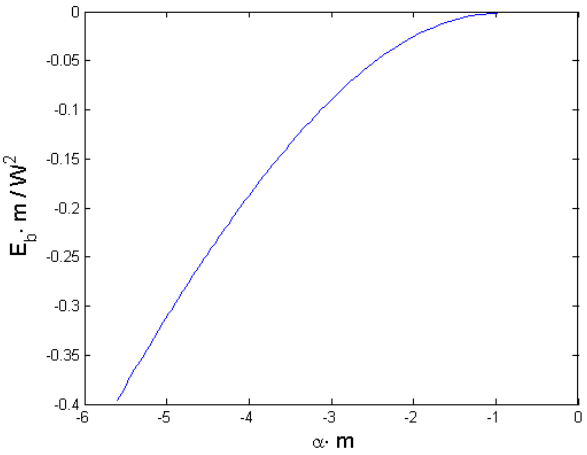

Figure 2.2: Bound energy E_b of the free particle model with mass m and cutoff W for the regularization is plotted as a function of impurity strength α. The bound energy decreases as the impurity strength negatively increases. In the limit of zero impurity strength, the bound energy converges to zero.

space, one can solve the 1d problem and get:

$$\frac{1}{\alpha} = \frac{-m/\pi}{1+2mE/W^2} \log\left(\frac{W}{\sqrt{-2mE}}\right). \tag{2.28}$$

As seen from Eq.(2.28), the bound state energy is renormalized by the cutoff and mass, but its qualitative behavior as a function of the impurity potential strength is unchanged. This is depicted in Fig. 2.2.

Let us study one more isotropic Hamiltonian - a Mexican hat-shaped energy band:

$$\tilde{H}_{2d}(k) = J(k^2 - k_0^2)^2, \tag{2.29}$$

where J is a constant with units of length cubed. The band covers all positive energies and therefore the energy of any bound state should be negative.

The Mexican hat Hamiltonian does not have a UV divergence problems as the free-particle Hamiltonian, and therefore does not require a Pauli-Villars regulator. Thus $\tilde{H}_{1d}(k) =$

$\tilde{H}_{2d}(k)$ in this case. Incidentally, it also has the same order of derivatives as the regularized free particle Hamiltonian, Eq.(2.23). Therefore, it obeys the same number of continuity relations and we may simply use the same functional form ansatz as in Eq.(2.25)-(2.26), with the wave numbers given by:

$$k_1 = i\lambda_1 = k_0 \left(1 + i\sqrt{\frac{-E}{Jk_0^4}}\right)^{1/2}, \tag{2.30}$$

$$k_2 = i\lambda_2 = k_0 \left(1 - i\sqrt{\frac{-E}{Jk_0^4}}\right)^{1/2}, \tag{2.31}$$

which is the result of setting $E = \tilde{H}_{1d}(k)$. Carrying out the same steps as in the free-particle case, we obtain that the relation between the bound state energy and the impurity strength is:

$$\frac{1}{\alpha} = \frac{1}{2\pi J}\frac{\log(\lambda_2/\lambda_1)}{\lambda_2^2 - \lambda_1^2}, \tag{2.32}$$

$$= \frac{-1}{4\pi J}\frac{\tan^{-1}\sqrt{-E/Jk_0^4}}{\sqrt{-E/J}}, \tag{2.33}$$

where it follows from the above expression that the bound state exists only for attractive potential. The result is plotted in Fig. 2.3 with renormalized axes.

2.3 Wavefunction matching for Anisotropic bands

When the impurity problem is anisotropic, we can no longer solve for the bound-state energies exactly using only a small number of incoming and outgoing beams. Instead, we can still consider simple 1d wave-functions for the radial part of the problem, and then consider a superposition over all angles. Here we extend the wavefunction matching method to such anisotropic systems.

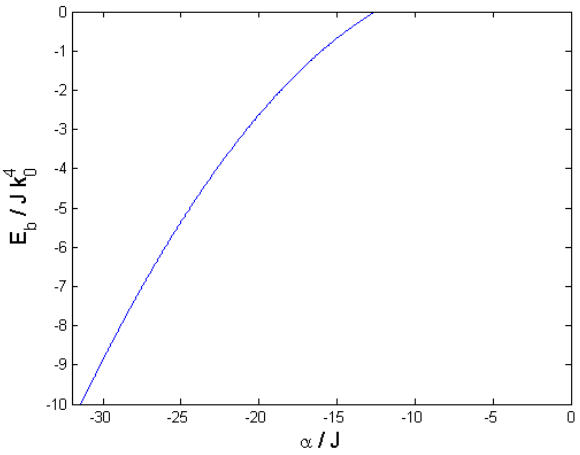

Figure 2.3: Bound energy E_b of the Mexican hat model is plotted as a function of impurity strength α. The general behavior is similar to that of the free particle model except that the bound state appears when $\alpha < -1/4\pi J k_0^2$.

We begin by writing the Hamiltonian in polar momentum coordinates: $\tilde{H}_{2d}(\vec{k}) = \tilde{H}^{\theta}_{2d}(k)$, with θ being the momentum direction. Now, when going from Eq.(2.9) to Eq.(2.10), the angular integration must be kept:

$$\frac{1}{\alpha} = \int \frac{d\theta}{2\pi} \int_0^{\infty} \frac{kdk}{2\pi} \frac{1}{E - \tilde{H}^{\theta}_{2d}(k)}. \tag{2.34}$$

Following exactly the same steps, we introduce a 1-d wave function along momentum angle θ:

$$G^{\theta}_{1d}(s) = \int_{-\infty}^{\infty} \frac{dk}{2\pi} \frac{e^{iks}}{E - \tilde{H}^{\theta}_{2d}(k)}, \tag{2.35}$$

which is the Green's function of 1-d Hamiltonian $H^{\theta}_{1d}(s) \equiv \tilde{H}^{\theta}_{2d}(k \to \frac{\partial}{i\partial s})$. The modified relation between potential strength and associated bound state energy is:

$$\frac{1}{\alpha} = \int \frac{d\theta}{2\pi} \frac{1}{\alpha^{\theta}}, \tag{2.36}$$

where $1/\alpha^\theta$, just as in the right hand side of Eq.(2.16) , is:

$$\frac{1}{\alpha^\theta} = -\frac{1}{\pi}\int_0^\infty \frac{ds}{s}\frac{\partial G_{1d}^\theta(s)}{\partial s}. \tag{2.37}$$

As pointed out above, the Green's function $G_{1d}^\theta(s)$ is constructed using plane wave solutions of $\tilde{H}_{2d}^\theta(\frac{\partial}{i\partial s})$, treated as a 1d Hamiltonian. For a general anisotropic system, the above prescription requires infinitely many directions of 1-d solutions.

A more direct formulation of the α_θ in terms of a 1d Schrödinger equation for each θ direction is as follows. We construct for each θ a solution of the 1d bound state equation:

$$\left[E - \tilde{H}_\theta\left(\frac{\partial}{i\partial s}\right)\right]\psi^\theta(s) = \alpha'^\theta\delta(s)\psi^\theta(s), \tag{2.38}$$

and find α'^θ in terms of E by requiring that the 1d problem has a bound state at energy E. The integrand in the right-hand-side of Eq.(2.36), α^θ, is given in terms α'^θ and the impurity-state wave function, $\psi^\theta(s)$, as:

$$\frac{1}{\alpha^\theta} = -\frac{1}{\alpha'^\theta}\frac{1}{\pi}\int_0^\infty \frac{ds}{s}\frac{\partial\psi^\theta(s)}{\partial s}\frac{1}{\psi^\theta(0)}. \tag{2.39}$$

As a simple example, we consider impurity states in a band described by a parabolic dispersion with an anisotropic mass:

$$\tilde{H}(\vec{k}) = \frac{k_x^2}{2m_x} + \frac{k_y^2}{2m_y} \equiv \frac{k^2}{2m(\theta)}, \tag{2.40}$$

where

$$\frac{1}{m(\theta)} = \frac{cos^2\theta}{m_x} + \frac{sin^2\theta}{m_y}. \tag{2.41}$$

This problem can be simply solved by rescaling x relative to y, and obtaining the isotropic solution. Therefore this calculation should just be a demonstration of using our method. For more complicated band structures (e.g., bands with multiple minima, as discussed below) this will not be possible.

Let us now construct G_{1d}^{θ} and α^{θ}. For a given direction we can make use of the relation we obtained before for a free particle, using $m(\theta)$ instead of m. Using Eq.(2.28), with $\alpha \to \alpha^{\theta}$, we obtain:

$$\frac{1}{\alpha^{\theta}} = \frac{-m(\theta)/\pi}{1+2m(\theta)E/W^2}\log\left(\frac{W}{\sqrt{-2m(\theta)E}}\right). \tag{2.42}$$

The last step in this consideration should be the integration of Eq.(2.42) over all momentum directions. However, we find that in this case it is enough to consider a pair of perpendicular directions – the extrema of α^{θ} which occur at $\theta = 0, \pi$ and $\theta = \pi/2, 3\pi/2$. This is shown in Fig. 2.4 where the dash-dot (black) line shows the result of the integration over all directions, and the other lines show two different directions (solid, dotted) and their combination (dashed). As evident from the graph, the combination of two perpendicular directions is very similar to the integrated expression. This is equivalent to evaluating the θ integral using a discrete sum, which could be used to reduce the number of beams necessary in a 2d problem to a finite and small number.

2.4 A band with multiple minima

Perhaps the most interesting application of our method is to dispersion relations which contain several gap minima. The qualitative picture of a bound state consisting of a simple superposition of several 1d beams each coming from the vicinity of one particular gap mini-

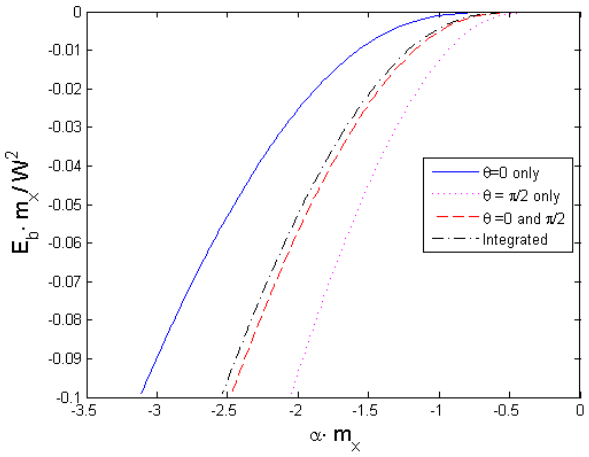

Figure 2.4: Bound energy associated with a single impurity for two-mass anisotropic band model ($m_y/m_x = 2$). The exact bound state energy is obtained by integrating over all momentum angle θ, while taking a straight "1d" path with a certain momentum angle yields slightly deviated bound state energy. Nevertheless, the consideration of only two momentum angle $\theta = 0$ and $\pi/2$ gives a fair agreement with the exact result.

mum is rather intuitive and appealing. Our method allows making this picture quantitative even for complicated band structures.

So far we have identified the single minimum of the band and used an approximated version of the Hamiltonian around the minimum. Then, according to Eq.(2.9), the Green's function is obtained and integrated with an appropriate cutoff W introduced through the Pauli Villars regulator. The generalization to more than one band minimum is dividing the integration in Eq.(2.9) into the summation of multiple integrations with different local Hamiltonians, which are the expansions of the Hamiltonian around each minimum. In many cases where multiple valleys need to be considered, the wavefunction is a multidimensional spinor. Therefore, we need to represent the impurity strength α by a matrix and use the determinant condition for bound states, Eq.(2.5).

$$\int \frac{d^2\vec{k}}{(2\pi)^2} \frac{1}{E - \tilde{H}_{2d}(\vec{k})} \approx \sum_l \int \frac{d^2\vec{k_l}}{(2\pi)^2} \frac{1}{E - \tilde{H}_l(\vec{k_l})}. \tag{2.43}$$

Where l goes over the band minima and H_l is the expansion of the Hamiltonian around the lth minimum with the appropriate Pauli-Villars regularization included. The origin of each $\vec{k_l}$ is set to the center of the minima such that the 'valley' Hamiltonian $\tilde{H}_l(\vec{k_l})$ has maximum symmetry. Thus, the condition for a bound state is:

$$\det\left(1-\sum_l \int \frac{d^2\vec{k_l}}{(2\pi)^2}\frac{1}{E-\tilde{H}_l(\vec{k_l})}\alpha\right)=0. \tag{2.44}$$

Applying the Kramers-Kronig trick here as well as in the anisotropic construction, we write the potential strength as a sum:

$$\det\left(1-\sum_l \int \frac{d\theta}{2\pi}\frac{1}{\alpha_l^\theta}\alpha\right)=0, \tag{2.45}$$

where $\left(\alpha_l^\theta\right)^{-1}$ is a matrix, given by:

$$\frac{1}{\alpha_l^\theta}=-\frac{1}{\pi}\int_0^\infty \frac{ds}{s}\frac{\partial G_l^\theta(s)}{\partial s}, \tag{2.46}$$

with

$$G_l^\theta(s)=\int_{-\infty}^{\infty}\frac{dk}{2\pi}\frac{e^{iks}}{E-\tilde{H}_l^\theta(k)},$$

the Green's function for the Hamiltonian $\tilde{H}_l^\theta=\tilde{H}_l(k\hat{x}\cos\theta+k\hat{y}\sin\theta)$.

As described in Sec. 2.3, Eq.(2.46) can also be interpreted in terms of individual 1d plane waves in each direction and valley. This is made a bit more complicated by taking into account a spinor index. Denoting the spinor indices with σ, σ', we have

$$\left(\alpha_l^\theta\right)^{-1}_{\sigma\sigma'}=-\frac{1}{b_l^{\theta,\sigma'}}\frac{1}{\pi}\int_0^\infty\frac{ds}{s}\frac{\partial[\psi_l^{\theta,\sigma'}]_\sigma(s)}{\partial s}\frac{1}{[\psi_l^{\theta,\sigma'}]_{\sigma'}(0)}, \tag{2.47}$$

where $b_l^{\theta,\sigma'}$ and $[\psi_l^{\theta,\sigma'}]_\sigma(s)$ are obtained by solving the 1d impurity problem of a particle with the Hamiltonian $\tilde{H}_l^\theta(k \to \frac{\partial}{i\partial s})$, which is the original 2d Hamiltonian for a particular momentum direction, θ, and with momentum in the vicinity of the bottom of valley l. Let us clarify these symbols further, and state the impurity problem that needs to be solved:

$$[(E - \tilde{H}_l^\theta)\psi_l^{\theta,\sigma'}]_\sigma(s) = \delta_{\sigma\,\sigma'}\delta(s) b_l^{\theta,\sigma'}[\psi_l^{\theta,\sigma'}]_\sigma(s). \tag{2.48}$$

The index σ' indicates to which component the impurity couples, and $b_l^{\theta,\sigma'}$ is the impurity strength required to induce an impurity state with energy E in the specified valley, direction, and component of the spinor involved. Accordingly, $[\psi_l^{\theta,\sigma'}]_\sigma(s)$, is the σ component at point s of the (valley l and momentum angle θ) wave function of a bound state of an impurity that couples to the σ' component. Note that the impurity strength is multiplied by the σ' component of the wave function.

As an example of an anisotropic system with multiple minima, we consider an impurity problem in the Kane-Mele model[12]. This model describes electrons hopping on a honeycomb lattice with mirror-symmetric spin-orbit coupling. It was the first model theorized to display a time reversal symmetric topological phase, i.e., the quantum spin Hall phase. The two sublattices of the honeycomb lattice are encoded in two-dimensional spinors, and its band structure has two massive Dirac points in the Brillouin zone. For simplicity, but without loss of generality, we focus on a non-magnetic impurity and consider spinless fermions. The Hamiltonian[14] is:

$$H = t\sum_{\langle ij\rangle} c_i^\dagger c_j + i\lambda_{SO}\sum_{\langle\langle ij\rangle\rangle} \nu_{ij} c_i^\dagger s^z c_j. \tag{2.49}$$

The first term is a nearest neighbor hopping, and the second term is spin-orbit interaction.

s^z is a Pauli matrix which acts in the spin space. $\nu_{ij} = (2/\sqrt{3})(\hat{d}_1 \times \hat{d}_2)_z = \pm 1$, where $\hat{d}_1$ and $\hat{d}_2$ are unit vectors along the two bonds the electron traverses going from site j to its next nearest neighbor i. The effective Hamiltonian near the valley K can be expressed by a 2×2 matrix in the pseudospin basis:

$$\tilde{H}_K(q) = \begin{pmatrix} m & qe^{-i\theta} \\ qe^{i\theta} & -m \end{pmatrix}, \tag{2.50}$$

where q is the momentum measured from K. Since the linear spectrum is not well behaved in the presence of a δ-function potential, we employ the Pauli-Villars regularization procedure as before. The regularized Hamiltonian reads:

$$\tilde{H}'_K(q) = \tilde{H}_K(q) - \left[E - \tilde{H}_K(q)\right] \frac{q^2}{W^2}. \tag{2.51}$$

The impurity is also described by a 2×2 potential matrix and we choose to put it on the A site.

$$\alpha = \alpha_0 \begin{pmatrix} 1 & 0 \\ 0 & 0 \end{pmatrix}. \tag{2.52}$$

To work this Hamiltonian in the sprit of 1d wave function matching method, we ought to solve the real space 1d Hamiltonian $H'_K(s) = \tilde{H}'_K(q \to \frac{\partial}{i\partial s})$. Instead, let us work with real space Green's function and then make use of Eq.(2.5) to find an associate bound energy of

a single impurity. We follow the matrix version of Eq.(2.35):

$$G_K^\theta(s) = \int \frac{dk}{2\pi} \frac{e^{iks}}{E - \tilde{H}'_K(k)}, \tag{2.53}$$

$$= \sum_{j=1,2} \frac{(-1)^j e^{-\lambda_j s}/2}{|\lambda_j|(1+\frac{E^2-m^2}{W^2})} \begin{pmatrix} E+m & i\lambda_j e^{-i\theta} \\ i\lambda_j e^{i\theta} & E-m \end{pmatrix}, \tag{2.54}$$

where the poles of Green's function are $\lambda_1 = \sqrt{m^2 - E^2}$, and $\lambda_2 = W$ for $s > 0$, and it is understood that $(-1)^{j=1} = -1$ and $(-1)^{j=2} = 1$. The diagonal elements of the solution are symmetric of s, while the off-diagonal elements are asymmetric. This is the wavefunction for the two sublattice system. For the other Dirac valley, K', the calculation is similar except that the sign of the spin orbit coupling is opposite. Following Eq.(2.37) for anisotropic Hamiltonians:

$$\frac{1}{\alpha^\theta_{K,K'}} = \frac{-1}{\pi} \int_0^\infty \frac{ds}{s} \frac{\partial G^\theta_{K,K'}(s)}{\partial s}. \tag{2.55}$$

The only remaining step is to consider the determinant from Eq. (2.5) and (2.44), in order to connect the potential strength and bound state energy:

$$\mathrm{Det}\left[\mathrm{I}_2 + \sum_{\mathrm{m=K,K'}} \int \frac{\mathrm{d}\theta}{2\pi} \frac{1}{\alpha^\theta_{\mathrm{m}}} \cdot \alpha\right] = 0. \tag{2.56}$$

As a result, we obtain the relation between the bound state energy and the potential strength α_0 in the Kane-Mele model:

$$\frac{1}{\alpha_0} = \frac{E}{2\pi^2(W^2 - m^2 + E^2)} \log\left(\frac{W}{\sqrt{m^2 - E^2}}\right). \tag{2.57}$$

This is plotted in Fig. 2.5, in which we show both positive and negative impurity strengths

and the associated positive and negative bound state energy. We compare our results for an exact diagonalization solution for the bound-state energy,

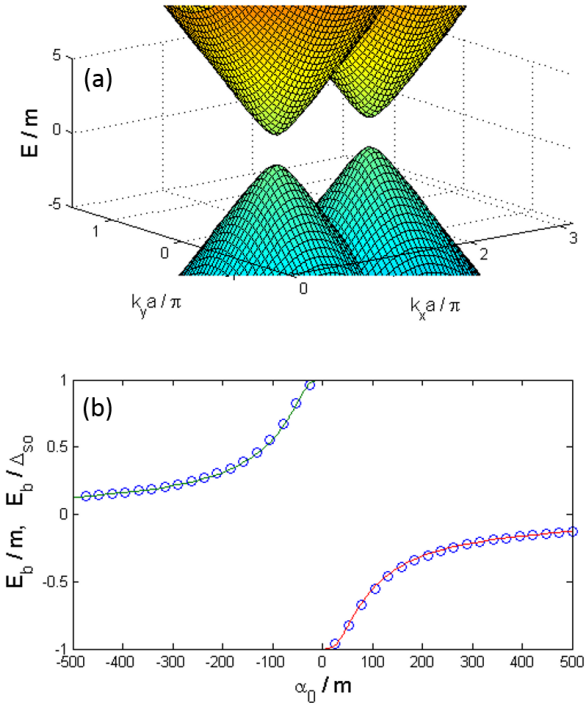

Figure 2.5: The Kane and Mele model is employed as an example of multiple minima band with $W/m = 1.6$. The band gap appears near zero energy and its size is proportional to the spin-orbit coupling. The bound state energy associated with a single impurity is always within the gap, and they converge to zero energy at infinite impurity strength. The exact diagonalization result of the Kane-Mele model on the honeycomb lattice of 20×20 unit cells is overlaid for comparison with $\lambda_{SO} = m/6\sqrt{3}$ (open circles) so that the band gap of lattice model $\Delta_{SO} = 6\sqrt{3}\lambda_{SO} = m$. The cutoff W is chosen such that the dispersion relation of continuum model is a good approximation of that of the lattice model.

2.5 Generalization to higher dimensions

We have studied how to obtain the bound energy associated with a single impurity and found that the Green's function at the impurity potential is a crucial quantity to find:

$$G(\vec{0}) = \int \frac{d\Omega}{(2\pi)^{d-1}} \int_0^\infty \frac{k^{d-1}dk}{2\pi} \frac{1}{E - \tilde{H}_d(\vec{k})}. \tag{2.58}$$

Although we have only discussed 2d systems, our method has a straightforward extension to higher dimensions. For odd dimensional cases, the wave function can be expressed by the summation of plane waves with certain momentum angles, since the k-integrals in Eq.(2.58) could be extended to the entire real k range. Then poles of the effective oriented Green's function combine to produce the solution, and the "wave function matching" picture straightforwardly follows when relating to the impurity strength.

In this section let us consider a Hamiltonian in an even dimensional space. For simplicity we assume an isotropic Hamiltonian without any spinor structure. Then the bound state energy associated with the single impurity potential, $V(\vec{x}) = \alpha\delta^{2n}(\vec{x})$, is expressed similarly to Eq.(2.9) by:

$$\frac{1}{\alpha} = \int \frac{d^{2n}\vec{k}}{(2\pi)^{2n}} \frac{1}{E - \tilde{H}_{2n}(k)}, \tag{2.59}$$

$$= \int \frac{k^{2n-1}dk}{2\pi} \frac{1}{E - \tilde{H}_{2n}(k)}, \tag{2.60}$$

where the difficulty lies in the integration in polar coordinates; as in the 2d case, the contour integration is not readily possible, and therefore any connection to a semi-classical beam analysis is not possible. Nevertheless, to overcome this hurdle we may use the same prescription as in 2d. We use the Kramers-Kronig relation to make use of the symmetric

imaginary part of the integrand and obtain the generalized relation:

$$\frac{1}{\alpha} = \frac{-1}{\pi}\int_0^\infty \frac{ds}{s}\frac{\partial^{2n-1}}{\partial s^{2n-1}}\left[\int_{-\infty}^{\infty}\frac{dk}{2\pi}\frac{e^{iks}}{E-\tilde{H}_{2n}(k)}\right]. \tag{2.61}$$

For isotropic and single-minimum band type problems, the above relation can be translated to finding an impurity state in a renormalized-strength impurity potential in the 1-d effective Schrödinger equation:

$$\left[E - H_{1d}(\partial_x)\right]\psi_{1d}(x) = \delta(x)\left[\frac{-\alpha}{\pi}\int_0^\infty \frac{ds}{s}\frac{\partial^{2n-1}}{\partial s^{2n-1}}\psi_{1d}(s)\right], \tag{2.62}$$

where $H_{1d}(\partial_x) = \tilde{H}_{2n}(k \to \frac{\partial}{i\partial x})$, and the solution is the sum of plane waves with complex wave numbers:

$$\psi_{1d}(x) = \int_{-\infty}^{\infty}\frac{dk}{2\pi}\frac{e^{iks}}{E-\tilde{H}_{2n}(k)}. \tag{2.63}$$

2.6 Conclusions and summary

Finding impurity bound states in 1d is quite intuitive, and is carried out by combining plane-wave states into a consistent solution. The plane-wave approach to solving impurity problems in 1d arises naturally when considering the T-matrix approach, or, equivalently, the Green's function expression of Eq.(2.4). The contour integration of the 1d Green's function results in a discrete sum of pole-contributions, each of which is associated with a plane-wave eigenstate of the uniform Hamiltonian. In 1d, the Schrödinger equation can be used directly to obtain impurity states, and such a calculation would involve satisfying matching conditions at the impurity location of plane-wave solutions – the same that arise

from the poles of the Green's function - belonging to either side. The intuitive interpretation of impurity states as a simple combination of plane-waves is completely lost at higher (even) dimensions, which is seen technically by not being able to reduce Eq.(2.4) to the sum of residues of the Green's function.

In this manuscript we presented a new approach for finding bound states, which reduces the impurity problem in any dimension to 1d impurity problems, and thus allows an interpretation in terms of a small set of incoming and outgoing plane waves on a linear trajectory.

We demonstrated that the method could be efficiently used to find impurity bound states in a general band structure where the gap could have multiple minima, and a spinor structure. Our method relied on the use of the Kramers-Kronig relation, which maps the Green's function formula at any dimension, to an expression which is given again by a sum of residues corresponding to plane-wave solutions of the pure model.

Presenting a few examples, we demonstrated how our method easily lends itself to approximating lattice Hamiltonians in terms of a discrete sum of separate valley Hamiltonians. As we show, when Pauli-Villars regulators are used to provide a cut-off for valley Hamiltonians, we can still use the Kramers-Kronig relation to connect bound states with a discrete sum of plane waves. The Pauli-Villars regulators, however, add additional poles to the Green's function of the pure system, which also need to be included in the plane-wave superposition.

While we only demonstrated the method in 2d, the wavefunction matching method can be extended to any dimension. All odd dimensional systems are analogous to the 1d case with additional angular variables, and all even dimensional systems are analogous to the 2d case. This is because the wavefunction matching method is closely connected to the contour

integration, which reduces the problem to finding poles of the Green's function; the contour integration applies in odd dimensions but not in even ones. For most systems without rotational symmetry of local Hamiltonians, only a few momentum angles are necessary to complete the semiclassical interpretation of a bound state.

Chapter 3

Transport through a disordered topological-metal strip[†]

3.1 Background and Motivation

To date, topological behavior has been observed in many systems in zero magnetic field, usually by identifying topologically induced edge states. Much of the theoretical attention has been given to topological insulators, [12, 14, 78, 79, 13, 80, 81] while many of the experimental observations are of systems that are metallic, due to either doping, or midgap states [82, 83, 84, 85]. It is natural then to ask – what kind of topological behavior can a metal, or a gapless system, exhibit?

Several groups have studied the so-called topological conductor. Ref. [86] used a 2d Kane-Mele (or Haldane) topological insulator, with interstitial sites in each hexagon forming an additional trivial band to realize a topological conductor (see Fig. 3.1 for illustration). The 'parasitic' metallic band was made to overlap with the topological-band edge states. Hybridization between the topological and parasitic metallic bands changed the edge-state spectrum in a peculiar way. Edge states which overlapped in both energy and parallel momentum with bulk metallic states not only did not disappear when hybridization was in-

[†]This chapter is published in [119]

troduced, but rather, they doubled: exact edge states emerged at energies above and below the metallic band, and a finite width spectral resonance remained where the unhybridized topological edge state used to be. An additional topological conductor system was studied by Bergman[87] and Barkeshli and Qi.[88] They showed that a magneto-electric axion response (with time-reversal broken at the surface) persists even when the 3d topological insulator is doped, and Fermi-surfaces appear in its bulk, although it is no longer quantized. Similarly, Ref. [89] shows that a 3d topological metal still supports a special surface plasmon mode.

The transport properties of a topological conductor, especially in the presence of disorder, are the focus of this paper. These aspects of the topological conductor were so far mostly ignored. Several groups, however, have investigated the effects of disorder on topological insulators. It was clearly shown that a sufficient amount of disorder will close a topological gap, resulting in a metal [90, 91, 92, 93, 94, 95, 22, 21, 96]. Furthermore, it was found that disorder could even induce topological behavior in trivial semiconductors with spin-orbit coupling [54, 97, 55]. Only Ref. [98] so far also considered disorder effects in a topological-metal regime, and found that it does not qualitatively affect the non-universal magneto-electric effects found by Refs. [88, 87].

Our study concentrates on the 'parasitic metal' flavor of the topological conductor which was described above [86]. Specifically, we investigate the conductance of a topological conductor strip as a function of disorder, with its chemical potential in the energy range where edge states and the parasitic metallic band coexist. Increasing disorder will eventually localize the bulk states, and then we expect there to be rather little mixing between the bulk states and the edge states, since the wavefunction overlaps are exponentially small. In contrast, for weak disorder, where the bulk states are still mostly delocalized, the wavefunction

overlaps are much more significant, and we expect that no state will be distinguishable as an edge state.

Our results, however, are quite surprising. The edge states appear to retain their significance for essentially all disorder strengths. Their presence and distinction is manifested in the persistence of a single highly conducting channel which survives until the disorder is sufficiently strong and the topological band associated with the honeycomb subsystem is destroyed. The distinct feature of this effect is the appearance of a conductance minimum for the most conducting channel at some finite disorder (see Fig. 3.4). We characterize this conductance minimum in systems of varying width and length, as well as for several values of the model parameters.

The organization of the paper is as follows. In Sec. 3.2 we describe in detail the parasitic metal model we study. We describe the transfer-matrix method we use in Sec. 3.3. Our results, demonstrating the conductance minimum, as well as its dependence on the system parameters, are recounted in Sec. 3.4. A qualitative understanding of the effect can be obtained using a simple model, which we describe and analyze in Sec. 3.5, before making our concluding remarks in Sec. 3.7.

3.2 The Kane-Mele parasitic band model for topological conductor

We perform the disorder and transport analysis on a specific model for the topological conductor. We expect that the qualitative behavior will be independent of the specific model we employ. As mentioned in the introduction, we will use the Haldane model with interstitial sites added. We will also consider the full Kane-Mele model with Rashba interaction

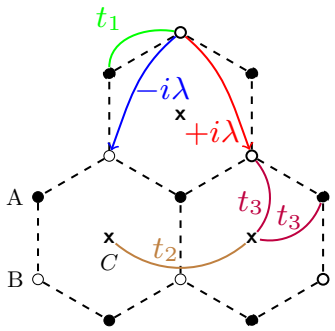

Figure 3.1: A 2d lattice model of a topological conductor. The model is based on the Kane-Mele model [12, 14] on the honeycomb lattice, which is denoted by dashed lines. The Kane-Mele model consists of nearest-neighbor hopping t_1 (green) between the two (A, B) sublattices of the honeycomb lattice (denoted by empty and filled circles, respectively), and a complex second-nearest-neighbor hopping (a spin orbit coupling term) with opposite sign when clockwise ($+i\lambda$, red) and counterclockwise ($-i\lambda$, blue), as indicated by the curved arrows in the figure. In addition to sites of the honeycomb lattice, we include a new set of sites (C) at the centers of the hexagonal plaquettes of the honeycomb lattice (denoted by cross marks). The C-sites form a triangular sublattice, and nearest-neighbor hopping between them t_2 (brown) forms a metallic band. To explore the interplay between the topological insulators' helical surface states and the bulk metallic band, we mix the two systems by allowing hopping between the C-sites and the honeycomb lattice sites, t_3 (purple).

included and find a similar behavior as for the Haldane model.

The Haldane model [99] consists of spinless electrons on the honeycomb lattice, with nearest-neighbor hopping, which gives the band structure of Graphene, and imaginary second-nearest-neighbor hopping, which opens a gap, induces a non-zero integer Chern number in the conduction and valence bands, and produces chiral edge states. To this we add a parasitic metallic band, formed by an overlayed triangular lattice of sites, which occupy the center of the honeycomb hexagons (see Fig. 3.1). Hopping between the interstitial triangular lattice sites produces a single topologically-trivial band, which overlaps in energy with the edge states of the Haldane model. We then allow the two subsystems to hybridize.

The Hamiltonian describing the combined model is

$$\begin{aligned}
\mathcal{H} &= \mathcal{H}_{Haldane} + \mathcal{H}_{met} + \mathcal{H}_{hyb} + \mathcal{H}_{dis} \\
\mathcal{H}_{Haldane} &= -t_1 \sum_{\langle ij \rangle} a_i^\dagger b_j - i\lambda \sum_{\langle\langle ij \rangle\rangle} \Big[a_i^\dagger a_j \nu_{ij} + (a \to b) \Big] + h.c \\
\mathcal{H}_{met} &= -t_2 \sum_{\langle ij \rangle} \Big[c_i^\dagger c_j + h.c. \Big] \\
\mathcal{H}_{hyb} &= -t_3 \sum_{\langle ij \rangle} \Big[c_i^\dagger a_j + c_i^\dagger b_j + h.c. \Big] \\
\mathcal{H}_{dis} &= \sum_{i, x \in \{a,b,c\}} V_i x_i^\dagger x_i \ , \qquad (3.1)
\end{aligned}$$

where i, j denote the sites of the composite honeycomb and interstitials lattice. The operators a, b denote the fermion annihilation operators on the two honeycomb sublattices (A and B), and c is the fermion annihilation operator on the triangular lattice sites C at the centers of the honeycomb plaquettes. The coefficients $\nu_{ij} = \pm 1$ determine the sign of the imaginary second-nearest-neighbor hoppings, and are defined in Refs. [12, 14], as $\nu_{ij} = \frac{2}{\sqrt{3}} \hat{z} \cdot (\hat{d}_{jk} \times \hat{d}_{ki})$, where $\hat{d}_{kj}$ is the unit vector pointing from site j to k, and k is the intermediate site between j and i. The parameter t_1 denotes the nearest-neighbor hopping on the honeycomb lattice, while t_2 denotes the nearest-neighbor hopping on the triangular lattice. Finally, t_3 is the hybridization hopping between the honeycomb and triangular lattice sites. The random on-site potential V_i on every site of the lattice (honeycomb and triangular lattice sites) has a uniform distribution between $[-W, W]$.

The single spin system we analyzed consisted of zig-zag strips of the topological conductor with the Hamiltonian (3.1). Its generic band structure is shown in Fig. 3.2. Indeed we see that the metallic band intervenes between the conduction and valence bands of the Haldane portion of the band structure. We see regions in the spectrum where in a single value of the momentum parallel to the edge, there are two edge states at energy above and

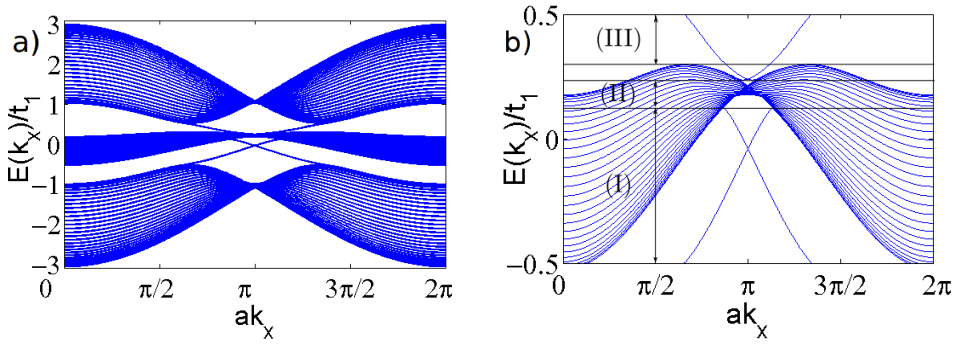

Figure 3.2: (a) Energy spectrum of the topological conductor without disorder. Bands at the top and bottom are the bulk states of the honeycomb lattice. The band in the middle is the metallic bulk from the interstitial sites. The parameters in units of t_1 are $\lambda = 0.1$, $t_2 = 0.1$, $t_3 = 0.1$, and the width of the strip is $M = 30$ zig-zag lines. (b) Zoom of the band structure in (a). Different Fermi-energy regimes are indicated. The region between (II) and (III) has the same properties as region (I).

below the metallic band. This is a manifestation of the exiling effect pointed out in Ref. [86], and indicates that the metallic band appeared on top of the edge-states branch in this region, and hybridization expelled the edge states while doubling them.

3.2.1 Rashba coupling

We have also studied the effect of adding a Rashba type spin-orbit coupling on the honeycomb lattice to our model (3.1), with the electron spin$-\frac{1}{2}$ restored. The Rashba interaction mixes between the two spin flavors as follows:

$$\mathcal{H}_R = i\lambda_R \sum_{\langle ij\rangle\alpha\beta} a^\dagger_{i\alpha}(\hat{s}_{\alpha\beta} \times \hat{d}_{ij})_z b_{j\beta} + h.c., \tag{3.2}$$

where $\hat{s}$ is the vector of Pauli matrices for the electron spin, $\hat{d}_{ij}$ is the unit vector pointing from site j to i, and α, β are spin indices.

Even with Rashba interaction included, we find the same qualitative behavior as in the spinless case described above.

3.2.2 Fermi-energy regimes

The systems' transport properties depend closely on its Fermi energy. The range of Fermi energies between the conduction and valence bands of the topological subsystem can be split into three important regions. Region I denotes the case where the edge states and metallic bands overlap in energy but not in momentum, and therefore coexist in the clean limit. Region II denotes the energy range of the parasitic metal where no edge states appear. Region III is the energy range that has only edge states. These regions are indicated in Fig. 3.2(b) for the spinless model.

3.3 Landauer formalism for the strip

In order to analyze the two-terminal transport through the topological conductor, we use the Landauer-Büttiker formalism.[100, 101, 102] We envision our system as consisting of a long strip of the topological conductor, which is disordered in a finite region (Fig. 3.3). The regions to the left and right of the disordered region form the ballistic leads, with several transverse modes. The Landauer-Büttiker formalism gives the following formula for the current flowing through the system in a two-terminal device:[103]

$$G = \frac{e^2}{h} \sum_{n,m} |T_{nm}^{LR}(E_F)|^2, \tag{3.3}$$

where $T_{nm}^{LR}(E_F)$ is the transmission coefficient for going from mode m in the left lead to mode n in the right lead at the Fermi energy, E_F. To ensure probability current conservation, it is important to note that the current associated with a scattered wave is proportional to the square of the wavefunction multiplied by the velocity. Therefore T_{nm} is given by the outgoing current amplitude, i.e., the wave amplitude times the square root of the velocity of

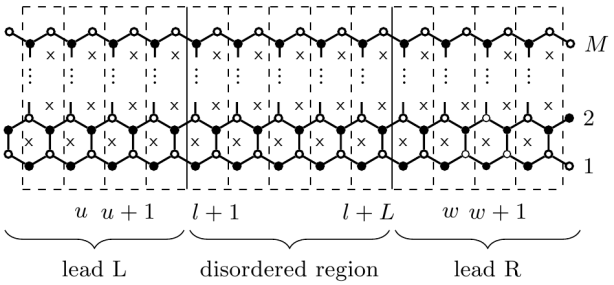

Figure 3.3: Lattice system with a width of M zig-zag lines. The disordered region of length L is the conductor which is connected to a lead on either side. Dashed rectangles show the unit cells of the strip geometry.

an electron leaving the device in mode n through one lead if the incoming current amplitude in mode m in the other lead is set to unity.

Eq. (3.3) can also be written as the sum of conductances per channel g_m:

$$G = \frac{e^2}{h} \sum_m g_m, \tag{3.4}$$

where $g_m = \sum_n |T^{LR}_{nm}|^2$ is the conductance of channel m, given by the probability that an electron entering the system in mode m is transmitted through the conductor. We find the transmission coefficients $T^{LR}_{nm}(E_F)$ using the transfer-matrix method, as described in Appendix 3.8. We note that this method, particularly when disorder is concerned, has an instability which restricts the system size possible. This instability arises due to the existence of imaginary momentum modes at the desired energy range which appear because we are exploring the conductance of the topological conductor for energies in the bulk gap of the honeycomb lattice. Indeed, the number of imaginary momentum modes due to the honeycomb subsystem increases linearly with the number of zig-zag lines in the strip, thus restricting the accessible system size.[†] Nevertheless, the transfer-matrix method provides reliable results for a range of strip sizes. These results could, in principle, be improved upon

[†]We have $2M - 1$ imaginary momentum modes due to the honeycomb system for a strip with M zig-zag lines.

by using S-matrix methods [104].

3.4 Results

We investigated the conductance of the topological conductor strip for different Fermi-energy regimes and analyzed its dependence on system and model parameters. For Fermi energies where metallic bulk and edge states coexist (region I), we find a distinct minimum in the conductance of the most conducting channel as a function of disorder strength, followed by a revival towards ballistic transport in this channel. This is a surprising feature given the mixing between bulk and edge.

3.4.1 Region I

The conductance for each channel for a Fermi energy in region I is shown in Fig. 3.4. The generic feature we find in this regime is a single highly conducting channel that persists up to large disorder and decays when disorder is presumably strong enough to close the gap of the honeycomb subsystem. For small disorder there is a sharp dip in the conductance followed by a broad maximum

3.4.1.1 Dependence on system size

In general, increasing the width of our strip has two opposing effects. One, the overlap of edge states on opposite sides of the strip is reduced and thereby the conductance should increase. Two, a wider strip hosts more bulk channels, and leakage from the edge into the bulk is increased, which reduces the conductance. Increasing the length of our strip increases the probability of electrons inside the wire being backscattered or leaking into the bulk since they travel a longer distance inside the disordered region. This should decrease

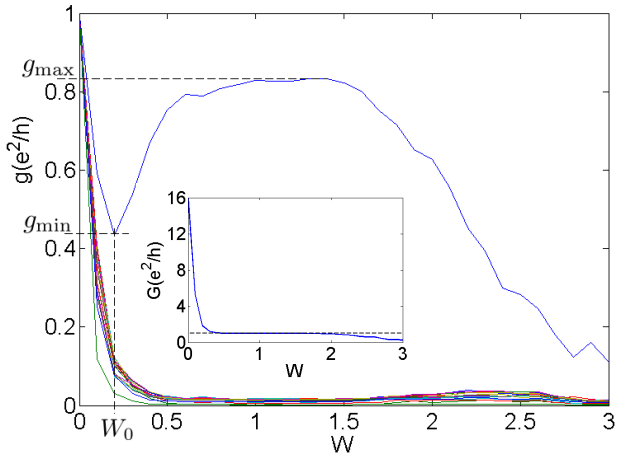

Figure 3.4: Illustration of the 'dip and recovery' feature of the edge channel conductance. Conductance g_n of different channels is plotted as a function of disorder strength W. The edge channel conductance shows a sharp minimum $g_{\min}$ at finite disorder W_0 and a broad maximum $g_{\max}$. Parameters are $E_F = 0.1$, $\lambda = t_3 = 0.1$, and $M = L = 20$. The inset shows the total conductance. The dip is no longer visible but one can see that the conductance remains at a value different from zero for a large range of disorder strengths. The dashed line marks the conductance e^2/h of a single channel.

the conductance while the net effect of changing the system width is not apparent.

The dependencies of the characteristic values of the conductance, the minimum $g_{\min}$, the maximum $g_{\max}$ at higher disorder, and the disorder strength at the minimum W_0 (cf. Fig 3.4) on the system size are given in Fig. 3.5. We find that these quantities have a rather different dependence on the system dimensions. $g_{\min}$ shows an exponential decay with increasing system length and a small increase with increasing width. The disorder strength W_0 at the minimum seems to be independent of the system width but shifts to smaller disorder values with increasing system length. $g_{\min}$, $g_{\max}$, and W_0 are (nearly) independent of the strip width, which shows that either the two opposing effects of changing the width are not very significant or that they (nearly) cancel each other for the studied parameter region.

Rather importantly, it appears that the most conducting channel recovers at high disorder and becomes effectively ballistic. The conductance maximum $g_{\max}$ seems to be in-

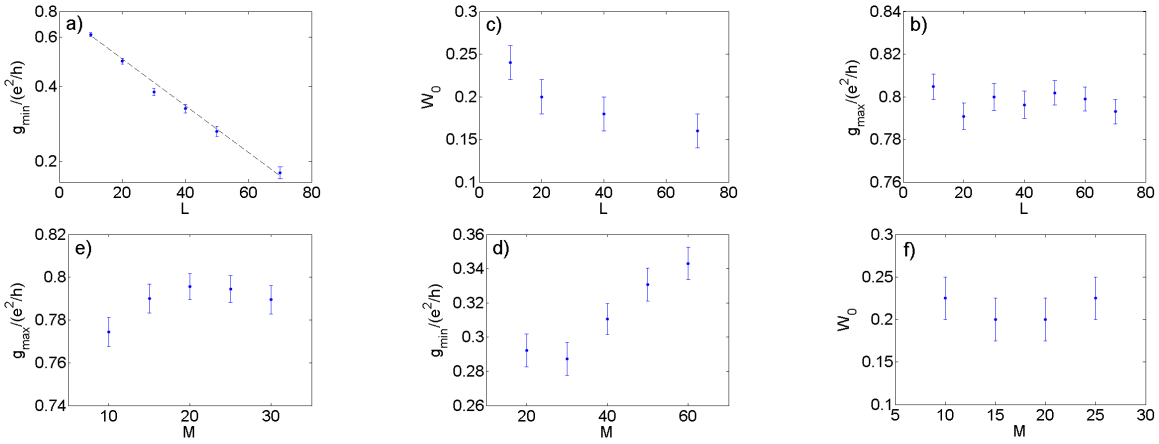

Figure 3.5: Dependence of the conductance dip and maximum on system size (Region I). (a)-(c) Dependence on length L of the system for $M = 20$. Note the log-scale on the y-axis in (a); the dashed line is a guide to the eye to emphasize the exponential dependence. (d)-(f) Dependence on system width for (d), (e) $L = 40$ and (f) $L = 20$. Parameters: $E_F = 0.1$, $\lambda = t_3 = 0.1$. While the observed feature is nearly independent of the system width, the conductance minimum decreases exponentially with system length. The maximum conductance is nearly independent of the system length, and the deviation from the quantized value presumably results from backscattering at the interface between leads and disordered region.

dependent of the system length. Its deviation from the quantized value is presumably the result of backscattering at the interface between leads and disordered wire rather than from effects inside the disordered region.

3.4.1.2 Dependence on system parameters

An increase in the coupling t_3 between the honeycomb subsystem and the triangular lattice increases the probability of electrons leaking from the edge into the localized metallic bulk states, which should reduce the conductance of the chiral edge states. Imaginary second-nearest-neighbor hopping λ is the essential ingredient for a topological phase as it opens a gap and produces chiral edge states. An increase in λ widens the gap and thereby makes the system more robust against disorder [12], which should increase the conductance and broaden the maximum.

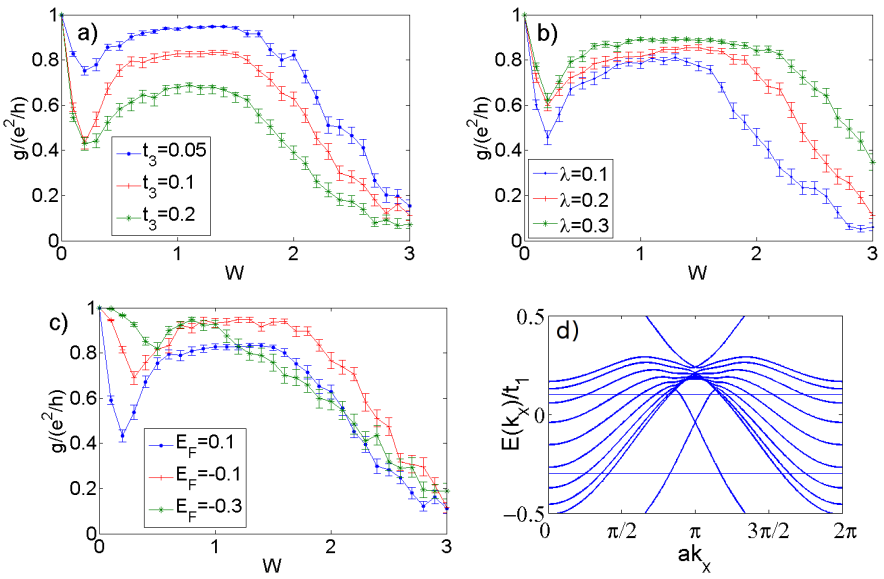

Figure 3.6: Region I. Dependence of the edge channel conductance on system parameters. Dependence on (a) hybridization t_3 ($\lambda = 0.1$, $M = 20$) and (b) second-nearest-neighbor hopping λ ($t_3 = 0.1$, $M = 10$) for $E_F = 0.1$ and $L = 20$. (c) Dependence on Fermi energy with $\lambda = t_3 = 0.1$, $M = 10$, and $L = 20$; (d) indicates the energy range from $E = 0.1$ to $E = -0.3$. Decreasing the hybridization t_3 and increasing the second-nearest-neighbor hopping λ increases the conductance over the entire disorder range. Moving the Fermi energy away from the metallic bulk has the same effect until E_F is too close to the honeycomb valence band when the characteristic feature is starting to vanish.

The dependence of the edge channel conductance on the hopping parameters λ and t_3 is illustrated in Fig. 3.6(a) and (b). We find that the characteristic shape of the conductance is left unaffected by changes in the hopping parameters of over a wide range of values. As expected, an increase in the hybridization t_3 decreases the conductance, while an increase in the second-nearest-neighbor hopping λ increases it and leads to a broader maximum due to the larger bulk gap of the honeycomb subsystem. One might think that the dependence of the conductance maximum on the hybridization t_3 contradicts our earlier conclusion that the deviation of the conductance maximum from the quantized value results from backscattering effects at the interface between conductor and leads. This is, however, not the case since, an increased coupling between the triangular and honeycomb lattices increases backscattering everywhere, including at the interface between conductor and leads, leading to the observed

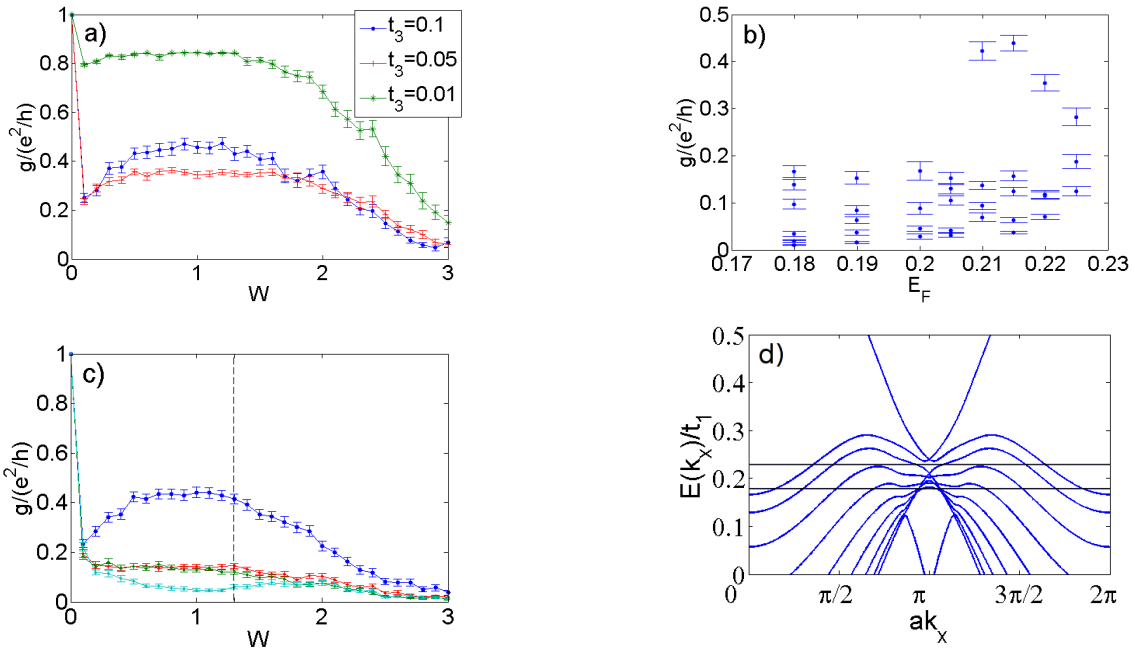

Figure 3.7: Region II. Conductance of the most conducting channel for a Fermi energy deep within the metallic band. (a) Dependence on disorder strength for different hopping strengths t_3. $E_F = 0.2$, $\lambda = 0.1$, $M = 20$, and $L = 20$. (b) Conductance of each channel at different Fermi energies. For Fermi energies between $E = 0.21$ and $E = 0.22$ a single highly conducting channel exists which is possibly connected to surface resonances. Parameters are $W = 1.3$, $\lambda = t_3 = 0.1$, $M = 10$ and $L = 20$. (c) Conductance as a function of disorder at $E_F = 0.21$ for $\lambda = t_3 = 0.1$, $M = 10$ and $L = 20$. A single channel stands out which is highly conducting at finite disorder. Dashed line indicates the disorder strength taken in (b). (c) shows the energy range from $E = 0.18$ to $E = 0.23$.

behavior.

When varying the Fermi energy within region I to values away from the metallic band (see Fig. 3.6(c)), first the conductance of the most conducting channel increases over the entire disorder range because of a decreasing number of metallic states, but the characteristic shape is unaffected. However, for Fermi energies too close to the bulk of the honeycomb lattice, the conductance starts to lose its shape. Even small disorder can in this case destroy to topological bands through partial closing of the bulk gap of the honeycomb subsystem.

3.4.2 Region II

In this region, the Fermi energy lies deep within the (trivial) metallic band. Without hybridization between the honeycomb and the triangular lattice, the edge states would traverse the bulk gap unhindered through the metallic band. For finite hybridization, however, the edge states are expelled out of the metallic band region to higher and lower energies (cf. Fig. 3.2). We would therefore expect the conductance in this regime to show bulk state behavior, i.e., rapid decay with increasing disorder. Decreasing the hybridization should recover the characteristic edge state behavior. We find, however, that even for strong hybridization $t_3 = 0.1$, for a certain range of parameters there is a conducting channel which shows the characteristic behavior of the edge channel (Fig. 3.7). This highly conducting channel exists only for a range of Fermi energies within the metallic band.

The explanation of the highly conducting channel in this regime is consistent with the notion of leftover spectral resonances of the edge states, once they are absorbed by the bulk. When the surface bands are pushed away from the metallic band they leave behind a finite lifetime surface resonance in place of the original surface states (these are referred to as 'ghosts' in Ref. [86]).

3.4.3 Region III

In this region the Fermi energy lies above the metallic band and below the conduction band of the honeycomb subsystem. The conductance is only determined by the edge states and we would expect a quantized value up to a certain critical disorder strength as in the case without a metallic band. However, for Fermi energies very close to the metallic band there is a residual effect from the metallic bulk states and the conductance shows a small dip in the otherwise quantized conductance (Fig. 3.8).

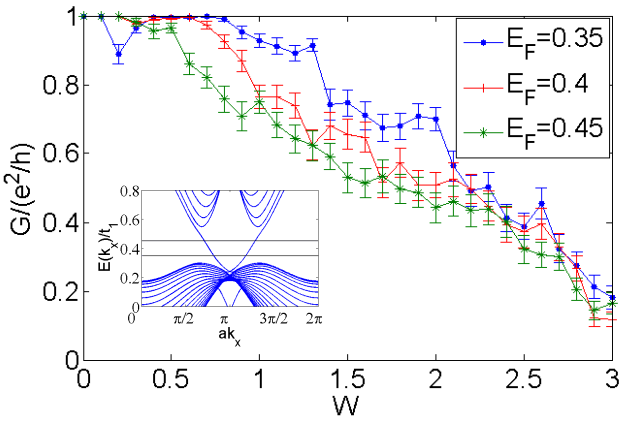

Figure 3.8: Region III. Conductance of the edge state for different Fermi energies. Parameters are $\lambda = t_3 = 0.1$ and $M = L = 20$. Inlet indicates the energy range form $E = 0.35$ to $E = 0.45$. At Fermi energies close to the metallic bulk ($E_F = 0.35$), disorder induced states above the bulk band still lead to a dip in the conductance. The closing of the honeycomb bulk gap due to disorder quickly decreases the conductance in the entire energy range.

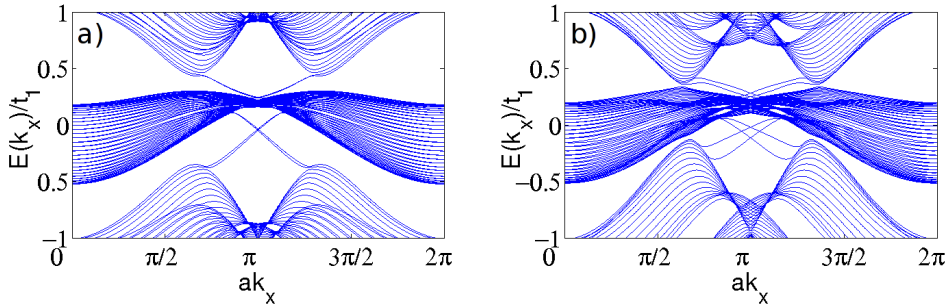

Figure 3.9: Band structure with Rashba coupling (a) $\lambda_R = 0.1$ and (b) $\lambda_R = 0.3$. Parameters are $\lambda = t_3 = 0.1$, and $M = 30$. Rashba coupling reduces the band gap of the honeycomb subsystem.

Disorder closes the bulk gap of the honeycomb subsystem by creating new bulk states above the valence and below the conduction band, and the conductance decreases rapidly with disorder for larger Fermi energies. In addition, disorder also creates new metallic states above the metallic band. These new states then coexist with edge states as in region I which explains the observed small dip at small disorder.

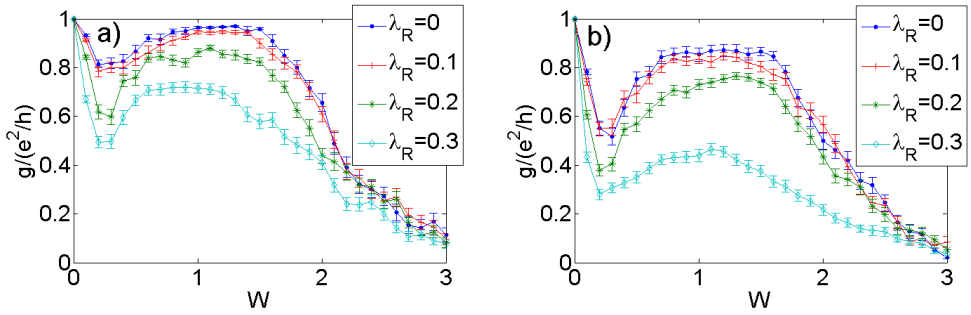

Figure 3.10: Region I with Rashba coupling. Conductance of one edge channel for (a) $t_3 = 0.05$ and (b) $t_3 = 0.1$ for different Rashba coupling strengths λ_R. Parameters are $E_F = 0.05$, $\lambda = 0.1$, $M = 10$, and $L = 20$. We plotted only a single spin orientation for readability. Rashba coupling overall reduces the conductance. The effect is enhanced for larger hybridization between the honeycomb and metallic subsystems.

3.4.4 Rashba coupling (Region I)

We also considered a spinful version of (3.1) with Rashba type spin-orbit coupling included between nearest-neighbor sites of the honeycomb subsystem (3.2). We considered the effects of spin-independent disorder only. As shown in Fig. 3.9, aside from the doubling of the bands, small Rashba coupling does not change the band structure dramatically. For large Rashba coupling the edge bands are clearly separated in momentum and the structure of the metallic band changes significantly. The bulk gap of the honeycomb subsystem is reduced such that region III vanishes. However, we find that Rashba coupling does not affect the characteristic shape of the edge channel conductance as seen in Fig. 3.10. Increasing Rashba coupling decreases the conductance over the entire disorder range but leaves the distinct 'dip and recovery' behavior of the conductance intact. As for the model without Rashba coupling, decreasing the hybridization t_3 between honeycomb and triangular lattice increases the conductance.

3.5 Interpretation and toy model

The nature of the conductance dip found in the previous section can be qualitatively understood using a simple toy model. Our toy model consists of a single chiral mode that is mixed, due to disorder, with multiple bulk modes. This model neglects inter-edge scattering. We further approximate the most conducting channel from one side to the other as the sum of two incoherent contributions: edge-to-edge $g_{e-e} = \frac{e^2}{h}|T_{e,e}|^2$ (through just the edge channel) and bulk-to-edge $g_{e-b} = \frac{e^2}{h}\sum_{m\neq e}|T_{e,m}|^2$ transport.

The transmission coefficient between mode m in the left lead to mode n in the right lead, can be computed from the retarded Green's function connecting these two modes [103]

$$T_{nm} = i\hbar\sqrt{v_n v_m}\mathcal{G}_{nm} \ , \tag{3.5}$$

where v_n is the electron velocity in mode n at the Fermi energy. For the sake of brevity we will take $\hbar \equiv 1$ from this point forward.

Indeed, since this system has a chiral mode, strictly speaking, it will always have a total conductance bigger than the single channel, e^2/h. Nevertheless, we will only be interested in the conductance involving the bare chiral edge states. So if the chiral mode manages to wander deep into the bulk due to the disorder, we will ignore its conductance. This is consistent with the numerics, since under these circumstances one would no longer be able to separate the system into two independent parts, each involving a single chiral mode.

The main findings in this section are the following. Coupling between edge and bulk channels in general leads to a distinct 'dip and recovery' feature with increasing disorder strength. Even for the simple model of a single bulk mode coupled to the edge mode via a single contact, this behavior can be observed (cf. Fig. 3.12). Near the minimum, the

main contribution to the conductance stems from the bulk-to-edge channel. As a result, this channel is largely responsible for the dependence on the system size of the conductance minimum. For the case of multiple bulk modes we find a good agreement with the results from the numerical analysis in Sec. 3.4. $g_{\min}$ is found to decrease exponentially with the system length and to be roughly independent of the system width (cf. Figs. 3.13, 3.14). Nevertheless, the toy model is limited. It does not capture reflection within a mode or the closing of the bulk gap with increasing disorder because it assumes a fixed number of bulk and edge modes at a certain Fermi level. The non-quantized conductance plateau and subsequent decrease of the conductance can thus not be analyzed within this model. The toy model is also not suitable to describe the region II calculation where edge and bulk modes are coupled already in the clean limit, and as such are not well separated contrary to what we assume in the model.

In the following we study the toy model in detail, explicitly calculate the conductance for different system lengths and widths, and use the results to explain the origin of the conductance dip.

3.5.1 Toy model and Green's functions

Consider a system with a single chiral edge mode and multiple bulk modes. We assume that the chiral edge mode can only hybridize with the bulk when impurities are introduced. The hybridization strength will serve as a proxy for disorder strength.

We describe our system with the action

$$\begin{aligned} S = \int \frac{d\omega}{2\pi} dx dx' \Big[& \chi^\dagger(x) G^{-1}(x-x') \chi(x') \\ & + \psi_n^\dagger(x) F_{nm}^{-1}(x-x') \psi_m(x') \\ & - \Big[\chi^\dagger(x) V_n(x) \psi_n(x) + h.c. \Big] \Big] \ , \end{aligned} \tag{3.6}$$

where the field $\chi(x)$ represents an electron at position x in the bare edge mode, and the fields $\psi_n(x)$ represent an electron at x in bulk mode n. In addition, G and F denote the bare edge and bulk state propagators, respectively, and V denotes the random potential scattering between the edge state and bulk channels. We will adopt the uniform distribution of random potential strength. The bare propagators are translationally invariant in the direction through the length of the strip (hence the dependence only on the relative coordinate $x-x'$), while the impurity scattering $V(x)$ is completely local. All terms depend on frequency ω, which for the sake of brevity has been kept implicit. The Einstein summation convention has been used for the bulk channel indices n, m. In momentum space the form of the propagators is

$$\begin{aligned} G^{-1}(k,\omega) &= \omega + i\eta - v_e k \\ F_{n,m}^{-1}(k,\omega) &= \delta_{n,m} \left[\omega + i\eta - \frac{k^2}{2\mathcal{M}_n} + \mu_n \right] \ , \end{aligned} \tag{3.7}$$

where $\eta > 0$ is infinitesimal and positive, and $\mathcal{M}_n$ and μ_n are the effective mass and the chemical potential, respectively, in bulk mode n. Fourier transforming from momentum

space to real space we find

$$\begin{aligned} G(x, E_F) &= \int_{-\infty}^{+\infty} G(k, E_F) e^{ikx} = -\frac{i}{v_e} e^{ik_e x} \theta(x) \\ F_{n,m}(x, E_F) &= \int_{-\infty}^{+\infty} F_{n,m}(k, E_F) e^{ikx} \\ &= \frac{-i}{v_{b,n}} e^{ik_{b,n}|x|} \delta_{n,m} \ , \end{aligned} \tag{3.8}$$

where $v_{b,n} = k_{b,n}/\mathcal{M}_n$, and $k_{b,n} = \sqrt{2\mathcal{M}_n(E_F + \mu_n)}$ is the Fermi momentum in the bulk mode n, and $k_e = \frac{E_F}{v_e}$. The chiral mode propagator G reflects a single propagation direction. $G(x)$ is zero when $x < 0$, and this reverses when we take $\eta < 0$ for the advanced propagator. For the bulk modes, we assume F is diagonal, neglecting the mixing of different bulk conduction channels.

The quantity $V(x)$ is not the bare random potential, but rather matrix elements between bulk modes and the edge state, due to disorder scattering, and we therefore assume they are uncorrelated random complex variables. The random phase captures the random location of the focal points of impurity induced edge-bulk scattering, and makes sure our results are not affected by momentum conservation. In this manner we take into account the diffusive nature of the bulk, while still using the translationally invariant form of the bulk propagator F.

We discretize the x coordinate into $i = 1 \ldots N$, as illustrated in Fig. 3.11, and set $V_n(i = 1) = V_n(i = N) = 0$ to represent clean leads so that we can still separate in our calculations the edge conduction channel from all the others. For $i \neq 1, N$ we take $V_n(j) = t_{j,n} e^{\phi_{j,n}}$. Now G and F are both square matrices with sizes $N \times N$ and $NM \times NM$, respectively, where M is the number of channels (and the width of the lattice model of our strip). In contrast, V_n is a non-square matrix of dimensions $N \times NM$. Discretizing x

requires one subtle change to the chiral propagator G in (3.8)

$$\begin{aligned} G(x_i - x_j, E_F) &= -\frac{i}{v_e} e^{ik_e(x_i - x_j)} \theta(x_i - x_j) \\ F_{n,m}(x_i - x_j, E_F) &= -\frac{i}{v_{b,n}} e^{ik_{b,}|x_i - x_j|} \delta_{n,m} \ , \end{aligned} \tag{3.9}$$

where the step function $\theta(x)$ at $x = 0$ is defined to be $1/2$. To find the transmission coefficients we seek, we will need to calculate the Green's function for electrons starting out at the left lead $i = 1$ and coming out at the right lead $i = N$, at the Fermi energy

$$\begin{aligned} \mathcal{G}_{e,e}(x = N, x' = 1) &= \langle \chi^\dagger_{i=N} \chi_{i=1} \rangle \\ \mathcal{G}_{e,m}(x = N, x' = 1) &= \langle \chi^\dagger_{i=N} \psi_{m,i=1} \rangle \ . \end{aligned} \tag{3.10}$$

where we specified two contributions: electron from edge to edge mode, $\mathcal{G}_{e,e}$, and electron from bulk mode m to edge mode, $\mathcal{G}_{e,m}$. With the position index suppressed for the sake of brevity, our action is of the form

$$S = \int d\omega \left[\begin{pmatrix} \chi^\dagger & \psi^\dagger \end{pmatrix} \begin{pmatrix} G^{-1} & -V \\ -V^\dagger & F^{-1} \end{pmatrix} \begin{pmatrix} \chi \\ \psi \end{pmatrix} \right] \ . \tag{3.11}$$

Next we want to invert the matrix, in order to find the components of the full Green's

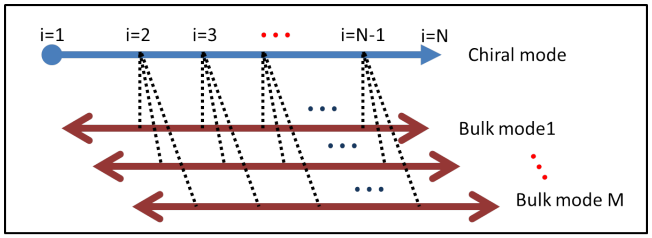

Figure 3.11: Illustration of the toy model. Bulk modes are independent of each other since we assume that the bulk channels describe the eigenmodes of the diffusive bulk. The edge mode couples to the bulk through $(N-2)$ scattering sites, giving in total $(N-2)M$ couplings $V_n(j)$. The coupling strength and phase are uniformly distributed.

function $\mathcal{G} = \begin{pmatrix} G^{-1} & -V \\ -V^\dagger & F^{-1} \end{pmatrix}^{-1}$. We find

$$\begin{aligned} \mathcal{G}_{e,e} &= \frac{1}{G^{-1} - VFV^\dagger} \\ \mathcal{G}_{e,m} &= \mathcal{G}_{e,e} V_n F_{nm} = \mathcal{G}_{e,e} VF \\ \mathcal{G}_{m,e} &= \mathcal{G}_{m,n} V_n^* G \\ \mathcal{G}_{n,m} &= \left(\frac{1}{F^{-1} - V^\dagger G V} \right)_{n,m} , \end{aligned} \tag{3.12}$$

where we have used the Einstein summation convention. The non-square matrices $\mathcal{G}_{e,m}$ and $\mathcal{G}_{m,e}$ are the Green's function elements that capture the bulk-edge and edge-bulk mixing, respectively; $\mathcal{G}_{e,e}$ and $\mathcal{G}_{n,m}$ are the renormalized Green's functions for the edge and bulk modes, respectively.

As we will see in what follows, the simple toy model already affords us a qualitative understanding of the conductance dip, and its dependence on the system dimensions.

3.6 Conductance dip of different system size

3.6.0.1 Single contact with single bulk case

It is instructive to first consider the case of a single bulk mode $m = b$ and a single impurity. In this case we take $N = 3$ and $M = 1$, and for simplicity we take $k_e = k_b = k_F$, and $V = te^{i\phi}$. From Eqs. (4.1,3.12), we can show that

$$\begin{aligned}
\mathcal{G}_{b,b}(N,1) &= \frac{e^{ik_F L}}{v_b}\frac{1}{1+t'^2/2} \\
\mathcal{G}_{e,e}(N,1) &= \frac{e^{ik_F L}}{v_e}\frac{1-t'^2/2}{1+t'^2/2} \\
\mathcal{G}_{b,e}(N,1) &= \frac{e^{ik_F L}}{\sqrt{v_e v_b}}\frac{t'}{1+t'^2/2} \\
\mathcal{G}_{e,b}(1,N) &= \frac{e^{ik_F L}}{\sqrt{v_e v_b}}\frac{t'}{1+t'^2/2}\ ,
\end{aligned} \tag{3.13}$$

where $L = (N-1)a = 2a$, a is the lattice spacing, and $t' = t/\sqrt{v_e v_b}$ is a dimensionless coupling strength. From these we find the conductances

$$\begin{aligned}
g_{e-e} &= \frac{e^2}{h}\left[\frac{1-t'^2/2}{1+t'^2/2}\right]^2 \\
g_{e-b} &= \frac{e^2}{h}\left[\frac{t'}{1+t'^2/2}\right]^2\ .
\end{aligned} \tag{3.14}$$

We can now easily see that $g_{e-e} = \frac{e^2}{h}$ for both the clean limit $t' = 0$ and the infinite disorder limit $t' \to \infty$. In between there is a minimum of $g_{e-e} = 0$ at $t' = \sqrt{2}$. In contrast, g_{e-b} starts at zero for $t' = 0$, and rises to a maximum value of $g_{e-b} = \frac{1}{2}\frac{e^2}{h}$ at $t' = \sqrt{2}$, before decaying back down to zero. Note that the Fermi velocities only rescale the disorder strength, and did not otherwise influence the conductance behavior.

Finally using Eq. (3.5) we find all the different contributions to the conductance (edge/bulk-edge/bulk), as plotted in Fig. 3.12. Fig. 3.12(a) shows the conductance of

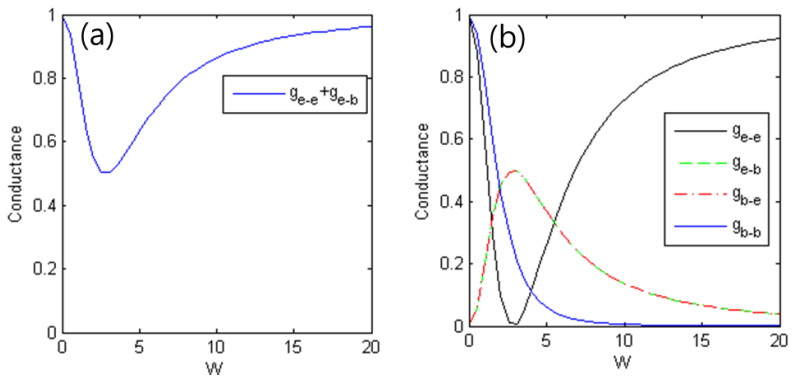

Figure 3.12: Conductance contribution via different channels as a function of coupling strength (x-axis) for the system of a single chiral and bulk mode with a single coupling: from edge to edge g_{e-e}, edge to bulk g_{b-e}, bulk to edge g_{e-b}, and bulk to bulk g_{b-b}. The edge to edge conductance has a minimum at finite disorder before recovering to the quantized value. The conductance is in units of $\frac{e^2}{h}$.

the strip, consisting of adding up the edge-to-edge and bulk-to-edge channels. Fig. 3.12(b) shows the possible individual conductances. Two points are noteworthy: (i) In the strong disorder limit, the conductance of edge-to-edge channel converges to unity. (ii) At the conductance dip minimum, the biggest contribution to the conductance comes from the bulk-edge channel. In other words, at strong disorder, the edge-edge channel conductance recovers to unity even without accounting for the localization of the bulk, and the size dependence of the conductance near the dip will arise from the bulk-edge channel contribution, and will be rather independent of the edge-edge channel behavior.

3.6.0.2 Multiple bulk modes and impurities

Consider now a general system of length N (i.e., having $N-2$ scattering sites), and width (bulk mode number) M. The Green's function components we need to calculate to find the transmission coefficient $\mathcal{G}(N,1)$ can be found in closed form. In particular, the edge-edge

Green's function is found to be

$$\mathcal{G}_{e,e}(N,1) = -\frac{i}{v_e} e^{ik_e(N-1)} \frac{det(G_0^T - \mathcal{V}F\mathcal{V}^\dagger)}{det(G_0 + \mathcal{V}F\mathcal{V}^\dagger)} \,, \tag{3.15}$$

where $G_0 = G(k_b = 0)$ in Eq. (4.1) and $\mathcal{V}_n(x_j) = (-1)^j e^{ik_e x_j} V_n(x_j)/2v_e$, such that $(\mathcal{V}F\mathcal{V}^\dagger)_{i,j} = \sum_{n,m} \mathcal{V}_n(i) F_{n,m}(i,j) \mathcal{V}_m(j)^*$. The derivation of this result is somewhat involved, and so we defer its details to a future publication.[105] More generally, for $j \neq 1$, we can show that

$$\mathcal{G}_{e,e}(N,j) = i\frac{(-1)^j}{2v_e} e^{ik_e(N-j)} \frac{det(G_0^T - \mathcal{V}F\mathcal{V}^\dagger)_{j^{th}}}{det(G_0 + \mathcal{V}F\mathcal{V}^\dagger)} \tag{3.16}$$

where $(A)_{j^{th}}$ indicates the j^{th} row of the matrix is replaced by a vector $(a)_j = -\frac{i}{v_e}(1 - \delta_{1,j} - \delta_{N,j}) = -\frac{i}{v_e}(0,1,1,\ldots,1,0)$. Concomitantly, the Green's function bulk-edge mixing component is

$$\mathcal{G}_{e,m}(N,1) = \sum_n \sum_{j=2}^{N-1} \mathcal{G}_{e,e}(N,j) V_n(j) F_{n,m}(j,1), \tag{3.17}$$

which is the sum of the $(N-2)$ Green's functions from clean bulk to renormalized chiral mode.

3.6.0.3 Length dependence

The conductance minimum $g_{\min}$ is expected to drop exponentially with the system's length, as shown in Fig. 3.5(a). The toy model's results are shown in Fig.3.13. Within our toy model, the length dependence of $g_{\min}$ is attributed to the mixed edge-bulk contribution to the conductance g_{e-b}. Indeed, we approximate the edge-related conduction as an incoherent

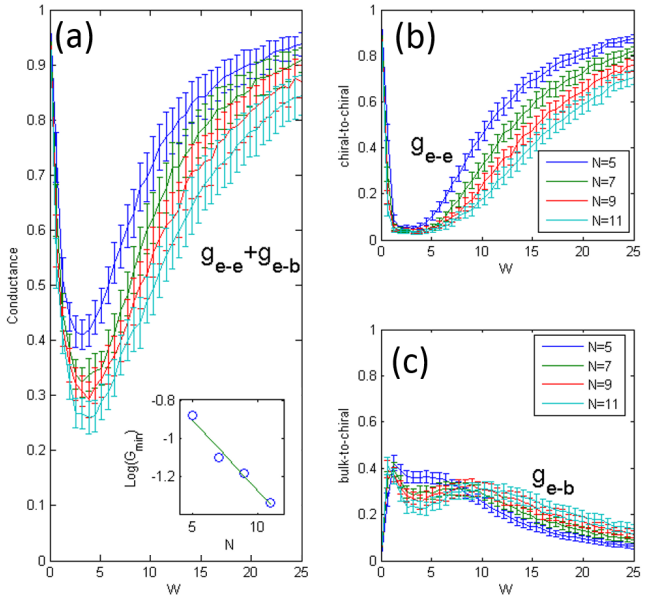

Figure 3.13: (a) Sum of the conductances of chiral-to-chiral (b) and bulk-to-chiral (c) channels for M=4 and N=5 (blue), 7 (green), 9 (red), and 11 (cyan) for $k_e = \frac{1.4\pi}{a}$ and $k_b = \frac{1.2\pi}{a}$. The inset in (a) shows the exponential decay of the minimum conductance with system length in agreement with the numerical calculation in Fig. 3.5(a). The conductance is in units of $\frac{e^2}{h}$.

sum of two contributions: conductance of electrons entering and leaving the strip in an edge state, g_{e-e}, and entering as bulk states, but leaving the strip as edge electrons, g_{e-b}. Even with multiple scatterers, g_{e-e} behaves as Eq. (3.15) indicates: it drops down from unity (in units of $\frac{e^2}{h}$) to zero at moderate disorder, then rises back to unity at strong disorder. In Fig. 3.13(b) we see that the minimum g_{e-e} is independent of the system length. Therefore, the only possible source of the $g_{\min}$ dependence on the system length must come from g_{e-b}, which starts at zero for the clean limit, rises for moderate disorder, then peaks and decays as we go to strong disorder (see Fig. 3.13(c)). The inset in Fig. 3.13(a) shows that the conductance g_{e-b} depends exponentially on the number of scattering points, and hence on the length of the system.

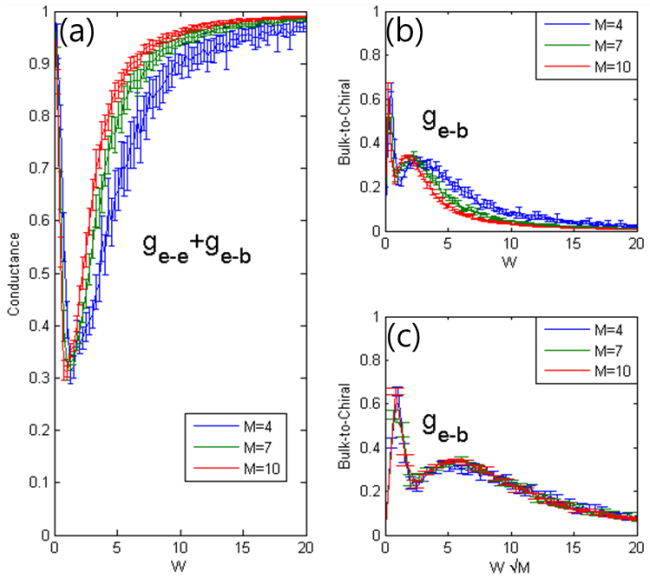

Figure 3.14: (a) Sum of conductance of chiral-to-chiral (b) and bulk-to-chiral (c) channels for N=5 and M=4 (blue), 7 (green), 10 (red) for $k_e = \frac{1.4\pi}{a}$ and $k_b = \frac{1.2\pi}{a}$. The conductance minimum is unaffected by changes is the system width in agreement with the results of the numerical calculation. c) Renormalizing the disorder strength by $\sqrt{M}$, g_{e-b}, which is the dominant contribution to the conductance in the region of the minimum, becomes independent of the system width. The conductance is in units of $\frac{e^2}{h}$.

3.6.0.4 Width dependence

We now explore the width dependence of the conductance through the edge states. To this end, we can use a simple approximation $\mathcal{V}F\mathcal{V}^\dagger \approx \langle \mathcal{V}F\mathcal{V}^\dagger \rangle$. This stems from the fact that $\langle (\mathcal{V}F\mathcal{V}^\dagger)^n \rangle / (\langle \mathcal{V}F\mathcal{V}^\dagger \rangle)^n \to 1$ when the number of bulk modes goes to infinity $M \to \infty$. This holds as long as the distribution of the random matrix elements $V_n(j)$ has a finite variance. Our approximation is therefore good when there is a large number of bulk modes $M \gg 1$, and we can then write

$$\langle \mathcal{G}_{e,e}(N,1) \rangle \simeq -\frac{i}{v_e} e^{ik_e(N-1)} \frac{det(G^T - \langle \mathcal{V}F\mathcal{V}^\dagger \rangle)}{det(G + \langle \mathcal{V}F\mathcal{V}^\dagger \rangle)} \,. \tag{3.18}$$

A similar expression holds for $\mathcal{G}_{e,e}(N, j \neq 1)$ as well.

The width dependence of the conductance can now be deduced from

$$\left(\left\langle \mathcal{V} F \mathcal{V}^\dagger \right\rangle\right)_{ij} = \frac{(-1)^{i+j}}{4v_e^2} e^{ik_e(x_i - x_j)} \sum_{nm} F_{n,m}(i,j) \left\langle V_n(i) V_m(j)^* \right\rangle \tag{3.19}$$

$$= \frac{(-1)^{i+j}}{4v_e^2} e^{ik_e(x_i - x_j)} \sum_{nm} F_{n,m}(i,j) \delta_{ij} \delta_{nm} W^2 \tag{3.20}$$

$$= \frac{1}{4v_e^2} \delta_{ij} W^2 \sum_{n} F_{n,n}(i,i) \sim M \delta_{ij} W^2 \,, \tag{3.21}$$

where the variance of the disorder is the disorder strength W squared. From this we see that the dependence on M can be absorbed into W,

$$W_{\text{eff}} = \sqrt{M} W \,. \tag{3.22}$$

As a consequence we expect that increasing the width (increasing M) only shifts the minimum to different disorder strength W_0, and does not change $g_{\min}$.

This simple dependence on M turns out to work quite well when applied to the toy model. Fig. 3.14(a) shows the conductance through the chiral mode for different system widths, M. The minimum conductances in the plots are indeed all similar, consistent with the numerical results shown in Fig. 3.5(d). The conductance is dominated by the bulk-to-chiral channel (Fig. 3.14(b)). Furthermore, scaling the disorder strength by $\sqrt{M}$, the three lines of Fig. 3.14(b) collapse onto a single line in Fig. 3.14(c). Only the width of the minimum, and not its depth, is affected by the channel number.

3.7 Conclusions and summary

In this manuscript we explored the transport signatures in a topological conductor phase. The particular realization of a 2d topological conductor we considered here had an edge

state originating in the high-energy bands, overlapping in energy (but not in momentum) with a trivial band at the Fermi energy (see the spectrum in Fig. 3.2). This model should suffice to capture the generic qualitative features of the non-protected topological aspects of topological conductors.

To find topological signatures, we calculated the two-terminal conductance through a topological conductor strip in the presence of disorder in the form of a random on-site chemical potential. Our results clearly show that even when a bulk gap is absent, the edge states, which are no longer protected, maintain their individuality and dominate the transport in the strip. Inspecting the effects of disorder on all the conducting channels of the topological conductor, a single channel clearly stands out (see Fig. 3.4). The most conducting channel in the strip has a conductance which initially decays rapidly as we increase disorder strength, but then reaches a minimum, and then recovers to a value consistent with ballistic transport through the disordered region. The dip and recovery features single out the topological edge channel, and show that even when the system is gapless, its capacity for nearly dissipationless transport is restored once disorder suppresses transport through the bulk.

The origin of the 'dip and recovery' features (Fig. 3.4) presumably has to do with localization effects in the bulk. Intuitively, as the bulk states become less transparent, the edge state, which cannot localize since it is chiral, reemerges to dominate transport. To gain a better qualitative understanding of the main features in our numerics, we developed a simple toy model, consisting of a single chiral mode that can randomly scatter to several regular channels. The model assumes that the bulk is diffusive, and does not invoke localization explicitly. Disorder strength is encoded in the random scattering strength between the chiral edge and the bulk. The diffusive nature of the bulk is taken into account by using

random phases in the edge-bulk scattering elements. Despite its simplifications, this model demonstrates that generically the edge-edge scattering contribution to the conductance g_{e-e} shows the 'dip and recovery' behavior (see Figs. 3.12, 3.13).

Thus it appears that the full-fledged Anderson localization, which is necessary to eliminate conductivity in the bulk, is not necessary for the revival of the edge state conductance. Rather, the dip and recovery feature appears to be guaranteed once a separate chiral mode is present, assuming it is unable to scatter to its counter-propagating partner. In the numerics, we do have both edge channels, but because their wave functions essentially do not overlap, disorder can not produce direct scattering between them. Note, however, that it appears that the 'dip and recovery' feature may not occur when the edge state overlaps in energy, and therefore can hybridize with the bulk states of its progenitor topological band.

The unique transport features in topological conductor strips will have additional signatures. First, we note that the results we presented here, when applied to a spinful electron system, rely on time-reversal invariance, and require that no scattering occurs between the counter-propagating, opposite-spin modes on the same edge. Therefore, when moderate disorder is present, and the strip conductance is dominated by the descendant of the edge channel, the conductance of the strip would be strongly suppressed by a magnetic (Zeeman) field normal to the Rashba spin direction. Such a Zeeman field opens up a gap in the edge states, pushing them away from the Fermi energy, in which case the edge state no longer contributes to transport. The highly conducting mode we found would then no longer contribute to the overall conductance through the strip, which will now be purely diffusive, with no remnant of ballistic transport. Magnetic impurities at the edge would have a similar destructive effect. Second, probing the current density in the sample would disclose that in moderate disorder the conduction is dominated by regions near the edge.

Probing these effects experimentally would rely on materials or quantum wells having a band structure similar to the one considered here: a metallic band coexisting at the same energy with the edge states of a different band.

The 'dip and recovery' feature arising in transport due to disorder was shown here to appear in a non-interacting 2d system. It is interesting to ask how these features would change when considering Coulomb interactions. This could also be explored within the toy model we presented, by promoting the electronic modes to Luttinger liquids with interaction between the various modes. We could then also consider a more complete model containing the chiral modes on both sides of the strip, and follow the mixing between them explicitly. Similarly, one could ask about similar resurgence of edge physics in a 3d topological conductor. Instead of conductance, however, the appropriate topological signatures in 3d should be the Kerr effect rotation angle, which encodes the unique response of topological edge states to an oscillating electro-magnetic field (see also Ref. [21]).

The work presented in this manuscript adds to the notion that topological behavior has distinct and strong signatures even in the absence of protection due to a band gap. This observation, as articulated also in Refs. [87, 88, 95], significantly extends the class of systems (and materials) in which topological effects can be found.

3.8 Appendix: Transfer-matrix method

In this section, we will demonstrate a way to calculate the transmission coefficients T_{nm}^{LR} of our system using the transfer-matrix method.[106]

Naively, all we have to do to calculate the transmission coefficients through our system is first find the basis of modes in the clean limit (the modes in the leads) $\psi_n(x)$, then starting with an electron in just one of the (clean-limit) modes in the left lead $\psi_n(x = au)$ (cf.

Fig. 3.3), propagate the wavefunction through the dirty sample, and calculate its weight in the various modes of the (clean) right lead $\psi(x = aw) = \sum_m T^{LR}_{nm}\psi_m(x = aw)$. These weights are precisely the transmission coefficients.

In practice, we run into some difficulties. Namely, the calculated $\psi(x = aw)$ contains weight in some unphysical exponentially growing modes $\sim e^{+|\kappa|x}$, not just in the propagating modes. As a consequence, we have to perform a more complicated numerical procedure.

The main steps of the calculation are the following: After determining the transfer matrix, we calculate the eigenvalues and -vectors of the transfer matrix which correspond to the possible modes and wavefunctions in the leads. For computational convenience we start the calculation in lead R. Propagating one of these wavefunctions backwards through the system using the transfer matrix gives us a wavefunction in lead L which is a superposition of all possible wavefunctions in the leads, i.e., a superposition of all eigenvectors of the transfer matrix including unphysical (exponentially increasing) modes. Next, in order to determine the transmission coefficients, we need to find a superposition of only physical modes in lead L which, after propagation through the system, leads to a superposition of one right-moving mode with weight one and decaying modes in lead R (cf. Fig. 3.15). To find the necessary coefficients of the modes in lead L, we propagate a superposition of one right-moving mode with weight one and all decaying modes backwards through the system and choose the coefficients of the decaying modes such that the unphysical modes in lead L are canceled by destructive interference. Doing this for all right-moving modes gives us information about all transmission channels and we can determine the transmission coefficients T^{LR}_{nm} for arbitrary modes n and m using probability current conservation.

The lattice model of the topological conductor is illustrated in Fig. 3.3. The system is a honeycomb strip with a width of M zig-zag lines with an overlayed triangular lattice

with sites that occupy the centers of the honeycomb hexagons. The unit cell is chosen as explained in Fig. 3.3 with dashed rectangles indicating the unit cells. A region with a length of L unit cells constitutes the disordered topological conductor. It is connected to two perfect ballistic leads, one on each side.

In order to determine the transfer matrix, the Hamiltonian given by Eq. (3.1), which only connects sites within neighboring unit cells (cf. Fig. 3.3), can be written as

$$\mathcal{H} = \sum_u \mathbf{c}_u^\dagger (\mathbf{H}_{u,u-1}\mathbf{c}_{u-1} + \mathbf{H}_{u,u}\mathbf{c}_u + \mathbf{H}_{u,u+1}\mathbf{c}_{u+1}), \tag{3.23}$$

where

$$\mathbf{c}_u^\dagger = \begin{pmatrix} (a_{u,1})^\dagger & (b_{u,1})^\dagger & (c_{u,1})^\dagger & \dots & (b_{u,M})^\dagger \end{pmatrix}$$

is the vector of all electron creation operators in unit cell u, as indicated in Fig. 3.3. The matrices $\mathbf{H}_{u,w}$ describe hopping from unit cell w to unit cell u.

Starting with the Schrödinger equation one can find a recursive relation for the wave-functions as

$$\mathbf{M}_u \cdot \begin{pmatrix} \Psi_{u+1} \\ \Psi_u \end{pmatrix} = \begin{pmatrix} \Psi_u \\ \Psi_{u-1} \end{pmatrix}, \tag{3.24}$$

with the transfer matrix

$$\mathbf{M}_u = \begin{pmatrix} 0 & \mathbf{I} \\ \mathbf{A}_u & \mathbf{B}_u \end{pmatrix}, \tag{3.25}$$

where

$$\mathbf{A}_u = -\left(\mathbf{H}_{u,u-1}\right)^{-1}\mathbf{H}_{u,u+1},$$

$$\mathbf{B}_u = \left(\mathbf{H}_{u,u-1}\right)^{-1}\left(E_F\mathbf{I} - \mathbf{H}_{u,u}\right).$$

$\Psi_u = \begin{pmatrix} \psi^A_{u,1} & \psi^B_{u,1} & \psi^C_{u,1} & ... & \psi^B_{u,M} \end{pmatrix}^T$ is a vector of the amplitudes on all sites in one unit cell and E_F our chosen Fermi energy. Using appropriate initial wavefunctions and Eq. (3.24), we can calculate the wavefunction in every unit cell of our system. Our initial condition is an incoming right-moving wave in lead L such that there are only transmitted waves in lead R and the initial and reflected waves in lead L. Once we have the wavefunctions in both leads we can determine the transmission matrix. For computational convenience we calculate backwards through the system starting in lead R.

The first step is therefore to determine the eigenmodes of lead R which are given by the eigenvalues λ_n and eigenvectors $\mathbf{\Psi}_n$ of the transfer matrix $\mathbf{M}_w$ for w in lead R. For propagating modes $\lambda_n = e^{ik_n a}$ and the eigenvalue is a root of unity, while otherwise the amplitude is increasing or decaying. Depending on the energy level we choose, we get p pairs of propagating modes (left and right moving) with eigenvalues $e^{\pm ik_n a}$ (a is the length scale of our system and will be set to 1) and eigenvectors $\mathbf{\Psi}_{\pm k_n}$ and q pairs of exponentially increasing or decaying modes (resulting from imaginary momentum modes) with eigenvalues $e^{\pm\kappa_n a}$ and eigenvectors $\mathbf{\Psi}_{\pm\kappa_n}$. The physical eigenmodes of lead R are the starting points for Eq. (3.24). Taking w to be a unit cell in lead R and u a unit cell in lead L, as illustrated in Fig. 3.3, we can determine $2p+q$ physical wavefunctions in lead L using

$$\mathbf{\Psi}^L_{k_n} = \begin{pmatrix} \Psi_{u+1} \\ \\ \Psi_u \end{pmatrix} = \mathbf{M}_{u+1}\cdot ... \cdot \mathbf{M}_{w-1}\cdot\mathbf{M}_w\cdot\mathbf{\Psi}^R_{k_n} \tag{3.26}$$

and analogously for $\mathbf{\Psi}^L_{\kappa_n}$. These wavefunctions have to be a superposition of all possible eigenvectors of $\mathbf{M}$ in the leads and can be written as

$$\mathbf{\Psi}^L_{k_n} = \sum_{m=1}^{2p} \alpha_{k_m,k_n} \mathbf{\Psi}^R_{k_m} e^{iNk_m} + \sum_{m=1}^{2q} \alpha_{\kappa_m,k_n} \mathbf{\Psi}^R_{\kappa_m} e^{N\kappa_m} \tag{3.27}$$

and analogously for $\mathbf{\Psi}^L_{\kappa_n}$ with $N = w - u$ and $k_{p+n} = -k_n$, $\kappa_{q+n} = -\kappa_n$ for brevity. $\alpha_{q_m,q'_n} \in \mathbb{C}$ is the coefficient of mode q_m in lead L when mode q'_n was propagated from lead R to lead L.

Since we know that the eigenvalues of the transfer matrix are of the form $e^{\pm ik}$ and $e^{\pm\kappa}$, the momenta k_m and κ_m can be calculated from the eigenvalues of $\mathbf{M}_w$. Eq. (3.27) forms a linear system of equations with a unique solution for the variables α_{q_m,q'_n}. In general all the coefficients α_{q_m,q'_n} will be nonzero, that includes the coefficients of the unphysical modes. Although we now essentially have corresponding incoming flux amplitudes in the left lead and outgoing flux amplitudes in the right lead, we cannot calculate the transmission coefficients from those because the picture is not physical. The wavefunction in the left lead contains exponentially increasing contributions. Instead of choosing a single outgoing mode in the right lead (which by itself gives us unphysical contributions in the left lead) we take a superposition of physical modes, i.e., propagating and exponentially decaying modes, in the right lead. The coefficients of this superposition have to be chosen such that (after propagating backwards through the strip) the unphysical modes in the left lead cancel each other. However this cancellation only works for a superposition of one propagating mode with all the exponentially decaying modes. This procedure is illustrated in Fig. 3.15. We are not interested in the left-going modes in the right lead since we are looking at the case of an incoming wave from the left. To cancel the unphysical modes in the left lead we need

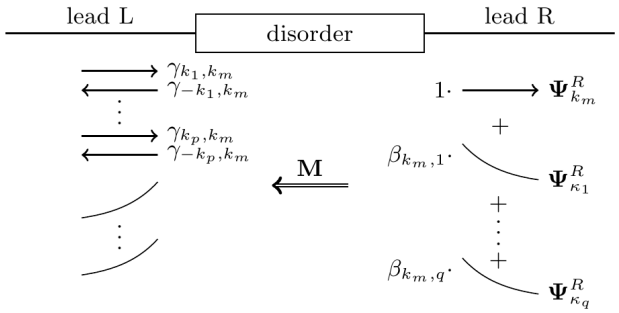

Figure 3.15: Considering a superposition of physical modes in lead R, one can cancel the unphysical modes in lead L by destructive interference. The coefficients $\beta_{k_m,n}$ have to be chosen such that, after backwards propagation, the exponentially increasing modes in lead L have zero weight. The coefficients $\beta_{k_m,n}$ are given by Eq. (3.28). The coefficients γ_{q_n,q'_m} of the resulting superposition (of only physical modes) in lead L are given by Eq. (3.29).

to solve p systems of equations like (cf. Fig. 3.15)

$$\begin{pmatrix} \alpha_{\kappa_1,k_m} & \alpha_{\kappa_1,\kappa_1} & \cdots & \alpha_{\kappa_1,\kappa_q} \\ \vdots & \vdots & \vdots & \vdots \\ \alpha_{\kappa_q,k_m} & \alpha_{\kappa_q,\kappa_1} & \cdots & \alpha_{\kappa_q,\kappa_q} \end{pmatrix} \begin{pmatrix} \beta_{k_m,0} \\ \beta_{k_m,1} \\ \vdots \\ \beta_{k_m,q} \end{pmatrix} = \begin{pmatrix} 0 \\ \vdots \\ 0 \end{pmatrix}, \tag{3.28}$$

one for each k_m corresponding to a mode propagating to the right. The $\beta_{k_m,n}$ are the coefficients of the superposition in lead R that we want to determine. The index k_m denotes which propagating mode is part of the superposition. The index n shows which mode belongs to this coefficient, 0 for the propagating mode and $n = 1...q$ for the q decaying modes. The α_{q_n,q'_m} are calculated from Eq. (3.27) and are the coefficients of the unphysical modes that we want to cancel. α_{κ_1,k_m} is the coefficient of the (exponentially increasing) mode κ_1 in the lead L when the (propagating) mode k_m was propagated from lead R backwards through the system. The set of linear equations (3.28) is under determined and we can therefore choose $\beta_{k_m,0} = 1$ without loss of generality. The coefficients $\beta_{k_m,0}$ and $\beta_{k_m,n}$ give us a superposition of physical modes in lead R which is caused by a superposition of

only physical modes in lead L. This is illustrated in Fig. 3.15 where the entire system is now made up out of only physical modes. In order to determine the transmission coefficients, we are interested in the coefficients γ of the propagating modes in lead L. Taking into account the necessary superpositions, the coefficients for the right-moving modes are given by

$$\gamma_{k_n,k_m} = 1 \cdot \alpha_{k_n,k_m} + \sum_{l=1}^{q} \beta_{k_m,\kappa_l} \alpha_{k_n,\kappa_l} \tag{3.29}$$

γ_{k_n,k_m} is the coefficient of mode k_n in the left lead when the outgoing mode in the right lead is k_m. The transmission coefficients can now be calculated by requiring probability current conservation. This leads to the following system of equations:

$$\begin{pmatrix} T_{11}^{LR} & T_{12}^{LR} & \dots & T_{1p}^{LR} \\ T_{21}^{LR} & \ddots & & \\ \vdots & & & \vdots \\ T_{p1}^{LR} & & \dots & T_{pp}^{LR} \end{pmatrix} \cdot \mathbf{\Gamma} = \mathbf{V}, \tag{3.30}$$

with $\mathbf{\Gamma}_{nm} = \gamma_{k_n,k_m} \sqrt{|v_{k_n}|}$ and $\mathbf{V}_{nm} = \sqrt{|v_{k_n}|}\, \delta_{nm}$. $v_{k_n} = \frac{1}{\hbar} \frac{\partial E}{\partial k}|_{k=k_n}$ is the velocity of mode k_n. The T_{nm} are the transmission coefficients with $|T_{nm}^{LR}|^2$ the probability that an electron coming in through mode k_m is transmitted through the conductor into mode k_n.

Chapter 4

Non-perturbative expression of leaky chiral mode †

4.1 Background and Motivation

Interest in the behavior of chiral modes on the boundary of 2d insulating systems has been growing in past years. In particular, such modes are always present on the boundaries of topological states such as topological insulators [12, 107, 108, 109, 81, 110, 111], and quantum Hall samples [26, 112, 113, 114]. For example, an important consequence is that zero-temperature electron transport along an edge of a topological insulator will have a quantized conductance, if time-reversal symmetry is not broken. To describe realistic systems, however, it is always necessary to take into account imperfections, such as potential disorder or impurity scattering [115, 116, 117], or even the presence of a bulk states. Interestingly, chiral edge states might even be the result of adding disorder to trivial spin-orbit coupled semiconductors, and the appearance of the so-called Anderson topological insulator [54, 68, 55]. In the course of such a disorder-induced transition, the system necessarily carries extended bulk states as well as chiral modes. Such topological metal systems show a non-trivial behavior of transport properties[118, 119].

†This chapter is published in [105]

Disorder effects in non-chiral 1d systems, e.g., localization phenomena due to the introduction of random potential, were also studied theoretically and computationally for many years (for a review see, e.g. [120]). While it is computationally straightforward to confirm localization of wave functions in 1d single particle systems, the theoretical studies of localization properties and transitions in 1d and higher have proven challenging. A scaling theory suggested in [49] shows the localization of 1d and 2d at any weak disorder in the system. For a given distribution of random disorder, an upper bound on localization length was found in [121]. Powerful disorder averaging techniques are available, such as the supersymmetry approach [122] and the replica trick [123], which induces an effective non-linear sigma field theory. Also, in strongly disordered systems such as random spin chains, trap models, and random polymers, the role of quenched disorder on quantum and thermal fluctuations has been studied by the strong disorder renormalization group method (for a review see, e.g. [124]).

Considerable advances, however, can be made by simple and, arguably, more reliable algebraic methods, when considering a 1d chiral mode connected to a bulk. Such an approach could apply to intrinsic chiral edge modes, and even to localization in non-chiral 1d systems. An example of such a simplification is the subject of the present paper.

In this manuscript, we present a closed-form Green's function of a chiral mode coupled to a bulk and its applications. In section 4.2, the Green's function is expressed as a ratio of determinants, and involving in the Green's function of the bulk and arbitrary couplings between the chiral mode and bulk. An application to disordered strict 1d wire is introduced in section 4.3. The 1d wire is modeled in terms of two chiral modes, and the "det-formula" is applied in the presence of onsite impurities. The disorder averaging of transmission coefficient, the log of transmission coefficient, and the reflection coefficient are worked out

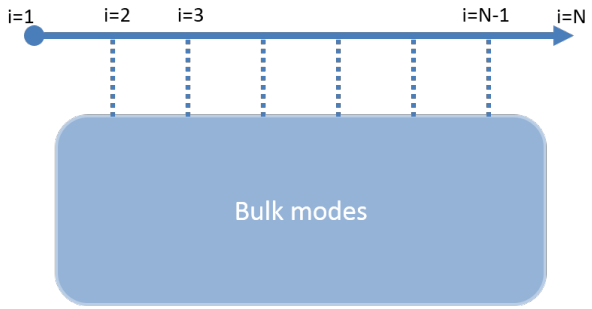

Figure 4.1: A chiral mode is coupled to a bulk that may contain localized and propagating modes. The chiral Green's function from site $i = 1$ to $i = N$ is found for a given coupling between the chiral and bulk modes expressed in matrix T in real space, and bulk Green's function G_B in section 4.2.

in the subsections. In section 4.4, the phase picked up by the chiral mode in quantum hall fluid system is studied. We conclude in section 4.5. Additional details of disorder averaging of the log of transmission coefficient are worked out in Appendix 4.6.

4.2 Green's function of a leaky chiral mode

In this section, we derive an analytic expression for the Green's function between the two ends of a chiral mode. Throughout the paper, we assume that the scattering happens at discrete locations, allowing us to turn the problem into a matrix problem. We therefore only need the Green's function of the right-moving chiral mode at the scattering positions:

$$(G_R)_{nm} = \frac{1}{iv_F} e^{ik|n-m|a} \theta(n-m), \tag{4.1}$$

which in real-space basis is a left lower triangular matrix. We define $\theta(0) = 1/2$, and $n, m = 1, \cdots, N$ are indices of scattering sites. We assume that the scattering centers are equally spaced. This assumption can be lifted by modifying the translational operator $\hat{U}_t$ introduced later. The chiral Green's function renormalized by the coupling with the bulk modes represented by G_B can be obtained by writing the Hamiltonian of the system in

block form and using standard block inversion, with the result:

$$\mathcal{G} = \frac{1}{G_R^{-1} - VG_BV^\dagger}. \tag{4.2}$$

For convenience, we pull out phase factors from the Green's function, writing it as:

$$G_R = \hat{U}_t^\dagger G_{R0} \hat{U}_t. \tag{4.3}$$

Here $\hat{U}_t = e^{-ika\hat{n}}$, where $\hat{n}$ is the position operator along the wire, $\hat{n}_{nm} = \delta_{mn} n$, and G_{R0} is a Green's function with zero wave number in Eq.(4.1), which can be thought of the chiral Green's function with the phase factors gauged out and without coupling to bulk modes. Due to the particular form of G_{R0}, we can write its inverse explicitly, finding that:

$$G_{R0}^{-1} = -4v_F^2 \hat{U}_s G_{R0} \hat{U}_s^\dagger, \tag{4.4}$$

where a sign operator $\hat{U}_s = e^{i\pi\hat{n}}$ is introduced. We note that G_R, as well as its inverse G_R^{-1}, are lower triangular matrices. With these definitions, we now have:

$$\mathcal{G} = \frac{1}{4v_F^2} \hat{U}_{st} \frac{1}{-G_{R0} - \mathcal{T} G_B \mathcal{T}^\dagger} \hat{U}_{st}^\dagger, \tag{4.5}$$

where $\hat{U}_{st} = \hat{U}_s \hat{U}_t$, and $\mathcal{T} = \hat{U}_{st} V / 2v_F$.

Our main interest in this paper is to get the Green's function between two ends, described by $\mathcal{G}_{N1}$. To do so, we use Cramer's rule, i.e., $C_{ij}^{-1} = (-1)^{i+j} M_{ji} det(C)^{-1}$, where M_{ji} is the

ji'th minor of the matrix C, together with Eq.(4.5), and find:

$$\mathcal{G}_{N1} = (-1)^N \frac{e^{i(N-1)ka}}{4v_F^2} \left(\frac{1}{G_{R0} + \mathcal{T} G_B \mathcal{T}^\dagger} \right)_{N1} \tag{4.6}$$

$$= (-1)^N \frac{e^{i(N-1)ka}}{4v_F^2} \frac{(-1)^{N+1} M_{1N}}{Det[G_{R0} + \mathcal{T} G_B \mathcal{T}^\dagger]}. \tag{4.7}$$

where (1,N)'th minor of the matrix is:

$$M_{1N} = minor_{1N}[G_{R0} + \mathcal{T} G_B \mathcal{T}^\dagger] \tag{4.8}$$

$$= 4iv_F(-1)^N Det[-G_{R0}^T + \mathcal{T} G_B \mathcal{T}^\dagger] \tag{4.9}$$

$$= 4iv_F Det[G_{R0}^T - \mathcal{T} G_B \mathcal{T}^\dagger]. \tag{4.10}$$

Here, we manage to express the minor in the symmetric form of the denominator in Eq.(4.7). The derivation is detailed in Fig.4.2. As a result, the renormalized Green's function is expressed in terms of the ratio of two determinants:

$$\mathcal{G}_{N1} = \mathcal{G}_{N1}^{(0)} \frac{Det[G_{L0} - \mathcal{T} G_B \mathcal{T}^\dagger]}{Det[G_{R0} + \mathcal{T} G_B \mathcal{T}^\dagger]}, \tag{4.11}$$

where $\mathcal{G}_{N1}^{(0)} = e^{i(N-1)ka}/iv_F$, and G_{R0}^T is replaced by G_{L0}, which is the Green's function of a left-moving chiral mode: $(G_{L0})_{mn} = (G_{R0})_{nm}$. Note that $\mathcal{T}$ is essentially the coupling matrix between the chiral and bulk modes, but rescaled by the Fermi velocity and multiplied by the sign and translational matrices. We thus obtained the renormalized chiral Green's function coupled with bulk modes in a compact and closed form. The additional factor is expressed as a ratio of two determinants, and we find it particularly advantageous to perform disorder averaging. We continue the detailed calculation of transmission of disordered 1d

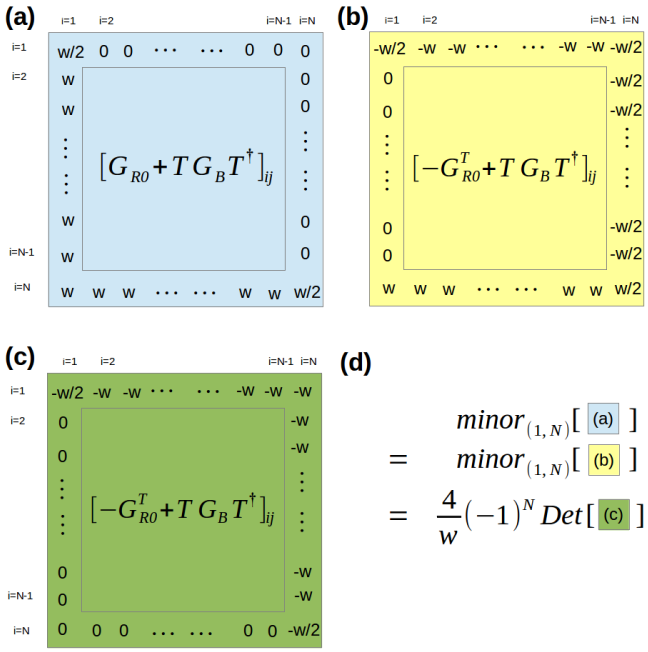

Figure 4.2: The derivation of Eq.(4.10) is detailed with diagrams using $w = 1/iv_F$, for simplicity. Note that $\mathcal{T}G_B\mathcal{T}^\dagger$ has no element in the outer part of the matrix since there is no coupling at site $i = 1$ and $i = N$. The (1,N)'th minor of matrix (a) is the same with that of matrix (b), which is obtained by subtracting the last row of (a) from all other rows. Then, consider matrix (c) which has the outer elements of $-G^T_{R0}$. Its determinant is the same with the (1,N)'th minor of matrix (b) up to a constant as expressed in (d).

wire in the following section.

4.3 Example: disordered 1d wire

Our first example is a 1d wire with random onsite potentials first considered by Anderson[43]. The physical quantity of interest is the transmission coefficient of the system, as it is the most relevant for 1d and quasi 1d wires connected to leads[125], rather than the conductance of system, which is the ratio of the transmission and reflection coefficients. Our expression for the Green's function is not directly applicable to this problem, since the 1d wire does not contain a chiral mode explicitly. Nevertheless, we show in section 4.3.1 that the disordered 1d wire can be equivalently modeled by two chiral modes with the couplings through quan-

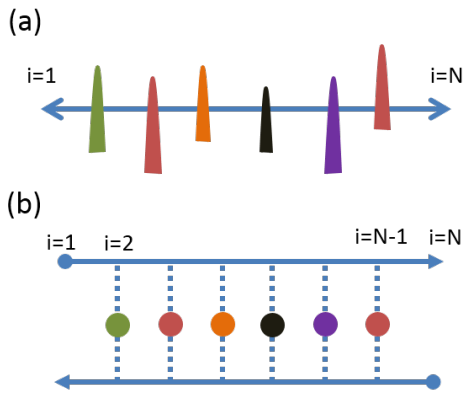

Figure 4.3: (a) 1d wire with random onsite impurities. (b) An equivalent model of (a). The 1d clean bulk mode is described by two chiral modes, and random impurities are modeled by the coupling between two chiral modes through quantum dots with random onsite potentials (see Eq.(4.17)).

tum dots. We then apply the det-formula in section III.B to find the transmission coefficient for a given realization of random impurities. In section III.C, the disorder averaging of the transmission coefficient T, as well as of $log(T)$, and $1/T$ are computed. We also show that our approach to computing the transport quantities provides a clear picture for why the log of the transmission is a well behaved statistical quantity. Plus, it simplifies the process of disorder averaging.

4.3.1 Alternative model of disordered 1d wire

In this section we consider an ordinary 1d wire, which, using the results of the previous section, we decompose into two chiral modes coupled through a series of quantum dots. The system contains $(N-2)$ impurities with random strengths which is expressed by matrix α in real space (see Fig.5.2):

$$(\alpha)_{nm} = \delta_{nm}\alpha_n, \tag{4.12}$$

where index n is for the scattering sites. The first site, $n = 1$, and the last site, $n = N$, play the role of leads connected to the disordered wire from both ends.

The Green's function through the disordered 1d wire can be cast in a T-matrix formulation as:

$$\mathcal{G}_{N1} = \left(G + G \frac{1}{I - \alpha G} \alpha G \right)_{N1}, \tag{4.13}$$

where G is the free Green's function on the wire. We consider a system with N scattering points and placed at intervals of length a. Only positions on the wire at which scattering occurs contribute in a non trivial way in Eq.(4.13), and therefore we can replace the continuous G by a $N \times N$ matrix with elements:

$$(G)_{nm} = \frac{1}{iv_F} e^{ik|n-m|a}. \tag{4.14}$$

Now consider chiral Green's functions with left and right moving modes. One can relate them to the non-chiral Green's function by:

$$G = G_R + G_L. \tag{4.15}$$

where the left-moving chiral Green's function is similar to Eq.(4.1) with m and n exchanged in the step function, so that $(G_L)_{mn} = (G_R)_{nm}$. Next, we express the Green's function through the disordered 1d system, Eq.(4.13), in terms of the chiral modes:

$$\mathcal{G}_{N1} = \left(G_R + G_R \frac{1}{I - \alpha(G_R + G_L)} \alpha G_R \right)_{N1}. \tag{4.16}$$

Note that except for the Green's function in the T-matrix, the Green's function G on the

left and on the right have been replaced by G_R, which is justified since $(G)_{nm} = (G_R)_{nm}$ for $n > m$, while α_n is nonzero only at the points $N - 1 > n > 1$.

Finally, we obtain a model of a disordered 1d wire by introducing quantum dots replacing random onsite potentials, and the two chiral modes are connected to the dots through a coupling matrix V:

$$\alpha = V G_Q V^\dagger, \tag{4.17}$$

where G_Q is Green's function of quantum dots possessing random chemical potentials. By substituting the random potential matrix α in Eq.(4.16), $\mathcal{G}_{N1}$ now describes the Green's function of the right-moving chiral mode, as in Fig.2 (b).

Note that all of our following analysis is performed in the parameter range where the dispersion relation can be treated as linear. More specifically, consider a dispersion relation at some momentum:

$$\begin{aligned} E(k) &= E(k_0) + v_F(k - k_0) + u_2(k - k_0)^2 \\ &+ u_3(k - k_0)^3 + O(k^4). \end{aligned} \tag{4.18}$$

To justify the validity of the det-formula, which is based on the linear dispersion of a chiral mode, we must have $k - k_0 \ll \Delta k_c = \mathrm{Min}(v_F/u_2, \sqrt{v_F/u_3})$. Therefore, the impurity strength should be less then $v_F \Delta k_c$. On the other hand, we introduce the limit of weak and strong impurity strength by the expansion parameters and the number of impurities:

$$\alpha \ll \frac{v_F}{N} \text{ (weak disorder)} \tag{4.19}$$

$$\frac{v_F}{N} \ll \alpha \ll v_F \Delta k_c \text{ (strong disorder)}. \tag{4.20}$$

In the following sections, we refer to the weak and strong limits of impurity strength according to the above determination. For some systems with $v_F/N \geq v_F \Delta k_c$, we disregard the strong disorder regime.

4.3.2 Green's function through disordered 1d wire

Consider a 1d wire with a particular disorder realization, Fig.5.2(b). We would like to compute the transmission through the wire from site $i = 1$ to $i = N$, and therefore the *bulk* corresponding to the one in Fig.4.1 is the quantum dots coupled with a left-moving chiral mode. The Green's function of the *bulk* is:

$$G_B = \frac{1}{G_Q^{-1} + V^\dagger G_L V} \tag{4.21}$$

where the left-moving chiral Green's function renormalizes the Green's function of quantum dots. Note the hopping matrix V has now a different order compared to Eq.(4.2). For our purpose, it is convenient to consider with a simplified form:

$$G_L = -\frac{1}{4v_F^2} \hat{U}_{st}^\dagger G_{L0}^{-1} \hat{U}_{st} \tag{4.22}$$

Define $\mathcal{T}_2 = \hat{U}_{st}^\dagger V/2v_F$, plug in the left-moving chiral Green's function back to the bulk Green's function expression:

$$G_B = \frac{1}{G_Q^{-1} + \mathcal{T}_2^\dagger G_{L0}^{-1} \mathcal{T}_2} \tag{4.23}$$

Next, let us work with the renormalized Green's function for this bulk system. Eq.(4.11) is reduced to:

$$\frac{\mathcal{G}_{N1}}{\mathcal{G}^{(0)}_{N1}} = \frac{Det[G_{L0} - \mathcal{T}G_B\mathcal{T}^\dagger]}{Det[G_{R0} + \mathcal{T}G_B\mathcal{T}^\dagger]} \tag{4.24}$$

$$= \frac{det[G_{L0}(\mathcal{T}G_B\mathcal{T}^\dagger)^{-1} - I]}{det[G_{R0}(\mathcal{T}G_B\mathcal{T}^\dagger)^{-1} + I]} \tag{4.25}$$

$$= \frac{Det[G_{L0} - (I - G_{L0}\hat{U}_t^2 G_{L0}^{-1}\hat{U}_t^{\dagger 2})\mathcal{T}G_Q\mathcal{T}^\dagger]}{Det[G_{R0} + (I + G_{R0}\hat{U}_t^2 G_{L0}^{-1}\hat{U}_t^{\dagger 2})\mathcal{T}G_Q\mathcal{T}^\dagger]} \tag{4.26}$$

$$= \frac{Det[G'_{L0} - R\mathcal{T}G_Q\mathcal{T}^\dagger]}{Det[G'_{R0} + \mathcal{T}G_Q\mathcal{T}^\dagger]} \tag{4.27}$$

where in the second equality the determinant with lower case is designated as the determinant of matrix excluding the boundary elements. Next, the inverse of $\mathcal{T}G_B\mathcal{T}^\dagger$ is expressed using the relation $\mathcal{T}_2\mathcal{T}^{-1} = \hat{U}_t^{\dagger 2} = e^{i2ka\hat{n}}$ and $\mathcal{T}G_Q\mathcal{T}^\dagger$ recovering a determinant of a whole matrix. In the last equality, new Green's functions have been defined:

$$G'_{R0} = \frac{1}{G_{R0}^{-1} + \hat{U}_t^2 G_{L0}^{-1}\hat{U}_t^{\dagger 2}} \tag{4.28}$$

$$= -\frac{1}{4v_F^2}\hat{U}_{st}\frac{1}{G_R + G_L}\hat{U}_{st}^\dagger \tag{4.29}$$

where $G_R + G_L$ is the Green's function of a clean 1d wire Hamiltonian with nearest neighbor hopping, and therefore the inverse is a tridiagonal matrix. On the other hand,

$$G'_{L0} = \frac{1}{I + G_{R0}\hat{U}_t^2 G_{L0}^{-1}\hat{U}_t^{\dagger 2}} G_{L0} \tag{4.30}$$

$$= G'_{R0}G_{R0}^{-1}G_{L0} \tag{4.31}$$

and

$$R = \frac{1}{I + G_{R0}\hat{U}_t^2 G_{L0}^{-1}\hat{U}_t^{\dagger 2}}(I + G_{L0}\hat{U}_t^2 G_{L0}^{-1}\hat{U}_t^{\dagger 2}) \quad (4.32)$$

$$= I - G'_{R0}(I + G_{R0}^{-1}G_{L0})\hat{U}_t^2 G_{L0}^{-1}\hat{U}_t^{\dagger 2}. \quad (4.33)$$

Studying the second term on the right side of Eq.(4.33), equal to $(I - R)$, we find that, $(I - R)_{nm} = 0$ for $n > 1$, and $(I - R)_{11} = 1$. As a result, we find that $(R)_{11} = 0$ and $(R)_{nn} = 1$ for $n \neq 1$. Finally, one can verify that:

$$(G'_{L0} + RG'_{R0})_{nm} = \frac{1}{4i}\delta_{n,1}\delta_{m,N}, \quad (4.34)$$

and the renormalized Green's function is reduced to:

$$\begin{aligned} \frac{\mathcal{G}_{N1}}{\mathcal{G}_{N1}^{(0)}} &= Det\left[(G'_{L0} + RG'_{R0})/(G'_{R0} + \mathcal{T}G_Q\mathcal{T}^\dagger) - R\right] \\ &= \frac{1}{Det[I + \mathcal{T}G_Q\mathcal{T}^\dagger G_{R0}'^{-1}]} \\ &= \frac{1}{Det[I - \alpha(G_R + G_L)]} \end{aligned} \quad (4.35)$$

using the notation previously defined in the alternative model. A Green's function of a similar form was discovered by Thouless[126], and used to obtain the density of state. Once the transmission of a 1d disordered system for particular disorder realization is written in this way, the analytic manipulation becomes easier and the disorder averaging is rendered accessible as we present in the next sections.

4.3.3 Disorder averaging

The ability to analytically perform disorder averaging for observable quantities can provide vital insights to the behavior of disordered systems. Although a purely 1d system is not experimentally accessible (with the exception, perhaps, of cold atoms[127]), there have been numerous theoretical studies of disorder in 1d due to its relative simplicity compared to quasi 1d and higher dimensional systems. For example, the disorder averaged resistance is most interesting and many works have been focused on the scaling behavior with respect to system size [128, 129, 130, 131, 132]. The log of the transmission was also a focus of much study, as it is a statistically well behaved quantity, which follows the central limit theorem [129, 133, 134, 135, 136]. Previous approaches [137, 138, 136], however, are mostly limited to weak disorder. With our reduced determinant expression for the transmission, we can simply show why the log of the transmission has a well defined probability distribution, and we also painlessly obtain the next order correction of $\log(T)$ in the appendix so that the localization length can be estimated at moderate disorder strength.

Finally, we computed the disorder averaged transmission coefficient of system; few studies of this quantity exist, as it is difficult to obtain its disorder average[138]. For a system without leads, a conductance is a transmission over resistance. But, as discussed earlier, the transmission coefficient is an experimentally more relevant quantity since one cannot measure the conductance without leads [125]. The disorder-averaged transmission will be particularly interesting for a quasi 1d system due to its universal conductance fluctuations [139, 140]. In the following subsections we perform disorder averaging of transmission, its log, and resistance.

4.3.3.1 Transmission coefficient: $\overline{T}$

In this section we find an analytic expression for the transmission coefficient of a disordered wire in the weak disorder limit, and then perform disorder averaging. The explicit expression of the transmission obtained here will be used in later sections. Note that the conductance measured in experiments also involves the connected leads, and therefore the transmission considered here is directly relevant to conductance even for a strict 1d system [125]. One can express the transmission for a particular disorder realization using transfer matrix methods. The resistance is related to a product of transfer matrices, and is thus relatively easy to disorder average, while the transmission is its inverse, which is harder to average. Group-theoretical approaches [141, 138] were suggested to perform the disorder average of the transmission, with some success in the weak disorder limit. We present here an approach that enables obtaining disorder averaging in a simpler fashion, and can possibly be generalized to spatially correlated disorder distribution.

In the weak disorder limit we make use of the Green's function(Eq.(4.35)) to obtain the transmission coefficient through the disordered wire, $T = |\mathcal{G}_{N1}|^2$. The determinant can be perturbatively expanded using $det(I + O) = exp(Tr(O - O^2/2 + \cdots)$. In our case, the matrix O is simply $-\alpha(G_R + G_L)$. We now consider the traces:

$$(O)_{nn} = -\frac{\alpha_n}{iv_F} \tag{4.36}$$

$$(O^2)_{nn} = -\sum_m \frac{\alpha_n \alpha_m}{v_F^2} e^{2ika|n-m|}. \tag{4.37}$$

We see that the diagonal elements of O are purely imaginary, and therefore the TrO term just provides a phase to the Green's function and the transmission coefficient is unchanged by the first order term. In contrast, the diagonal elements of O^2 possess a non-vanishing

real part, and therefore the leading order contribution in the weak impurity limit.

For a given realization of impurity strengths $\{\alpha\}$, we have the transmission coefficient:

$$T(\{\alpha\}) = e^{-Tr\left[\sum_{m=1}^{M_{up}} \frac{(-1)^{m+1}}{m}(O^m+O^{*m})\right]}, \tag{4.38}$$

$$\simeq \frac{1}{exp(-Tr(O^2+O^{*2})/2)}, \tag{4.39}$$

$$= \frac{1}{exp(\sum_{n,m}\alpha_n\alpha_m cos(2ka|n-m|)/v_F^2)}, \tag{4.40}$$

where the upper bound of sum in the exponent of Eq.(4.38), $M_{up}=2$ is taken in the second equality. The indices n and m run over the lattice positions between $n=2$ to $n=N-1$. The bilinear summation over impurity strengths is particularly useful for analytic disorder averaging if the α_i are given by a Gaussian distribution:

$$\overline{T} = \int T(\{\alpha\}) \prod_{i=2}^{N-1} \frac{e^{-\alpha_i^2/2\sigma^2}}{\sqrt{2\pi}\sigma} d\alpha_i \tag{4.41}$$

$$= \frac{1}{\sqrt{det(K)}} \tag{4.42}$$

where the matrix K is:

$$(K)_{nm} = \delta_{nm} + 2\sigma^2 cos(2ka|n-m|)/v_F^2. \tag{4.43}$$

K can also be written in the form

$$K = I_{N-2} + \frac{2\sigma^2}{v_F^2}(|v\rangle\langle v| + |v^*\rangle\langle v^*|), \tag{4.44}$$

where $|v\rangle$ is a vector with elements $(v)_n = e^{inka}$ with the index $n = 1, \cdots, N-2$. This form shows that K is a rank 2 matrix, and the determinant of K is as easy as taking a

determinant of a 2×2 matrix. As a result:

$$det(K) = \left[1 - (N-2)\frac{\sigma^2}{v_F^2}\right]^2 - \frac{\sigma^4}{v_F^4}|\Sigma_{n=1}^{N-2} e^{inka}|^2. \tag{4.45}$$

In the weak disorder regime, the first term gives the dominant contribution to the transmission coefficient. Fig.4.4 shows a surprisingly good agreement between numerics that take into account all orders and the analytics within 2nd order for different system size N. The perturbation theory works only when the expansion parameter is smaller than unity. For our case, from the expansion parameter, $Tr(O^2)$ in Eq.(4.37), the condition is

$$\lambda = \frac{\sigma^2 N}{v_F^2} < 1. \tag{4.46}$$

The horizontal axis of the plot is σ^2/v_F^2, and therefore the analytic expression is valid for $\sigma^2/v_F^2 < 1/N$. For the largest system size $N = 100$ in the plot, we can see the deviation as early as $\sigma^2/v_F^2 \simeq 0.01$, consistent with the discussion.

A natural question is how will the estimates improve if higher order terms in the matrix O are taken into account. We found that the improvement is negligibly small, as shown in Fig.4.5 which shows the comparison for the inclusion of different orders. This is an interesting point to discuss. The random variables, i.e., the strengths of the impurities, α_n, appear in the exponent of exponential function. Therefore, the average transmission coefficient is dominated by the realizations with very small impurity strengths, the contribution of other realizations is exponentially suppressed. Because at small impurity strengths the contribution of higher order terms in Eq.(4.38) are also small, we find that the leading order actually gives a good estimate of all orders. Note that for systems with a spatially correlated disorder distribution, we can simply introduce a spatially correlated Gaussian

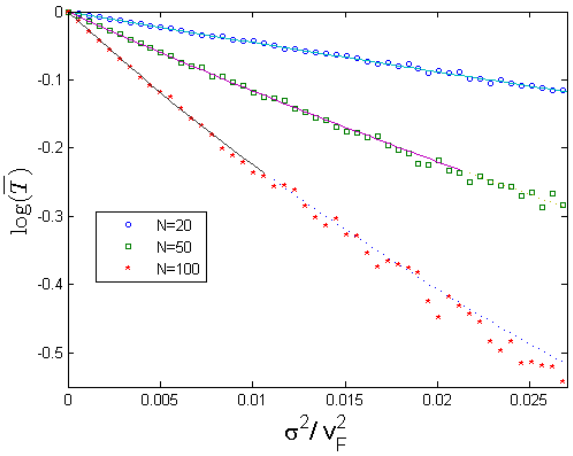

Figure 4.4: $\log \overline{T}$ of a disordered 1d wire with $ka = 0.45\pi$ is plotted. 1000 different disorder realizations are numerically performed (dots) and compared with the analytic expression within the perturbative regime (solid lines) and non-perturbative regime (dashed lines) for different system size N=20, 50, 100. The perturbative regime is determined by $\lambda = \sigma^2/v_F^2 < 1/N$ according to Eq.(4.46).

distribution in Eq.(4.41), which allows the averaging to follow along the same lines as for systems with non-correlated distributions.

4.3.3.2 Localization length: $\overline{log(T)}$

As shown in the last section, the disorder-average of the transmission is dominated by a few rare realizations with a set of very weak impurities. On the other hand, it is found that the log of the transmission is statistically well behaved [129, 133, 134, 135, 136]. In the weak disorder limit, the explicit expression of the inverse localization length was found using a perturbative approach to first orderin disorder [136, 137, 138]. In this section, we present the expression of $\overline{\log T}$, which includes all terms linearly proportional to system size for $W/v_F < 1$. We also obtain the terms which are not linearly proportional to system size in the appendix. They may have a non-trivial effect on the inverse localization when the electron's wavelength is commensurate with the lattice spacing [136]. We show, using our formalism, why $(\log T)/L$ obeys the central limit theorem. Also, we discuss the behavior of

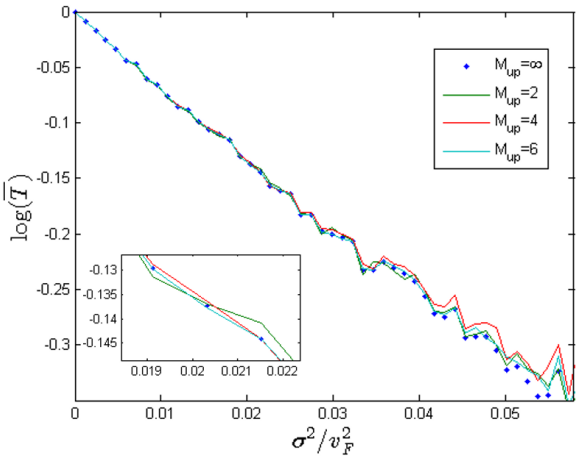

Figure 4.5: $\log \overline{T}$ with $ka = 0.45\pi$ is numerically computed (lines) considering different upper bound M_{up} of summation in the exponent of Eq.(4.38), and compared with exact numerical results (dots) for a system of $N = 30$. The improvement by including the higher order correction is slight.

$\overline{\log T}$ in the strong disorder limit.

Let us first consider the disorder strength within perturbation regime, $W/v_F < 1$, where the W is the cutoff of uniform disorder distribution. Here we employ the uniform distribution instead of a Gaussian distribution, ensuring all moments are bounded. Working in the perturbation regime validates the expansion of $log(I+O)$ for the terms linearly proportional to system size considered below. We consider the terms with even order of O in the expansion, since they are the only non-vanishing terms after disorder averaging. The term with even m^{th} order of O is:

$$\frac{1}{m} Tr\left[O^m + O^{*m}\right] = \tag{4.47}$$

$$\frac{2}{m} \sum_{n_1,\cdots,n_m} \left(\prod_{i=1}^{m} \frac{\alpha_{n_i}}{v_F}\right) cos\left(ka \sum_{i=1}^{m} |n_{i+1} - n_i|\right) \tag{4.48}$$

where $n_i = 2, \cdots, N-1$ is index of impurity site, and $n_{m+1} \equiv n_1$. Though the exact summation over indices seems tricky, we find the dominant contribution by summing terms

with zero argument of the cosine function: $n_{i+1} = n_i$ for all i. Retaining such terms, we find that the average of the log transmission is given by:

$$\begin{aligned}
\overline{log(T)} &\simeq -\frac{L}{a}\sum_{m=1}^{\infty}\int_{-W}^{W}(-1)^{m+1}\frac{1}{m}\left(\frac{\alpha}{v_F}\right)^{2m}\frac{d\alpha}{2W} \\
&= -\frac{L}{a}\sum_{m=1}^{\infty}\frac{(-1)^{m+1}}{m(2m+1)}\left(\frac{W}{v_F}\right)^{2m} \qquad (4.49) \\
&= -L/l_{loc}. \qquad (4.50)
\end{aligned}$$

where $L = (N-2)a$ is the length of disordered regime in the wire. The next dominant correction with non-zero argument of the cosine function is discussed in the appendix. Such rotating terms could be important for the wavelength commensurate with lattice spacing, otherwise the sum of rotating terms will average out to zero in general. The localization length of system is found as:

$$l_{loc}/a = \left[Log\left(1+\frac{W^2}{v_F^2}\right) - \frac{v_F}{iW}log\left(\frac{1+iW/v_F}{1-iW/v_F}\right) - 2\right]^{-1}, \qquad (4.51)$$

which is plotted in Fig.4.6 compared with computational results that take into account all non-zero arguments of cosine function, showing reasonably good matching for different system sizes. The very first term of the inverse localization length $a/l_{loc} \simeq W^2/3v_F^2$ and this is consistent with previous findings using perturbation approaches [137, 136].

It is worthwhile to compute the variance of the inverse localization length, in order to check if $(\log T)/L$ is really statistically well behaved. Numerically [133], and analytically [136], it was found that the variance is proportional to the inverse square root of system size. The first leading contribution for the variance comes from the $m = 1$ term, Eq.(4.48), and the computation is directly following:

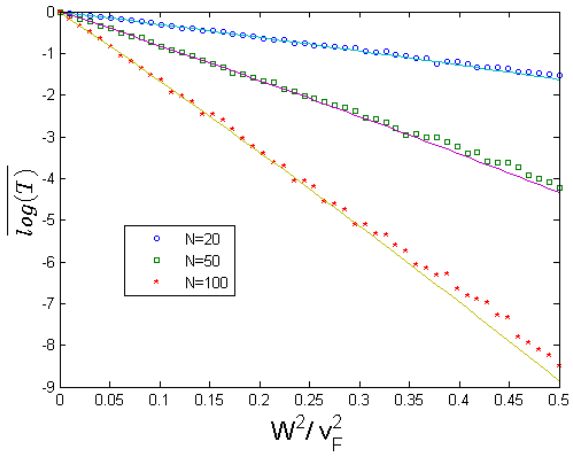

Figure 4.6: $\overline{log(T)}$ for different system sizes, N=20, 50, 100 with $ka = 0.25\pi$ using uniform distribution $[-W, W]$ is numerically computed (dots) and compared with the analytic results (lines), Eq.(4.50). Despite ignoring multiple scatterings from different impurities, as a leading order approximation the analytic result works well beyond its pertrubative regime $W^2/v_F^2 < 1/N$. The disorder averaging with 1000 realizations is performed.

$$\overline{\left(\frac{logT}{L}\right)^2} = \overline{\left(\frac{2}{L}\sum_{i=2}^{N-1}\frac{\alpha_i}{v_F}\right)^2} + O\left(\frac{W^4}{L}\right) \tag{4.52}$$

$$= \frac{4}{L}\frac{a}{l_{loc}} + O\left(\frac{W^4}{L}\right). \tag{4.53}$$

where $a/l_{loc} = W^2/3v_F^2$ up to the order of W^2. Therefore, we obtain the previously known relation[136, 133]:

$$\frac{var\left(l_{loc}^{-1}\right)}{l_{loc}^{-1}} = \frac{4}{L/a} + O\left(\frac{W^4}{L}\right) \tag{4.54}$$

confirming that the $\log T/L$ a variable following the central limit theorem.

Let us end this section with the disorder averaging of opposite limit. For 'strong' disorder strength, we take v_F/W as a perturbation expansion parameter. We are careful to use the

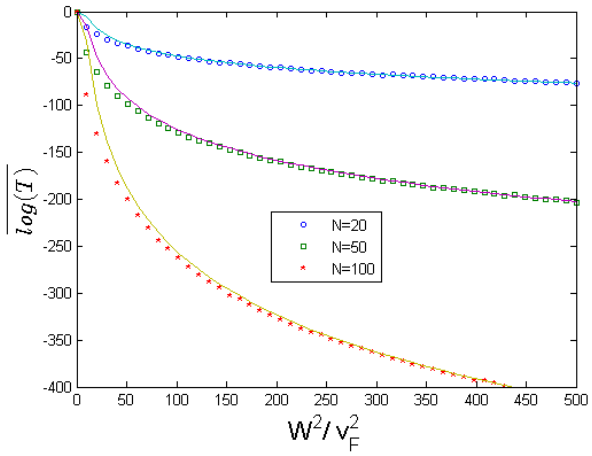

Figure 4.7: $\overline{log(T)}$ in strong disorder strength limit with $ka = 0.25\pi$ is numerically computed (dots) and compared with analytic approximation (lines) according to Eq.(4.57). They match well in the strong disorder regime, while in the weak disorder regime a deviation is present since the perturbation parameter is now $\lambda = v_F^2/W^2$, and the range of impurity strength is $[-W, W]$ instead of $[-1/W, 1/W]$. The disorder averaging with 1000 realizations is performed.

term 'strong', since our expression based on the picture of two chiral modes would not be valid as the energy scale brought by impurities is comparable or larger than energy band width of a clean wire. For more discussion of 'strong' disorder limit, we refer to section III.A. Having the elements of matrix $1\alpha G$ large, the transmission is:

$$T = \left|\frac{1}{det[I+\alpha G]}\right|^2 \simeq \left|\frac{1}{det[\alpha G]}\right|^2 \tag{4.55}$$

$$log(T) = C + \sum_{i=2}^{N-1} log\left(\frac{v_F^2}{\alpha_i^2}\right) \tag{4.56}$$

where $C = -2log|det[v_F G]|$. Therefore, the average of the log T in the uniform distribution of disorder is straightforward:

$$\overline{log(T)} \simeq C - 2(N-2)\left[log\left(\frac{W}{v_F}\right) - 1\right], \tag{4.57}$$

which is plotted in the Fig.4.7 for different system size and shows a good agreement. This is also consistent with a previous study by Stone et al.[136] in the strong disorder limit. It is also interesting to compare this strong disorder limit expression to the weak disorder one that the second term of Eq.(4.57) is obtained from Eq.(4.51) in $W/v_F \gg 1$ limt.

4.3.3.3 Resistance: $\overline{R} = \overline{1/T}$

There have been many studies of the resistance of disordered 1d wires [128, 129, 130, 131, 132]. Like the transmission, which was discussed earlier, the resistance is not a statistically well behaved quantity since its fluctuations increase faster than its average with system size. Nevertheless, various approaches have been used to compute the moments of the resistance [134, 130, 131, 142], and the scaling behavior of resistance with system size attracted lots of attention [133, 129, 131]. Our formalism does not offer significant advantages for computing the disorder average of the resistance; nonetheless, we carry out the calculation for the sake of completeness of the formulation developed in this manuscript.

The resistance of 1d wire is proportional to the inverse transmission 1/T. Thus, let us focus on the disorder averaging of 1/T for simplicity. Directly from Eq.(4.35) the inverse transmission can be expressed by the determinant of the matrices:

$$1/T = \frac{1}{\mathcal{G}_{N1}\mathcal{G}^*_{N1}} \tag{4.58}$$

$$= \frac{det[G^{-1}G^{*-1} - \alpha G^{*-1} - G^{-1}\alpha + \alpha\alpha]}{det[G^{-1}G^{*-1}]}, \tag{4.59}$$

with $G^{-1} = 1/(G_R + G_L)$, which is the Hamiltonian of clean 1d wire and therefore a tridiagonal matrix. Hence, the matrix inside the determinant in the numerator in Eq.(4.59) is essentially an extended version of a tridiagonal matrix which has five non-zero elements along the diagonal element instead of three as in Eq.(4.35), with the elements:

$$D_{n,n} = (\alpha_n - E)^2 + 2t^2 \tag{4.60}$$

$$D_{n+1,n} = D_{n,n+1} = t(\alpha_n + \alpha_{n+1}) - 2tE \tag{4.61}$$

$$D_{n+2,n} = D_{n,n+2} = t^2. \tag{4.62}$$

Here $D_{1,1} = D_{N,N} = 2t^2$, $\alpha_1 = \alpha_N = te^{-ika}$, and we place impurities at $i = 6, 10, 14, \cdots, N-5$ so that transfer matrices are not impurity correlated. As a result, the recursion relation involving a transfer matrix can be written using six elements:

$$\begin{pmatrix} d_{4(m+1)+1} \\ d_{4(m+1)+2} \\ d_{4(m+1)+3} \\ d_{4(m+1)+4} \\ X_{4(m+1)+2} \\ X_{4(m+1)+3} \end{pmatrix} = T^m_{6\times 6} \begin{pmatrix} d_{4m+1} \\ d_{4m+2} \\ d_{4m+3} \\ d_{4m+4} \\ X_{4m+2} \\ X_{4m+3} \end{pmatrix}$$

where d_{4m+j} is the determinant of the upper left square matrix of D up to the $(4m+1)^{th}$ row and column. X_n are also the determinants of a similar matrix which is required to construct the transfer matrix (see Fig.4.8):

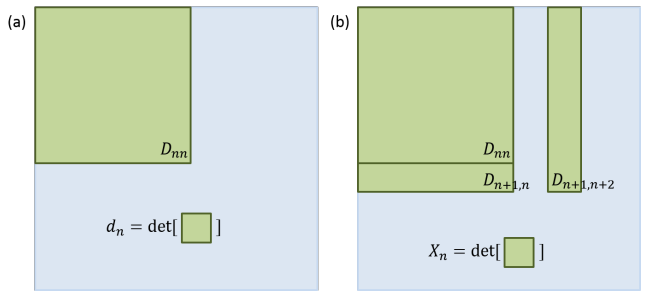

Figure 4.8: Describing the elements of the determinant in Eq.(4.63). (a) d_n is the determinant of Green's square block up to element D_{nn}. (b) X_n is the determinant of the Green's blocks collection.

$$X_n = D_{n,n+1}d_{n-1} - D_{n-1,n+1}D_{n,n-1}d_{n-2} \tag{4.63}$$

$$-D_{n-1,n+1}D_{n-2,n}X_{n-2} \tag{4.64}$$

From this recursion relation one can build the train of transfer matrices and perform disorder averaging for each transfer matrix separately.

To have an analytic description, we look for the exponents of the $1/T$, which are related to the eigenvalues of the transfer matrix. The characteristic equation of the disorder averaged transfer matrix $T^m_{6\times 6}$ has one trivial eigenvalue, unity, and the others are from a quintic equation whose general solution is not analytically available. Here we show the computation of "analytic" and numeric results in Fig.4.9. The plot shows the exponential increase of the resistance of disordered wire with the system size.

4.4 Example: Quantum Hall fluid

Another natural application for the det-formula is the quantum Hall system. The application of the det-formula is rather straightforward as it contains an explicit chiral model

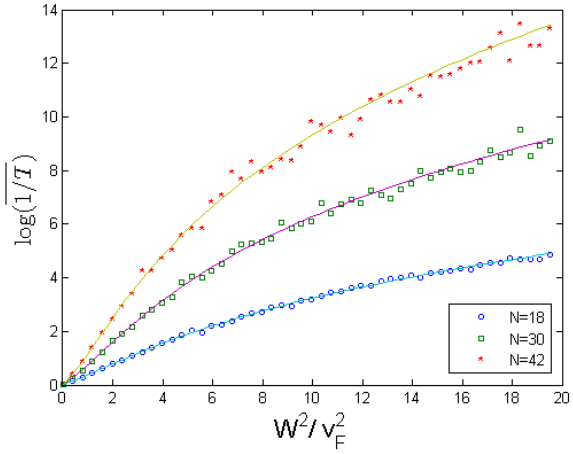

Figure 4.9: $\log \overline{1/T}$ for different system sizes, N=18, 30, and 42 with $ka = 0.45\pi$ is computed numerically (dots) by disorder averaging of 2000 realization. And, the analytic disorder averaging (lines) is performed exactly using transfer matrix, though its eigenvalues cannot be expressed in a closed form.

along the boundary. Consider the system described in Fig.4.10, where impurities near the boundary may scatter the chiral mode, and impurities are also connected with each other in a random fashion. In the single particle picture, the conductance of the chiral mode is expected to be quantize; however, the Green's function will possess a system specific phase factor due to the scattering from the impurities. These non-trivial phase factors in quantum Hall systems can be probed by different types of interferometers [143, 144, 145, 146, 147]. Our purpose in this section is to estimate the accumulated phase throughout the system.

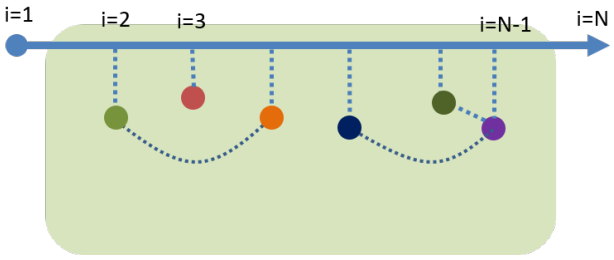

Figure 4.10: A chiral mode in a quantum Hall system with an insulating bulk. Multiple impurities with random couplings near the edge are encountered by the chiral mode, and the accumulated phase is estimated with the det-formula.

Let us introduce the Green's function, G_B, of quantum dots with random coupling, the coupling matrix T between chiral mode and quantum dots, and $\mathcal{T} = \hat{U}_{st}V/2v_F$, as is done in section 4.2. The direct application of the det-formula gives:

$$\mathcal{G}_{N1} = \frac{e^{i(N-1)ka}}{iv_F}\frac{det[I - G_{L0}^{-1}\mathcal{T}G_B\mathcal{T}^\dagger]}{det[I + \mathcal{T}G_B\mathcal{T}^\dagger G_{R0}^{-1}]} \tag{4.65}$$

$$= \frac{e^{i(N-1)ka}}{iv_F}\frac{e^{TrLog[I-G_{L0}^{-1}\mathcal{T}G_B\mathcal{T}^\dagger]}}{e^{TrLog[I-(G_{L0}^{-1}\mathcal{T}G_B^\dagger\mathcal{T}^\dagger)^\dagger]}}, \tag{4.66}$$

where in the first equality the order of matrix multiplication is changed within the determinant of denominator, then in the second equality $(G_{R0}^{-1})^\dagger = -G_{L0}^{-1}$ is used. Having a symmetric form, diagonalization helps to further simplify:

$$G_{L0}^{-1}\mathcal{T}G_B\mathcal{T}^\dagger = U^{-1}\Lambda U \tag{4.67}$$

The bulk Green's function G_B may, in general, not be a hermitian matrix in an open, lossy system. However, when the bulk states are insulating and do not contain propagating states to the exterior, the bulk Green's function becomes real and symmetric, $G_B^\dagger = G_B$. As a result, the renormalized Green's function is now reduced to:

$$\mathcal{G}_{N1} = \frac{e^{i(N-1)ka}}{iv_F}e^{\sum_n Log\left[\frac{1-\lambda_n}{1-\lambda_n^*}\right]} \tag{4.68}$$

which gives a succinct expression for the accumulated phase due to random impurity scatterings in terms of the eigenvalues of the matrix Eq.(4.67). We expect this expression to be useful in similar systems.

4.5 Conclusion and summary

In this manuscript we introduced a closed form expression for the propagator of a chiral mode coupled to a bulk. For a given bulk Green's function and coupling matrix to the chiral mode, we were able to express the renormalized chiral Green's function by the ratio of determinants. No assumption is made on the bulk Green's function, therefore, the formula is applicable to a system with and without non-localized bulk modes.

Using a disordered 1d quantum wire as example, we demonstrated how non-chiral 1d systems can be modeled in terms of chiral modes, and computed the average transmission coefficient, its inverse, and log. The det-formula was shown to be especially powerful in performing disorder averaging for different transport quantities. A similar trick is expected to work for quasi 1d and topological metal systems.

As a second example, the phase accumulated by the chiral mode is conveniently estimated in a quantum hall system with random impurities. This formula may be used to describe the interference pattern in quantum hall interferometers as a function of chemical potential of the bulk and other system characteristics.

4.6 Appendix: Localization length of the next order

Localization length was computed by averaging the log of transmission coefficient for different disorder realizations. We computed the main contribution in Eq.(4.50) after ignoring the rotating terms. Up to the second order in disorder strength, the analytics and numerical results are in good agreement(Fig.4.6) in weak disorder regime. However, as soon as the fourth and higher orders get important at moderate disorder strength, the contribution from the rotating term should be taken into account. In this appendix we compute the

leading correction of the rotating term by allowing the indices n_i to be different.

In section 4.3.3.2, we obtained the leading order of disorder averaged $\log(T)$, assuming all indices in Eq.(4.48) are the same: $n_1 = n_2 = \cdots = n_m$. For the next leading correction, we allow the indices to be two different indices: $n_1, \cdots, n_m \in n_i, n_j$ with $i \neq j$. Then all possible terms of order m can be expressed by the help of a 2×2 transfer matrix form for even m :

$$\begin{aligned} &\textstyle\sum_{n_1,\cdots,n_m} \left(\prod_{i=1}^{m} \frac{\alpha_{n_i}}{v_F}\right) \mathrm{Re}[e^{ika\sum_{i=1}^{m}|n_{i+1}-n_i|}], \\ &= \textstyle\sum_{n_1,n_2} \mathrm{Re\ Tr} \left[\begin{pmatrix} \alpha_{n_1} & \alpha_{n_1} e^{ik\Delta} \\ \alpha_{n_2} e^{-ik\Delta} & \alpha_{n_2} \end{pmatrix}^m - \begin{pmatrix} \alpha_{n_1}^m & 0 \\ 0 & \alpha_{n_2}^m \end{pmatrix} \right], \end{aligned}$$

where $\Delta = |n_1 - n_2|a$ is the distance between two impurity sites. Now the problem is reduced to finding eigenvalue of the transfer matrix:

$$\lambda_{\pm} = \frac{\alpha_{n_1} + \alpha_{n_2}}{2} \pm \sqrt{\frac{(\alpha_{n_1} - \alpha_{n_2})^2}{4} + \alpha_{n_1}\alpha_{n_2} e^{2ik\Delta}} \tag{4.69}$$

By using the prefactor in Eq.(4.48) and inserting the eigenvalues:

$$\begin{aligned} \log(T_{(m)}) &= \sum_{n_1,n_2} \frac{(-1)^m}{m v_F^m} 2Re[\lambda_+^m + \lambda_-^m - \alpha_{n_1}^m - \alpha_{n_2}^m] \\ &= 2Re \sum_{n_1,n_2} log \left[\frac{(1 + \frac{\lambda_+}{v_F})(1 + \frac{\lambda_-}{v_F})}{(1 + \frac{\alpha_{n_1}}{v_F})(1 + \frac{\alpha_{n_2}}{v_F})} \right] \\ &= 2Re \sum_{n_1,n_2} log \left[1 - \frac{\alpha_{n_1}\alpha_{n_2} e^{2ik\Delta}/v_F^2}{(1 + \frac{\alpha_{n_1}}{v_F})(1 + \frac{\alpha_{n_2}}{v_F})} \right] \end{aligned}$$

which is the generating function for the correction of two indices to all orders for a particular disorder realization. For example, the first correction appears in the fourth order with non-zero argument of cosine function. By expanding the log in series of α_i/v_F, then disorder

averaging:

$$\begin{aligned}
\overline{log(T_{(4)})} &= Re \sum_{n_1,n_2} \frac{\overline{\alpha_{n_1}^2 \alpha_{n_2}^2}(4e^{2ik\Delta} + 2e^{4ik\Delta})}{-2v_F^2} \\
&= \frac{\left\langle \alpha^2 \right\rangle^2}{-v_F^4} \sum_{\Delta/a=1}^{L/a-1} \frac{L-\Delta}{a}[2cos(2k\Delta) + cos(4k\Delta)] \\
&= \frac{\left\langle \alpha^2 \right\rangle^2}{v_F^4} \left[\frac{3L}{2a} - \frac{sin^2(kL)}{sin^2(ka)} - \frac{sin^2(2kL)}{2sin^2(2ka)}\right] \qquad (4.70)
\end{aligned}$$

where $L = (N-2)a$ is the length of disordered regime. One can see that the term in the square bracket may not be small depending on the wavenumber k, but the term goes to zero upon the integration over k. This is the case for all higher order corrections. By carefully performing the expansion of the generating function, the general expression for m^{th} order correction of two indices can be deduced:

$$\begin{aligned}
\overline{log(T_{(m)})} = \frac{1}{m} \sum_{n=2,even}^{m-2} \sum_{l=1}^{l_{up}} \frac{1}{n+1} \frac{(-1)^{m/2+1}}{m-n+1} \left(\frac{W}{v_F}\right)^m \\
\times \binom{m-n}{l} \binom{n}{l} l \left(\frac{1}{n} + \frac{1}{m-n}\right) \left[\frac{L}{a} - \frac{sin^2(kLl)}{sin^2(kal)}\right] \qquad (4.71)
\end{aligned}$$

where $l_{up} = min(n, m-n)$ and indices m and n are even integers. Fig.4.11 shows the contribution of $\overline{log(T_{(m)})}$ in addition to the leading order with single index (Eq.(4.50), solid line). The dots are from the numerical result averaged over 4000 disorder realizations. The difference between dotted lines and the solid line are corrections made by double index terms for different wave numbers. $\overline{\log T}$ is independent of wave number in weak disorder limit and they converge to a single line(Eq.(4.50)).

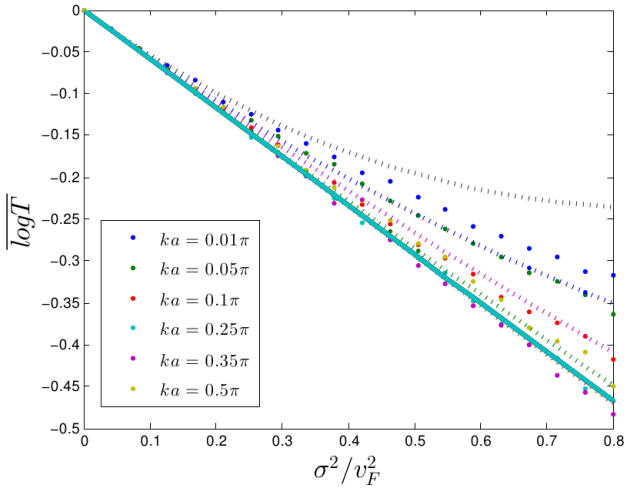

Figure 4.11: Disorder averaged log T is plotted using the exact expression (dots) from Eq.(4.35), the single index contribution (solid line) from Eq.(4.50), and the result which includes the double-index correction (dotted line) from Eq.(4.71). At moderate disorder the single-index contribution fails to reproduce the exact results for the various wave numbers. The double-index correction, however, does manage to account for wave-number dependence except for the smallest wave number.

Chapter 5

Effects of surface impurity potentials on surface states in topological insulators

5.1 Background and introduction

A study of systems with a disorder potential is a tricky subject in analytic manners, even for a single particle Hamiltonian. A perturbative approach provides solutions at weak or strong disorder strength limits, but we often want to know the transition electronic behavior solutions between weak and strong disorder strengths. Furthermore, naive applications of perturbation approach can lead to an incorrect interpretation. In this chapter, we present a non-perturbative approach to the local density of surface states in the presence of disorders on a system surface in any dimensions.

In relation to the surface states and impurities in a 3d topological insulator, Schubert and his colleagues [21] conducted an exact diagonalization study to see how the local density of states behaves as a function of surface impurity strength. In the strong impurity limit, surprisingly, they found that the system maintains clean surface states underneath the disordered top layer. At a moderate impurity strength comparable to the bandwidth of the system, the local density of states shows larger fluctuations in the first few layers and they

do not have a well-defined local density of states in momentum space, implying a diffusive metallic behavior of surface states.

In this chapter, our aim is to understand the two non-trivial behaviors of local density of states in an analytically oriented manner. We will introduce a general framework to study local density of states in section 5.2 which is applicable to any systems with layered structure. In section 5.3, a toy model of 2d topological insulator is employed to demonstrate the approach introduced earlier with a concrete example. Lastly, in section 5.4 the conductance of the same system with different magnetic and non-magnetic impurity strength are present to complement the local density of states data.

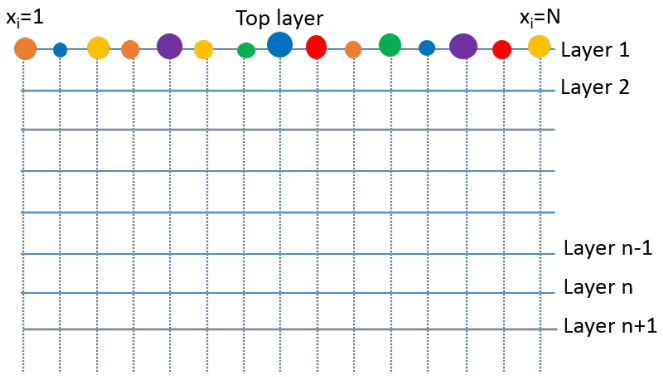

Figure 5.1: A pictorial description of 2d lattice model. Along x-direction we have a periodic boundary condition that $x_1 = x_{N+1}$, and along y-direction there are N-layers and the subscript n indicates the n_{th} layer along y-direction. Different colors and sizes of dots on the top layer indicate random on-site impurity potentials. We study how the top random surface impurities propagate down into the bulk layers.

5.2 General framework: transfer matrix of layered wave functions

Numerically, the local density of states at a certain energy within the gap is obtained by finding eigenstates of a Hamiltonian with surface impurities. One repeats the process

for different realizations of impurities, then the statistics of the local density of states is computed. In this section, we suggest a different approach: the ansatz of a wave function in the first layer will be assumed to reflect the surface impurity strength, then the transfer matrix between layered wave functions will be employed to discover an overall behavior of the local density of states. To proceed, the analytic expression of the transfer matrix is essential to offering further insight. We come up with a disorder-free transfer matrix, which is the key result of this chapter.

5.2.1 Transfer matrix from Schrodinger equation

The Schrodinger equation along the layers provides the most direct way of getting the transfer matrix between in-layer wave functions.

$$B\psi_{n-1} + [H_{||} + U\delta_{n,1} - E]\psi_n + B^{\dagger}\psi_{n+1} = 0, \tag{5.1}$$

where ψ_n is a wave function on n_{th} layer, $H_{||}$ is an in-layer Hamiltonian, U is an impurity potential on the first layer, B and $B^{\dagger}$ are hopping terms between layers, a layer index n is a positive integer, and $\psi_0 = 0$ (see Fig.5.1). For $n = 1$ case, we obtain the relation between the first and second layer wave functions:

$$\psi_2 = B^{\dagger -1}[E - H_{||} - U]\psi_1. \tag{5.2}$$

To get the relation between the second and third layer wave functions, put ψ_1 in (5.2) to (5.1) with n=2. One can repeat this process to get the relation between ψ_n and ψ_{n-1}:

$$\psi_n = V_{(n)}^{-1} B\psi_{n-1}, \tag{5.3}$$

where we introduced a n_{th} layer effective potential $V_{(n)}$:

$$V_{(n)} = B[E - H_{||} - V_{(n-1)}]^{-1}B^{\dagger}, \tag{5.4}$$

The first layer effective potential is the actual surface impurity potential, $V_{(1)} = U$. One can think of $B\psi_{n-1}$ in (5.1) as a contribution from the first to $(n-1)_{th}$ layer integrated, and therefore $V_{(n)}$ multiplied to ψ_n in (5.3) can be thought of as an effective potential on n_{th} layer from all previous layers.

Now the transfer matrix between ψ_n and ψ_1 is obtained by multiplying a series of the transfer matrices:

$$\psi_n = [V_{(n)}^{-1}B][V_{(n-1)}^{-1}B]\cdots[V_{(2)}^{-1}B]\psi_1. \tag{5.5}$$

This is the conventional formulation using the transfer matrix. Though this is exact, the actual analytic expression is impossible, since the surface impurity potential breaks translational and the recursion relation (5.4) is highly non-linear.

5.2.2 Holographic mapping of effective potentials

We can make a significant progress to simplify the transfer matrix in (5.5) by introducing a wave function like object $M_{(n)}$ on n_{th} layer and make a correspondence with $V_{(n)}$:

$$V_{(n)} = BM_{(n-1)}M_{(n)}^{-1}. \tag{5.6}$$

We assume that $M_{(n)}$ is invertible and satisfies the same Schrodinger equation along the layers:

$$BM_{(n-1)} + [H_{||} - E]M_{(n)} + B^{\dagger}M_{(n+1)} = 0. \tag{5.7}$$

One can straightforwardly verify that (5.7) and (5.4) are identical if the mapping (5.6) is made. The transfer matrix connecting the first and n_{th} layer wave function is now simplified:

$$\psi_n = M_{(n)}M_{(1)}^{-1}\psi_1. \tag{5.8}$$

This expression offers a convenient picture of how wave function behaves over the layers. The propagation is simply governed by the bulk property of clean system as $M_{(n)}$ is the solution of the Schrodinger equation without impurity potentials. However, it is still tricky to compute $M_{(n)}$ in the analytical manner, because the boundary condition involves the surface impurities:

$$U = BM_{(0)}M_{(1)}^{-1}. \tag{5.9}$$

This tells us that the surface impurities are doing nothing but setting the initial amplitudes of $M_{(0)}$, then the propagation of wave functions over the layers depends only on the clean bulk properties. This interpretation is not so obvious from (5.5).

5.2.3 Disorder-free transfer matrix

We discuss our main finding of the chapter that the transfer matrix discussed so far((5.5) and (5.8)) can be written in a disorder-free format. For a system with a finite width, we

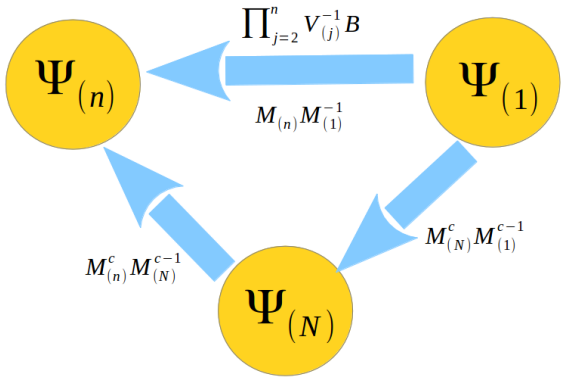

Figure 5.2: A diagram describing the transfer matrix methods as discussed in section 5.2.3. Instead of using the product of the transfer matrix, $V_{(j)}^{-1}B$, to connect ψ_1 and ψ_n, we bring the bottom wave function ψ_N in the middle to make use of the disorder-free transfer matrix, $M_{(n)}^{c} M_{(1)}^{c-1}$.

can think of the similar relation between the bottom-most layer wave function and the n_{th} layer wave function. For instance,

$$\psi_N = [E - H_{||}]^{-1} B \psi_{N-1}. \tag{5.10}$$

Alternatively, using the Schrodinger equation (5.1),

$$\psi_{n+1} = [B^{\dagger -1} \Sigma_{(n)}] \psi_n \tag{5.11}$$

where we define the effective potential on n_{th} layer due to the bottom layers:

$$\Sigma_{(n)} = B^{\dagger} [E - H_{||} - \Sigma_{(n+1)}]^{-1} B. \tag{5.12}$$

This is the recursion relation between the bottom in-layer potentials. The previously introduced mapping applies to this recursion relation similarly:

$$\Sigma_{(n)} = B^{\dagger} M^{c}_{(n+1)} M^{c-1}_{(n)}. \tag{5.13}$$

To connect ψ_1 and ψ_n, imagine the propagation from the bottom-most wave function ψ_N to ψ_1 and ψ_n. As a result,

$$\begin{aligned} \psi_n &= [B^{\dagger -1}\Sigma_{(n-1)}][B^{\dagger -1}\Sigma_{(n-2)}]\cdots[B^{\dagger -1}\Sigma_{(1)}]\psi_1 \\ &= [M^{c}_{(n)} M^{c-1}_{(1)}]\psi_1. \end{aligned} \tag{5.14}$$

where $M^{c}_{(n)}$ is disorder-free, and therefore it is diagonal in the momentum space. It is strictly determined by the clean bulk without surface impurity potentials, and finally the analytic expression of the transfer matrix is at hand. Explicit computation will be shown for 2d topological insulator system with edge impurities.

5.3 Application to 2d topological insulator

In the previous section, we introduced a general framework of how to compute a transfer matrix between in-layer wave functions. We have succeeded in expressing it in a disorder-free and analytically computable form. The formulation is applicable to any system with a layer structure. In this section, a 2d topological insulator model is employed to explicitly show how the local density of states can be estimated in a system with edge impurities.

5.3.1 Model Hamiltonian

Consider the toy model of a 2d topological insulator. In momentum space,

$$H(\vec{k}) = [m - 2b(2 - cosk_x - cosk_y)]\tau_z$$
$$+A[\tau_x s_z sink_x + \tau_y sink_y] \tag{5.15}$$

where τ_i is a pauli matrix in orbital basis, s_i a pauli matrix in spin basis. Momenta k_x and k_y are normalized by a lattice spacing a. To introduce an edge state, the open boundary condition is introduced in the y-direction, and the periodic boundary condition is applied to the x-direction. An in-layer Hamiltonian and a hopping term between layers in Eq. (5.1) are:

$$H_{||} = [m - 2b(2 - cosk_x)]\tau_z + \tau_x s_z A sink_x, \tag{5.16}$$
$$B = b\tau_z - iA\tau_y. \tag{5.17}$$

The system is in the topological phase if the inversion of band takes place for some range of momentum: $\text{sign}(mB) > 0$. For this case, the dispersion of the top and bottom edge states are $E = \pm A\text{sin}k_x$.

5.3.2 Disorder-free Transfer matrix

Using the above Hamiltonian, we can build the transfer matrix, Eq. (5.14). The computation is not hard as it is diagonal in momentum space, but there are three cases which require different derivations: i) $(k_x, E) = (0, 0)$ case, ii) $(k_x, E) = (2\pi l/N_x, \pm A\text{sin}(2\pi l/N_x))$, where l is an integer and N_x is the system size along the edge, and iii) cases neither type i) nor

ii) . For each cases, the detailed derivations of the transfer matrix expression are given in appendix 5.6. We argue that case iii) is most relevant to the local density of states of the top edge state in the presence of top edge impurities. This is because the case i) and ii) are only possible for a clean system with an infinitely long width.

The elements of transfer matrix of case iii) for a given momentum and energy (k_x, E) in the basis of $|+\rangle = (1,1)^T/\sqrt{2}$ and $|-\rangle = (1,-1)^T/\sqrt{2}$ are:

$$\langle +|S_{(1)}^{(n+1)}|+\rangle = \frac{1}{r_1 - r_3}\left[\rho_1^{-n} r_1 - \rho_3^{-n} r_3\right] \tag{5.18}$$

$$\langle +|S_{(1)}^{(n+1)}|-\rangle = \frac{r_1 r_3}{r_1 - r_3}\left[\rho_3^{-n} - \rho_1^{-n}\right] \tag{5.19}$$

$$\langle -|S_{(1)}^{(n+1)}|+\rangle = \frac{1}{r_1 - r_3}\left[\rho_1^{-n} - \rho_3^{-n}\right] \tag{5.20}$$

$$\langle -|S_{(1)}^{(n+1)}|-\rangle = \frac{1}{r_1 - r_3}\left[\rho_3^{-n} r_1 - \rho_1^{-n} r_3\right] \tag{5.21}$$

where ρ_1 and ρ_3 are eigenvalues of the Schrodinger equation (5.7) whose magnitudes are larger than unity. r_1 and r_3 are the ratio of coefficients of Schmidt decomposition of eigenvectors into $|+\rangle$ and $|-\rangle$ (see appendix). r_1 is zero if eigenvector $|\rho_1\rangle$ is parallel to $|+\rangle$, and it is infinite if they are orthogonal. Note that $\langle -|S_{(1)}^{(n+1)}|+\rangle$ could be very large among other elements when (k, E) is very close to case i) and ii). This element is indeed responsible for the flipping from $|+\rangle$ to $|-\rangle$ state, and it essentially allows the system to behave like a clean one in the strong edge impurity limit, as will be shown in the next section.

5.3.3 Simulating the local density of states

We simulate the behavior of local density of states by constructing the ansatz of the first layer wave function to reflect the impurity strength on the top edge. Then the ansatz will be propagated down to layers into the bulk using the disorder-free transfer matrix obtained in

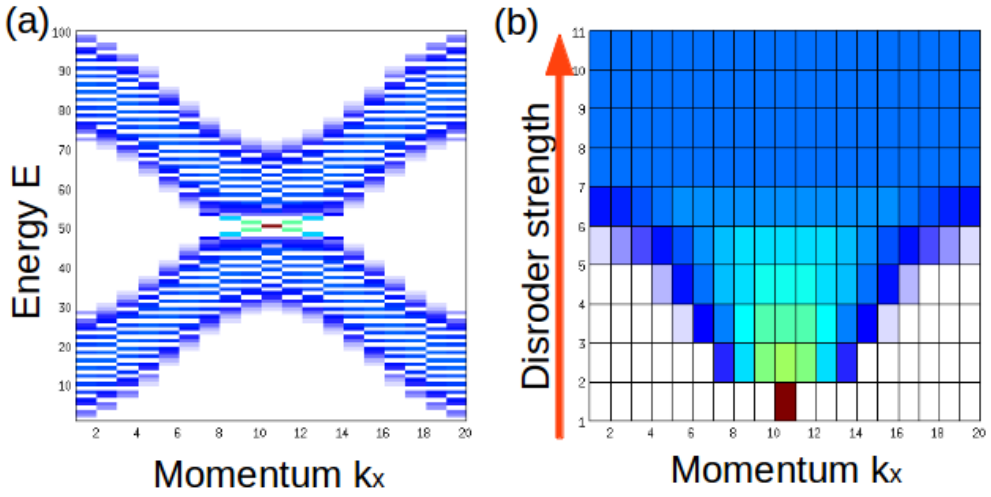

Figure 5.3: (a) A band structure of the 2d topological insulator from which we can deduce the local density of state in momentum space within the energy window $[-W/2, W/2]$. (b) $f(k_x, W)$ is plotted for disorder strength $W = 0.01, 1, 3, 5, 7, 10, 14, 20, 50, 100$. The first layer wave function ansatz Eq.(5.22) has a single non-zero value in momentum space in the clean limit, while more momentum states are accessible with increasing impurity strength.

the previous section. Lastly, the whole wave function will be normalized to unity. Without exactly solving the Schrodinger equation with edge impurities, we show the same generic behaviors of the local density of states: i) returning to the clean edge state in the strong disorder limit, and ii) a large fluctuation of the local density of states for the first few layers at moderate impurity strength.

The choice of the first layer wave function ansatz can be arbitrary, but we try to build a reasonable and minimal ansatz so that it reflects the strength of edge impurities. Our choice is:

$$\psi_1(k_x, W) = f(k_x, W) \left[\frac{1}{\sqrt{2}} \begin{pmatrix} 1 \\ 1 \end{pmatrix} + \frac{r(W)}{\sqrt{2}} \begin{pmatrix} 1 \\ -1 \end{pmatrix} \right]. \tag{5.22}$$

where a function $f(k_x, W)$ measures the spread of wave function in momentum space with impurity strength W. In the clean limit near zero energy, the wave function will be concen-

trated at $k_x = 0$, therefore $f(k_x) = \delta_{k_x,0}$. As we turn on the impurity strength, more states at different momenta will be accessible. Fig.5.3 (a) shows the actual distribution (y-axis) of the first layer wave function in the momentum space as a function of impurity strength (x-axis). The accessible momentum state as a function of impurity strength can be guessed from the band structure of the clean system, as impurities allow the state near Fermi energy to scatter into the eigenstates within the energy range $[E_F - W/2, E_F + W/2]$. This is why in Fig.5.3 (a) we can see that all momentum states are accessed with relatively uniform distribution when impurity strength can cover the whole band, $W = 14$. We will use this distribution for $f(k_x, W)$ in our ansatz (5.22).

The second part of the ansatz is its spin-orbital parts. In clean limit, the orbital is parallel to $|+\rangle$, while with increasing disorder strength the orbital begins to pick up its orthogonal parts. In (5.22), a parameter $r(W)$ is used to reflect this behavior. The orbital part of ansatz is also dependent of the momentum k_x, but we do not include such details, since only on-shell electrons are important to consider for the qualitative change of the local density of states with impurities.

Using this ansats, the local density of state in momentum space (y-axis) along the layers (x-axis) is simulated in Fig.5.4. Though our model includes certain arbitrariness, the general behavior of local density of state is robust. First, at strong impurity strength all momentum states are equally accessible in the first layer, while the $k_x = 0$ state singly stands out in the second layer when the wave function is at near zero energy (see Fig.5.4 (d)). As a result, the wave function behaves like a clean edge state with one layer shifted downward. This phenomenon always occurs as long as the portion of $|-\rangle$, mixed in the first layer wave function increases with the impurity strength. $|-\rangle$ in the first layer is flipped into $|+\rangle$ in the second layer with a large amplitude according to (5.20). For smaller values

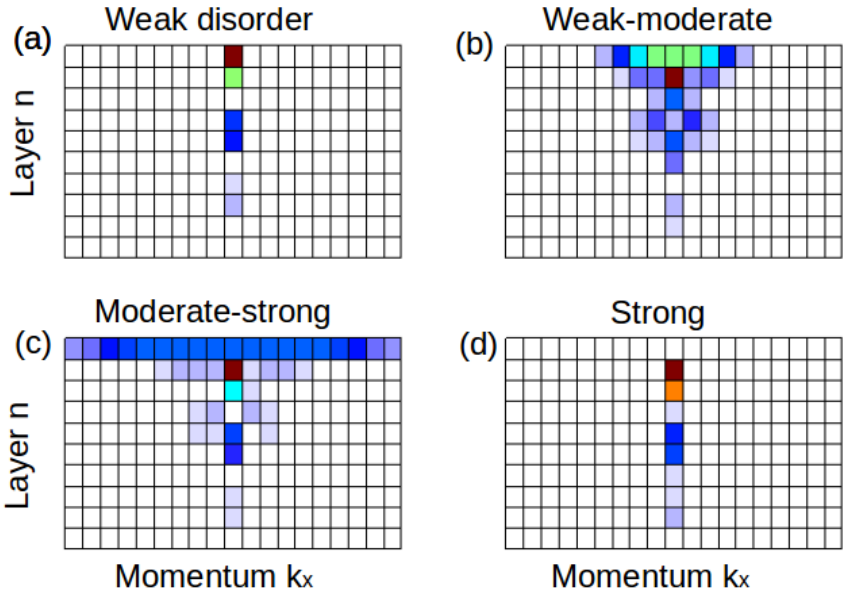

Figure 5.4: Local density of states in momentum space k_x over layers into the bulk at different edge impurity strength are obtained from the simulated first layer wave function according to (5.22). At weak (a) and strong (d) disorder, the wave functions in momentum space are well localized at $k_x = 0$, indicating that a system with strongly disordered edge impurities has edge modes of a clean system. Systems with the moderate strength, (b) and (c), of edge impurity show the transition between two limits: the LDOS is distributed in a broader range of momentum and shows a large fluctuation for different $r(W)$ (see also Fig.5.5).

of r, local density of states at moderate impurity strength are simulated in Fig.5.4 (b) and (c) with $r = 0.005$ and $r = 0.05$, respectively. We can see that the first layer wave function is fairly disordered as it has nonzero elements for a wide range of momentum, and the wave function shows the longest tail at $k_x = 0$. This implies that the n_{th} layer wave function away from the top edge impurities behaves more like the eigenstates in clean system at zero energy. Because the moderate impurity strength is between the clean and strong impurity limit, its local density of states shows a larger fluctuation for the first few layers. Fig.5.5 shows the local density of states over the layers and integrated in momentum.

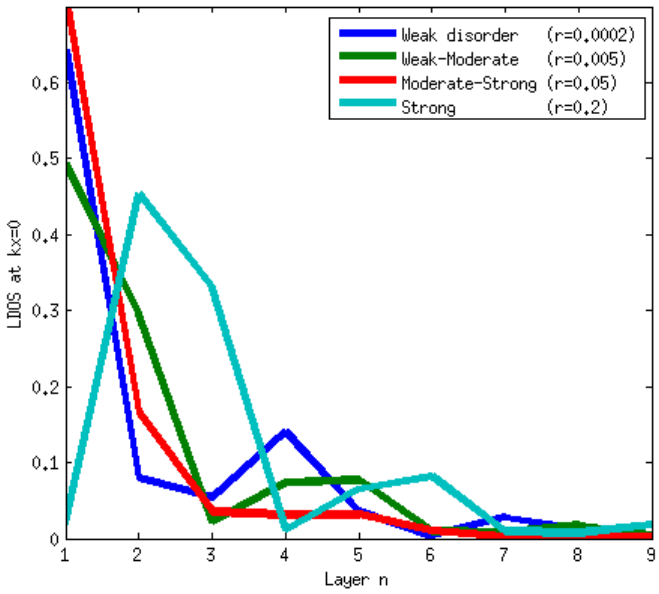

Figure 5.5: Simulated local density of states over the layers is shown for different impurity strength repsented by $f(k_x, W)$ and $r(W)$. For four impurity strengths, $W = 0.01, 3, 10, 100$, corresponding $f(k_x, W)$ in Eq. (5.22) is employed from Fig. 5.3 and an increasing proportion of $|-\rangle$ in the first layer wave function $r(W) = 0.002, 0.005, 0.05, 0.2$ are used. This plot is a momentum-integrated version of Fig.5.4.

5.4 Transport behavior

The local density of state discussed in the last section can be probed by the angle-resolved photoemission spectroscopy [37],but, the transport along the edge states is another set of information independent from the local density of states. For instance, non-magnetic impurities cannot backscatter the edge mode and its conductance remains quantized to the value of clean system, though its local density of state still shows the similar transition discussed in the previous sections. To clarify the transport nature of the system with magnetic and non-magnetic impurities along the edge, in this section we study conductance of the systems using the Landauer-Buttiker method.

Imagine a system where two semi-infinite leads are connected to a disordered region at both ends. Landauer and Buttiker [100, 101, 102] made a relation between the conductance

and the transmission coefficient through the disordered region: $g = \frac{e^2}{h} T_{N1}$, where g is conductance, T_{N1} is a transmission coefficient through the disordered region from site 1 to site N. By appealing to the linear response theorem, Fisher and Lee [103] expressed the transmission coefficient in terms of Green's functions:

$$g = \frac{e^2}{h} \mathrm{Tr}\left[\Gamma_L G_{N1} \Gamma_R G_{N1}^{\dagger}\right] \tag{5.23}$$

where $\Gamma_L = i(\Sigma_L - \Sigma_L^{\dagger})$, G_{N1} is a Green's function from site 1 to N renormalized by the presence of the leads, and Σ_L is a self-energy of the semi-finite left lead. Each term is computed recursively so that the conductance of a long system can be obtained with a reasonable computing power. A good review of the detailed calculation can be found elsewhere [148].

5.4.1 Non-magnetic impurity case

Consider the 2d topological insulator system introduced earlier with non-magnetic impurities along the top edge. Because the Hamiltonian is diagonal in spin basis without magnetic impurities, we can consider one spin section only for its transport behavior. Imagine an incoming electron from the left lead following top edge. If the chemical potential is located within the energy gap, the backscattering is improbable since the electron needs to scatter into the bottom edge mode. Therefore, we naturally expect an almost quantized value of conductance within the energy gap. This is shown in Fig.5.6 at different impurity strength W.

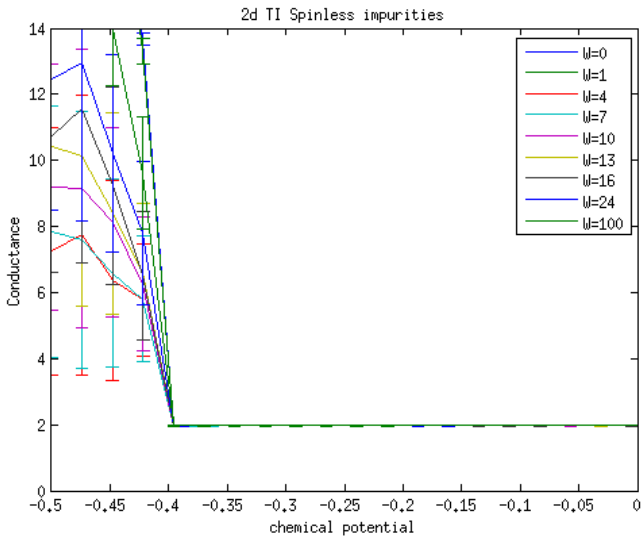

Figure 5.6: Conductance near zero energy for different magnetic impurity strengths. For all strengths, the conductance is well quantized within the energy gap since backscattering is not allowed.

5.4.2 Magnetic impurity case

Two chiral edge modes with opposite spins are coupled as soon as magnetic impurities are introduced. As a result, the transport through the disordered edge is suppressed, while the transport through the other clean edge remains unaffected. Therefore, the total conductance rapidly approaches to e^2/h with the increasing magnetic impurity strength. However, in the strong impurity limit, $W > 500$, we found that the conductance comes back up to its clean system value. This is because such impurities are strongly bound to electrons at energies far away from the Fermi energy, and they play negligible roles in the transport at the Fermi energy. Fig.5.7a shows the conductance behavior with chemical potentials for different impurity strength, and we can see how the conductance changes within the energy gap between one and two units of e^2/h conductance. The behavior is clearer in Fig.5.7b, which shows the conductance with the strength of impurities in the log-scale for different chemical potentials. We can see in the intermediate range of impurity strength,

the conduction through the disordered top edge is significantly suppressed due to magnetic impurities, while the conductance comes back up to two units of e^2/h value in the strong impurity limit.

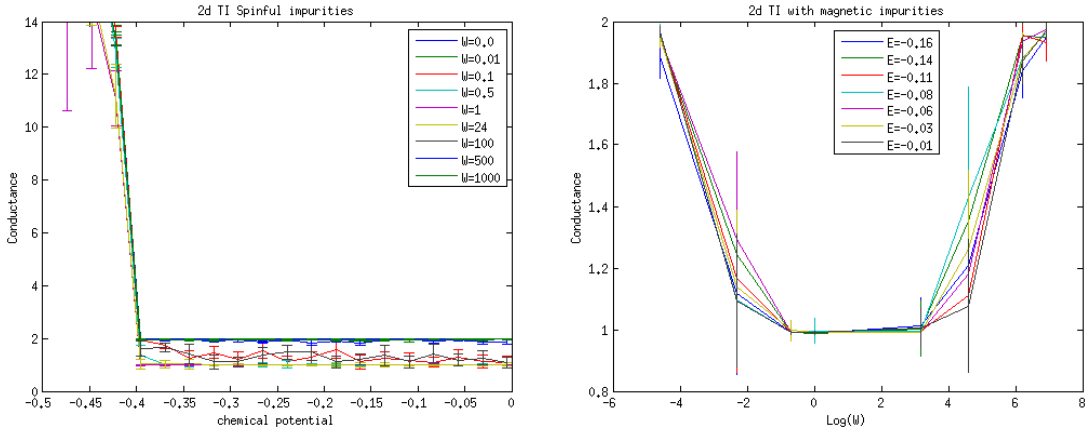

(a) (b)

Figure 5.7: (a) A similar conductance plot is shown for magnetic impurities. In the weak and strong impurity limit the conductance is close to two units of e^2/h, while at moderate strength case one edge channel is completely suppressed and the conductance is reduced to one unit of e^2/h. (b) Conductance is plotted in the log-scale of impurity strength (x-axis) for different chemical potentials. One can see the change of conductance with magnetic impurity strength more clearly for different chemical potential.

5.5 Conclusion and Summary

We have developed a framework to study surface impurity of a system with a layered structure. Using a mapping of effective potentials in terms of a wave function like object $M_{(n)}$, we are able to express the transfer matrix from a disordered first layer wave function to n_{th} layer wave function. In this way, the general behavior of the local density of state over the layers at different impurity strength is studied and it shows the consistent picture with the result from the exact diagonalization approach by Schubert et al. [21]. Furthermore, we complement the conductance calculation using the Landauer-Buttiker formulation that

helps to identify the difference between magnetic and non-magnetic impurity cases.

5.6 Appendix: the derivation of transfer matrix

In this appendix, we show explicitly how to build the wave function like object M-matrix in a clean system satisfying the boundary condition. We divide the problem into three cases: i) (k, E) is not on the dispersion, ii) (k, E) is on the dispersion at nonzero energy, and iii) (k, E) is on the dispersion at zero energy. We solve the following Schrodinger equation:

$$B\frac{1}{\rho}\psi_n + [H_{||}(k_x) - E]\psi_n + B^\dagger\rho\psi_n = 0, \tag{5.24}$$

where we put $\psi_{n-1} = \frac{1}{\rho}\psi_n$ and $\psi_{n+1} = \rho\psi_n$. We will solve this Schrodinger equation for a specific momentum and energy, and in this way we keep our approach analytically tractable.

5.6.1 Case (iii): $(k, E) \neq (k_x, \pm A\mathbf{sin}(k_x a))$

We want to build an invertible 2×2 matrix which satisfies the Schrodinger equation and meets the vanishing boundary condition at the clean edge. For a particular momentum k and energy E, not in the relation of $E = A\sin(k_x a)$, we will first find the eigenvectors and eigenvalues. Then $M^c_{(n)}$ will be constructed out of the eigenvectors so that it automatically satisfies the Schrodinger equation. To impose the vanishing boundary condition at $n = N$, we combine the four eigenvectors in a certain way such that $M^c_{(n)}$ is invertible. Explicitly, for 2×2 one spin section solution, let us assume that the four eigenvectors are the following:

$$\psi_1 = \begin{pmatrix} \alpha_1 \\ \\ \beta_1 \end{pmatrix}, \psi_2 = \begin{pmatrix} \alpha_2 \\ \\ \beta_2 \end{pmatrix}, \psi_3 = \begin{pmatrix} \alpha_3 \\ \\ \beta_3 \end{pmatrix}, \psi_4 = \begin{pmatrix} \alpha_4 \\ \\ \beta_4 \end{pmatrix} \tag{5.25}$$

with eigenvalues ρ_1, ρ_2, ρ_3, and ρ_4, respectively. Note that α_i and β_i are functions of Hamiltonian parameters given in section 5.3 and $i = 1, 2, 3, 4$ is not the layer index. Here we have four eigenvectors that are not parallel to each other. Then we can combine $\psi_{1,2}$ to build $|+\rangle = \begin{pmatrix} 1 & 1 \end{pmatrix}^T / \sqrt{2}$ and $|-\rangle = \begin{pmatrix} 1 & -1 \end{pmatrix}^T / \sqrt{2}$ vectors, and combine $\psi_{3,4}$ to build another set of $|+\rangle$ and $|-\rangle$, which are convenient choices for further manipulations. Explicitly, consider the following Schmidt decomposition:

$$\psi_j = \begin{pmatrix} \alpha_j \\ \\ \beta_j \end{pmatrix} = \frac{A_{+,j}}{\sqrt{2}} \begin{pmatrix} 1 \\ \\ 1 \end{pmatrix} + \frac{A_{-,j}}{\sqrt{2}} \begin{pmatrix} 1 \\ \\ -1 \end{pmatrix} \tag{5.26}$$

and define $\gamma_j = A_{+,j}/A_{-,j}$, which is a measure of how much a eigenvector ψ_j is close to $|+\rangle$. Through similar decompositions of other eigenvectors, we get the two ways of building the $|+\rangle$ and $|-\rangle$:

$$\frac{1}{\sqrt{2}} \begin{pmatrix} 1 \\ \\ 1 \end{pmatrix} = \frac{1}{\gamma_1 - \gamma_2} \left(\frac{1}{A_{-,1}} \psi_1 - \frac{1}{A_{-,2}} \psi_2 \right) \tag{5.27}$$

$$= \frac{1}{\gamma_3 - \gamma_4} \left(\frac{1}{A_{-,3}} \psi_3 - \frac{1}{A_{-,4}} \psi_4 \right) \tag{5.28}$$

and,

$$\frac{1}{\sqrt{2}} \begin{pmatrix} 1 \\ \\ -1 \end{pmatrix} = \frac{1}{1/\gamma_1 - 1/\gamma_2} \left(\frac{1}{A_{+,1}} \psi_1 - \frac{1}{A_{+,2}} \psi_2 \right) \tag{5.29}$$

$$= \frac{1}{1/\gamma_3 - 1/\gamma_4} \left(\frac{1}{A_{+,3}} \psi_3 - \frac{1}{A_{+,4}} \psi_4 \right) \tag{5.30}$$

Now, we are ready to construct $M^c_{(n=N+1)}$ at the last layer, which is zero 2×2 matrix :

$$M^c_{(n=N+1)} = \left[\begin{pmatrix} 1 \\ \\ 1 \end{pmatrix} - \begin{pmatrix} 1 \\ \\ 1 \end{pmatrix} \right] \begin{pmatrix} 1 & 1 \end{pmatrix} + \left[\begin{pmatrix} 1 \\ \\ -1 \end{pmatrix} - \begin{pmatrix} 1 \\ \\ -1 \end{pmatrix} \right] \begin{pmatrix} 1 & -1 \end{pmatrix}. \tag{5.31}$$

We put (5.27)-(5.28) in the first square bracket of (5.31), and put (5.29)-(5.30) in the second bracket. In this way, we construct the $M^c_{(n)}$-matrix with the vanishing boundary condition and invertible in the subsequent layers ($n \leq N$). Since each eigenvector propagates over the layers in a straightforward manner, $\psi_j(n) = \rho_j^{n-N}\psi_j(N)$, by propagating each eigenvector and plugging them into (5.26) back, we get the expression of n_{th} layer $M^c_{(n)}$-matrix in $|\pm\rangle\langle\pm|$ basis:

$$M^c_{(N+1-n)} = \begin{pmatrix} \frac{r_1\rho_1^n - r_2\rho_2^n}{r_1 - r_2} - \frac{r_3\rho_3^n - r_4\rho_4^n}{r_3 - r_4} & \frac{\rho_1^n - \rho_2^n}{r_1 - r_2} - \frac{\rho_3^n - \rho_4^n}{r_3 - r_4} \\ \\ \frac{\rho_1^n - \rho_2^n}{1/r_1 - 1/r_2} - \frac{\rho_3^n - \rho_4^n}{1/r_3 - 1/r_4} & \frac{\rho_1^n/r_1 - \rho_2^n/r_2}{1/r_1 - 1/r_2} - \frac{\rho_3^n/r_3 - \rho_4^n/r_4}{1/r_3 - 1/r_4} \end{pmatrix}_{\pm}. \tag{5.32}$$

where the index n is used to indicate the distance from the $(N+1)_{th}$ layer. In turn, we can obtain the transfer matrix following (5.14). Though the exact expression is available, some terms are negligible for a large width of system. Assuming eigenvalue ρ_1 and ρ_3 are larger than unity, we obtain a reduced expression for the transfer matrix between the first and n_{th} layer:

$$S_{(n+1)\leftarrow 1} = \frac{1}{(r_1 - r_3)} \begin{pmatrix} \rho_1^{-n} r_1 - \rho_3^{-n} r_3 & (\rho_1^{-n} - \rho_3^{-n}) \\ \\ r_1 r_3 (\rho_3^{-n} - \rho_1^{-n}) & \rho_3^{-n} r_1 - \rho_1^{-n} r_3 \end{pmatrix}_{\pm}, \tag{5.33}$$

which is reproduced in section 5.3.2. We want to emphasize that among three classified cases, the case (iii) (k, E) not on the dispersion is most relevant because in the presence of surface impurities, eigenenergies of the surface state are not identical to the ones of the

clean system.

5.6.2 Case (ii): $(k, E \neq 0) = (k_x, \pm A\mathbf{sin}(k_x a))$

For this case we have the following set of eigenvectors in general for $E = A\sin(k_x a)$:

$$\psi_1 = \begin{pmatrix} \alpha_1 \\ \\ \beta_1 \end{pmatrix}, \psi_2 = \begin{pmatrix} \alpha_2 \\ \\ \beta_2 \end{pmatrix}, \psi_3 = \frac{1}{\sqrt{2}} \begin{pmatrix} 1 \\ \\ 1 \end{pmatrix}, \psi_4 = \frac{1}{\sqrt{2}} \begin{pmatrix} 1 \\ \\ 1 \end{pmatrix} \tag{5.34}$$

where the eigenvalues ρ_3 and ρ_4 are less than unity. To construct a $M^c_{(n)}$-matrix with the vanishing boundary condition, we do Schmidt decompositions of ψ_1 and ψ_2 and construct $|-\rangle$ in two different ways:

$$\frac{1}{\sqrt{2}} \begin{pmatrix} 1 \\ \\ -1 \end{pmatrix} = \left(\frac{1}{A_{-,1}} \psi_1 - \frac{A_{+,1}}{A_{-,1}} \psi_3 \right) \tag{5.35}$$

$$= \left(\frac{1}{A_{-,2}} \psi_2 - \frac{A_{+,2}}{A_{-,2}} \psi_4 \right) \tag{5.36}$$

where $A_{\pm,j}$ is defined in (5.26). Next, we construct the $M^c_{(n)}$-matrix in the same way as before:

$$M^c_{(N+1-n)} = \begin{pmatrix} \rho_3^n - \rho_4^n & 0 \\ \\ r_1(\rho_1^n - \rho_3^n) - r_2(\rho_2^n - \rho_4^n) & \rho_1^n - \rho_2^n \end{pmatrix}_{\pm} . \tag{5.37}$$

Note that when $n = 0$, we get zero matrix $M^c_{(N+1)}$, as required from the boundary condition. The transfer matrix in the limit of large width N is:

$$\begin{aligned} S_{(n)\leftarrow(m)} &= M^c_{(n)}/M^c_{(m)} \\ &= \begin{pmatrix} \frac{\rho_3^n-\rho_4^n}{\rho_3^m-\rho_4^m} & 0 \\ \frac{(\rho_3^n-\rho_4^n)(-r_1\rho_1^m+r_2\rho_2^m)+(\rho_3^m-\rho_4^m)(r_1\rho_1^n-r_2\rho_2^n)}{(\rho_1^m-\rho_2^m)(\rho_3^m-\rho_4^m)} & \frac{\rho_1^n-\rho_2^n}{\rho_1^m-\rho_2^m} \end{pmatrix}_{\pm} . \end{aligned} \tag{5.38}$$

If (k_x, E) are on the other edge dispersion relation $E = -A\sin(k_x a)$, we have the following four eigenvectors:

$$\psi_1 = \begin{pmatrix} \alpha_1 \\ \\ \beta_1 \end{pmatrix}, \psi_2 = \begin{pmatrix} \alpha_2 \\ \\ \beta_2 \end{pmatrix}, \psi_3 = \frac{1}{\sqrt{2}} \begin{pmatrix} 1 \\ \\ -1 \end{pmatrix}, \psi_4 = \frac{1}{\sqrt{2}} \begin{pmatrix} 1 \\ \\ -1 \end{pmatrix} \tag{5.39}$$

where eigenvalues ρ_3 and ρ_4 are less then unity. We construct the vector $|-\rangle$ in two different ways using ψ_1 and ψ_2. Explicitly,

$$\frac{1}{\sqrt{2}} \begin{pmatrix} 1 \\ \\ 1 \end{pmatrix} = \left(\frac{1}{A_{+,1}}\psi_1 - \frac{A_{-,1}}{A_{+,1}}\psi_3 \right) \tag{5.40}$$

$$= \left(\frac{1}{A_{+,2}}\psi_2 - \frac{A_{-,2}}{A_{+,2}}\psi_4 \right) \tag{5.41}$$

The $M^c_{(n)}$-matrix satisfying the vanishing boundary condition at $n = N + 1$ is:

$$M^c_{(N+1-n)} = \begin{pmatrix} \rho_1^n - \rho_2^n & (\rho_1^n - \rho_3^n)/r_1 - (\rho_2^n - \rho_4^n)/r_2 \\ \\ 0 & \rho_3^n - \rho_4^n \end{pmatrix}_{\pm} . \tag{5.42}$$

Finally, the transfer matrix that connects the wavefunctions on layer n and m is:

$$\begin{aligned} S_{(n)\leftarrow(m)} &= M_n/M_m \\ &= \begin{pmatrix} \frac{\rho_1^n-\rho_2^n}{\rho_1^m-\rho_2^m} & \frac{(\rho_3^n-\rho_4^n)(-\rho_1^m/r_1+\rho_2^m/r_2)+(\rho_3^m-\rho_4^m)(\rho_1^n/r_1-\rho_2^n/r_2)}{(\rho_1^m-\rho_2^m)(\rho_3^m-\rho_4^m)} \\ 0 & \frac{\rho_3^n-\rho_4^n}{\rho_3^m-\rho_4^m} \end{pmatrix}_{\pm}. \end{aligned} \tag{5.43}$$

5.6.3 Case (i): $(k, E) = (0, 0)$

At zero energy, the top and bottom edge states share the same momentum $k_x = 0$ and the four eigenvectors of the Schrodinger equation are:

$$\psi_1 = \frac{1}{\sqrt{2}}\begin{pmatrix} 1 \\ \\ -1 \end{pmatrix}, \psi_2 = \frac{1}{\sqrt{2}}\begin{pmatrix} 1 \\ \\ -1 \end{pmatrix}, \psi_3 = \frac{1}{\sqrt{2}}\begin{pmatrix} 1 \\ \\ 1 \end{pmatrix}, \psi_4 = \frac{1}{\sqrt{2}}\begin{pmatrix} 1 \\ \\ 1 \end{pmatrix} \tag{5.44}$$

The eigenvalues are $\rho_1 = \rho e^{i\theta}$ with $\rho > 1$, $\rho_2 = \rho_1^*$, $\rho_3 = 1/\rho_1$, and $\rho_4 = 1/\rho_1^*$. In this case we can directly construct the $M_{(n)}^c$-matrix satisfying the vanishing boundary condition at $n = N + 1$:

$$M_{(N+1-n)}^c = (\rho_1^n - \rho_3^n)\frac{1}{2}\begin{pmatrix} 1 & 1 \\ \\ 1 & 1 \end{pmatrix} - (\rho_2^n - \rho_4^n)\frac{1}{2}\begin{pmatrix} 1 & -1 \\ \\ -1 & 1 \end{pmatrix} \tag{5.45}$$

And the following transfer matrix is:

$$S_{(n)\leftarrow(N)} = \frac{\sin(n\theta)}{2\sin(N\theta)}\left[\rho^{n-N}\begin{pmatrix} 1 & 0 \\ \\ 0 & 0 \end{pmatrix}_{\pm} + \rho^{-n+N}\begin{pmatrix} 0 & 0 \\ \\ 0 & 1 \end{pmatrix}_{\pm}\right] \tag{5.46}$$

which diverges in the $N \to \infty$ limit.

Bibliography

[1] D. Pesin and A. H. MacDonald, Nature Materials **11**, 409 (2012), ISSN 1476-1122.

[2] P. Ghaemi, R. S. K. Mong, and J. E. Moore, Physical Review Letters **105**, 166603 (2010).

[3] N. H. Lindner, G. Refael, and F. von Oppen, arXiv:1403.0010 [cond-mat] (2014).

[4] J. Alicea, Reports on Progress in Physics **75**, 076501 (2012), ISSN 0034-4885.

[5] M. König, S. Wiedmann, C. Brüne, A. Roth, H. Buhmann, L. W. Molenkamp, X.-L. Qi, and S.-C. Zhang, Science **318**, 766 (2007), ISSN 0036-8075, 1095-9203, PMID: 17885096.

[6] J. G. Checkelsky, Y. S. Hor, M.-H. Liu, D.-X. Qu, R. J. Cava, and N. P. Ong, Physical Review Letters **103**, 246601 (2009).

[7] I. Affleck, Physical Review Letters **57**, 1048 (1986).

[8] D. J. P. Morris, D. A. Tennant, S. A. Grigera, B. Klemke, C. Castelnovo, R. Moessner, C. Czternasty, M. Meissner, K. C. Rule, J.-U. Hoffmann, et al., Science **326**, 411 (2009), ISSN 0036-8075, 1095-9203, PMID: 19729617.

[9] G. Rosenberg and M. Franz, Physical Review B **82**, 035105 (2010).

[10] J. T. Barreiro, M. Müller, P. Schindler, D. Nigg, T. Monz, M. Chwalla, M. Hennrich, C. F. Roos, P. Zoller, and R. Blatt, Nature **470**, 486 (2011), ISSN 0028-0836.

[11] R. S. K. Mong and V. Shivamoggi, Physical Review B **83**, 125109 (2011).

[12] C. L. Kane and E. J. Mele, Physical Review Letters **95**, 226801 (2005).

[13] J. E. Moore and L. Balents, Physical Review B **75**, 121306 (2007).

[14] C. L. Kane and E. J. Mele, Physical Review Letters **95**, 146802 (2005).

[15] A. M. Essin, J. E. Moore, and D. Vanderbilt, Physical Review Letters **102**, 146805 (2009).

[16] P. a. M. Dirac, Proceedings of the Royal Society of London. Series A **133**, 60 (1931), ISSN 1364-5021, 1471-2946.

[17] X.-L. Qi, R. Li, J. Zang, and S.-C. Zhang, Science **323**, 1184 (2009), ISSN 0036-8075, 1095-9203, PMID: 19179491.

[18] C.-Y. Hou, C. Chamon, and C. Mudry, Physical Review Letters **98**, 186809 (2007).

[19] J. Moore, Nature Physics **5**, 378 (2009), ISSN 1745-2473.

[20] D. J. Thouless, M. Kohmoto, M. P. Nightingale, and M. den Nijs, Physical Review Letters **49**, 405 (1982).

[21] G. Schubert, H. Fehske, L. Fritz, and M. Vojta, Physical Review B **85**, 201105 (2012).

[22] S. Ryu and K. Nomura, Physical Review B **85**, 155138 (2012).

[23] S.-i. Tomonaga, Progress of Theoretical Physics **5**, 544 (1950), ISSN 0033-068X, 1347-4081.

[24] J. M. Luttinger, Journal of Mathematical Physics **4**, 1154 (1963), ISSN 0022-2488, 1089-7658.

[25] F. D. M. Haldane, Journal of Physics C: Solid State Physics **14**, 2585 (1981), ISSN 0022-3719.

[26] X. G. Wen, Physical Review B **41**, 12838 (1990).

[27] C. L. Kane and M. P. A. Fisher, Physical Review Letters **68**, 1220 (1992).

[28] S. Das Sarma, M. Freedman, and C. Nayak, Physical Review Letters **94**, 166802 (2005).

[29] A. Y. Kitaev, Physics-Uspekhi **44**, 131 (2001), ISSN 1063-7869.

[30] S.-S. Lee, S. Ryu, C. Nayak, and M. P. A. Fisher, Physical Review Letters **99**, 236807 (2007).

[31] W. Bishara and C. Nayak, Physical Review B **77**, 165302 (2008).

[32] B. I. Halperin, A. Stern, I. Neder, and B. Rosenow, Physical Review B **83**, 155440 (2011).

[33] J. G. Analytis, R. D. McDonald, S. C. Riggs, J.-H. Chu, G. S. Boebinger, and I. R. Fisher, Nature Physics **6**, 960 (2010), ISSN 1745-2473.

[34] H. Peng, K. Lai, D. Kong, S. Meister, Y. Chen, X.-L. Qi, S.-C. Zhang, Z.-X. Shen, and Y. Cui, Nature Materials **9**, 225 (2010), ISSN 1476-1122.

[35] J.-P. Cleuziou, W. Wernsdorfer, V. Bouchiat, T. Ondarçuhu, and M. Monthioux, Nature Nanotechnology **1**, 53 (2006), ISSN 1748-3387.

[36] D. Hsieh, Y. Xia, D. Qian, L. Wray, J. H. Dil, F. Meier, J. Osterwalder, L. Patthey, J. G. Checkelsky, N. P. Ong, et al., Nature **460**, 1101 (2009), ISSN 0028-0836.

[37] L. A. Wray, S.-Y. Xu, Y. Xia, D. Hsieh, A. V. Fedorov, Y. S. Hor, R. J. Cava, A. Bansil, H. Lin, and M. Z. Hasan, Nature Physics **7**, 32 (2011), ISSN 1745-2473.

[38] T. Zhang, P. Cheng, X. Chen, J.-F. Jia, X. Ma, K. He, L. Wang, H. Zhang, X. Dai, Z. Fang, et al., Physical Review Letters **103**, 266803 (2009).

[39] W.-C. Lee and C. Wu, Physical Review Letters **103**, 176101 (2009).

[40] W. J. de Haas, J. de Boer, and G. J. van dën Berg, Physica **1**, 1115 (1934), ISSN 0031-8914.

[41] J. Kondo, Progress of Theoretical Physics **32**, 37 (1964), ISSN 0033-068X, 1347-4081.

[42] M. Grobis, I. G. Rau, R. M. Potok, H. Shtrikman, and D. Goldhaber-Gordon, Physical Review Letters **100**, 246601 (2008).

[43] P. W. Anderson, Phys. Rev. **109**, 1492 (1958).

[44] K. G. Wilson and J. Kogut, Physics Reports **12**, 75 (1974), ISSN 0370-1573.

[45] H. C. Manoharan, C. P. Lutz, and D. M. Eigler, Nature **403**, 512 (2000), ISSN 0028-0836.

[46] G. A. Fiete and E. J. Heller, Reviews of Modern Physics **75**, 933 (2003).

[47] K. v. Klitzing, G. Dorda, and M. Pepper, Physical Review Letters **45**, 494 (1980).

[48] Q. Niu, D. J. Thouless, and Y.-S. Wu, Physical Review B **31**, 3372 (1985).

[49] E. Abrahams, P. W. Anderson, D. C. Licciardello, and T. V. Ramakrishnan, Physical Review Letters **42**, 673 (1979).

[50] D. Vollhardt and P. Wölfle, Physical Review Letters **45**, 842 (1980).

[51] C. W. J. Beenakker, Reviews of Modern Physics **69**, 731 (1997).

[52] K. B. Efetov, International Journal of Modern Physics B **24**, 1756 (2010), ISSN 0217-9792.

[53] J. G. Checkelsky, Y. S. Hor, M.-H. Liu, D.-X. Qu, R. J. Cava, and N. P. Ong, Physical Review Letters **103**, 246601 (2009).

[54] J. Li, R.-L. Chu, J. K. Jain, and S.-Q. Shen, Physical Review Letters **102**, 136806 (2009).

[55] H.-M. Guo, G. Rosenberg, G. Refael, and M. Franz, Physical Review Letters **105**, 216601 (2010).

[56] M. Ma and P. A. Lee, Physical Review B **32**, 5658 (1985).

[57] A. V. Balatsky, M. I. Salkola, and A. Rosengren, Physical Review B **51**, 15547 (1995).

[58] A. Abrikosov and L. Gor'Kov, Zhur. Eksptl'. i Teoret. Fiz. **35** (1958).

[59] K. W. Kim, T. Pereg-Barnea, and G. Refael, Physical Review B **89**, 085117 (2014).

[60] P. W. Anderson, Rev. Mod. Phys. **50**, 191 (1978).

[61] E. Abrahams, *50 years of Anderson localization*, vol. 24 (World Scientific, 2010).

[62] F. Evers and A. D. Mirlin, Rev. Mod. Phys. **80**, 1355 (2008).

[63] P. Anderson, Journal of Physics and Chemistry of Solids **11**, 26 (1959).

[64] P. Anderson, *Proceedings of the Eighth Conference on Low Temperature Physics* (Univ. Toronto Press, Toronto, 1961).

[65] A. Abrikosov and L. Gor'kov, Sov. Phys.-JETP (Engl. Transl.);(United States) **9** (1959).

[66] D. Markowitz and L. P. Kadanoff, Phys. Rev. **131**, 563 (1963).

[67] A. Larkin, JETP Lett **2**, 130 (1965).

[68] C. W. Groth, M. Wimmer, A. R. Akhmerov, J. Tworzydło, and C. W. J. Beenakker, Phys. Rev. Lett. **103**, 196805 (2009).

[69] J. Kondo, Progress of theoretical physics **32**, 37 (1964).

[70] A. C. Hewson, *The Kondo problem to heavy fermions*, 2 (Cambridge university press, 1997).

[71] I. m. c. Adagideli, P. M. Goldbart, A. Shnirman, and A. Yazdani, Phys. Rev. Lett. **83**, 5571 (1999).

[72] D. Noid, M. Koszykowski, and R. Marcus, The Journal of Chemical Physics **71**, 2864 (1979).

[73] D. A. Stone, C. A. Downing, and M. E. Portnoi, Phys. Rev. B **86**, 075464 (2012).

[74] P. Carmier and D. Ullmo, Phys. Rev. B **77**, 245413 (2008).

[75] J. Knoll and R. Schaeffer, Annals of Physics **97**, 307 (1976).

[76] A. V. Balatsky, I. Vekhter, and J.-X. Zhu, Rev. Mod. Phys. **78**, 373 (2006).

[77] M. Srednicki, Quantum Field Theory, by Mark Srednicki, pp. 664. Cambridge University Press, January 2007. ISBN-10:. ISBN-13: **1** (2007).

[78] L. Fu and C. L. Kane, Physical Review B **76**, 045302 (2007).

[79] L. Fu, C. L. Kane, and E. J. Mele, Physical Review Letters **98**, 106803 (2007).

[80] Z. Wang, X.-L. Qi, and S.-C. Zhang, New Journal of Physics **12**, 065007 (2010), ISSN 1367-2630.

[81] X.-L. Qi, T. L. Hughes, and S.-C. Zhang, Physical Review B **78**, 195424 (2008).

[82] H. Steinberg, D. R. Gardner, Y. S. Lee, and P. Jarillo-Herrero, Nano Letters **10**, 5032 (2010), ISSN 1530-6984.

[83] N. P. Butch, K. Kirshenbaum, P. Syers, A. B. Sushkov, G. S. Jenkins, H. D. Drew, and J. Paglione, Physical Review B **81**, 241301 (2010).

[84] D. Hsieh, D. Qian, L. Wray, Y. Xia, Y. S. Hor, R. J. Cava, and M. Z. Hasan, Nature **452**, 970 (2008), ISSN 0028-0836.

[85] M. Neupane, S.-Y. Xu, L. A. Wray, A. Petersen, R. Shankar, N. Alidoust, C. Liu, A. Fedorov, H. Ji, J. M. Allred, et al., Physical Review B **85**, 235406 (2012).

[86] D. L. Bergman and G. Refael, Physical Review B **82**, 195417 (2010).

[87] D. L. Bergman, Physical Review Letters **107**, 176801 (2011).

[88] M. Barkeshli and X.-L. Qi, Physical Review Letters **107**, 206602 (2011).

[89] A. Karch, Physical Review B **83**, 245432 (2011).

[90] R. Shindou and S. Murakami, Physical Review B **79**, 045321 (2009).

[91] R. Shindou, R. Nakai, and S. Murakami, New Journal of Physics **12**, 065008 (2010), ISSN 1367-2630.

[92] B. Leung and E. Prodan, Physical Review B **85**, 205136 (2012).

[93] E. Prodan, Physical Review B **83**, 195119 (2011).

[94] T. A. Loring and M. B. Hastings, EPL (Europhysics Letters) **92**, 67004 (2010), ISSN 0295-5075.

[95] M. B. Hastings and T. A. Loring, Annals of Physics **326**, 1699 (2011), ISSN 0003-4916.

[96] J. S. Meyer and G. Refael, Physical Review B **87**, 104202 (2013).

[97] C. W. Groth, M. Wimmer, A. R. Akhmerov, J. Tworzydło, and C. W. J. Beenakker, Physical Review Letters **103**, 196805 (2009).

[98] D. L. Bergman and G. Refael, Physical Review B **87**, 024202 (2013).

[99] F. D. M. Haldane, Physical Review Letters **61**, 2015 (1988).

[100] R. Landauer, IBM Journal of Research and Development **1**, 223 (1957), ISSN 0018-8646.

[101] R. Landauer, Philosophical Magazine **21**, 863 (1970), ISSN 0031-8086.

[102] M. Büttiker, Physical Review B **38**, 12724 (1988).

[103] D. S. Fisher and P. A. Lee, Physical Review B **23**, 6851 (1981).

[104] S. Datta, *Electronic Transport in Mesoscopic Systems* (Cambridge University Press, 1997), ISBN 9780521599436.

[105] K. W. Kim, I. Klich, and G. Refael, Physical Review B **89**, 104204 (2014).

[106] R. Tsu and L. Esaki, Applied Physics Letters **22**, 562 (2003).

[107] L. Fu and C. L. Kane, Phys. Rev. B **74**, 195312 (2006).

[108] J. E. Moore and L. Balents, Phys. Rev. B **75**, 121306 (2007).

[109] T. Fukui, T. Fujiwara, and Y. Hatsugai, Journal of the Physical Society of Japan **77** (2008).

[110] R. Roy, Phys. Rev. B **79**, 195321 (2009).

[111] Z. Wang, X.-L. Qi, and S.-C. Zhang, New Journal of Physics **12**, 065007 (2010).

[112] A. Stern, Annals of Physics **323**, 204 (2008).

[113] D. C. Tsui, H. L. Stormer, and A. C. Gossard, Phys. Rev. Lett. **48**, 1559 (1982).

[114] K. v. Klitzing, G. Dorda, and M. Pepper, Phys. Rev. Lett. **45**, 494 (1980).

[115] C. Xu and J. E. Moore, Phys. Rev. B **73**, 045322 (2006).

[116] C. Wu, B. A. Bernevig, and S.-C. Zhang, Phys. Rev. Lett. **96**, 106401 (2006).

[117] V. Cheianov and L. I. Glazman, Phys. Rev. Lett. **110**, 206803 (2013).

[118] D. L. Bergman and G. Refael, Phys. Rev. B **82**, 195417 (2010).

[119] A. Junck, K. W. Kim, D. L. Bergman, T. Pereg-Barnea, and G. Refael, Phys. Rev. B **87**, 235114 (2013).

[120] T. Brandes and S. Kettemann, *Anderson Localization and Its Ramifications: Disorder, Phase Coherence, and Electron Correlations*, vol. 630 (Springer, 2003).

[121] F. Delyon, H. Kunz, and B. Souillard, Journal of Physics a-Mathematical and General **16**, 25 (1983).

[122] K. Efetov, *Supersymmetry in disorder and chaos* (Cambridge University Press, 1999).

[123] F. Wegner, Zeitschrift Fur Physik B-Condensed Matter **35**, 207 (1979).

[124] F. Iglói and C. Monthus, Physics reports **412**, 277 (2005).

[125] A. D. Stone and A. Szafer, IBM Journal of Research and Development **32**, 384 (1988), ISSN 0018-8646.

[126] D. Thouless, Journal of Physics C: Solid State Physics **5**, 77 (1972).

[127] T. Fukuhara, P. Schauß, M. Endres, S. Hild, M. Cheneau, I. Bloch, and C. Gross, arXiv preprint arXiv:1305.6598 (2013).

[128] E. Abrahams and M. J. Stephen, Journal of Physics C: Solid State Physics **13**, L377 (1980), ISSN 0022-3719.

[129] P. W. Anderson, D. J. Thouless, E. Abrahams, and D. S. Fisher, Physical Review B **22**, 3519 (1980).

[130] N. Kumar, Physical Review B **31**, 5513 (1985).

[131] P. D. Kirkman and J. B. Pendry, Journal of Physics C: Solid State Physics **17**, 4327 (1984), ISSN 0022-3719.

[132] A. D. Stone, J. D. Joannopoulos, and D. J. Chadi, Physical Review B **24**, 5583 (1981).

[133] B. S. Andereck and E. Abrahams, Journal of Physics C: Solid State Physics **13**, L383 (1980).

[134] P. A. Mello, Journal of Mathematical Physics **27**, 2876 (1986), ISSN 0022-2488, 1089-7658.

[135] J. Sak and B. Kramer, Physical Review B **24**, 1761 (1981).

[136] A. D. Stone, D. C. Allan, and J. D. Joannopoulos, Physical Review B **27**, 836 (1983).

[137] B. Kramer and A. MacKinnon, Reports on Progress in Physics **56**, 1469 (1993), ISSN 0034-4885.

[138] J. B. Pendry, Advances in Physics **43**, 461 (1994).

[139] P. A. Lee, A. D. Stone, and H. Fukuyama, Physical Review B **35**, 1039 (1987).

[140] C. W. J. Beenakker, Reviews of Modern Physics **69**, 731 (1997).

[141] P. Erdös and R. Herndon, Advances in Physics **31**, 65 (1982).

[142] A. Abrikosov, Solid State Communications **37**, 997 (1981).

[143] C. de C. Chamon, D. E. Freed, S. A. Kivelson, S. L. Sondhi, and X. G. Wen, Phys. Rev. B **55**, 2331 (1997).

[144] D. E. Feldman and A. Kitaev, Phys. Rev. Lett. **97**, 186803 (2006).

[145] D. E. Feldman, Y. Gefen, A. Kitaev, K. T. Law, and A. Stern, Phys. Rev. B **76**, 085333 (2007).

[146] A. R. Akhmerov, J. Nilsson, and C. W. J. Beenakker, Phys. Rev. Lett. **102**, 216404 (2009).

[147] W. Bishara and C. Nayak, Physical Review B **77**, 165302 (2008).

[148] G. Metalidis and P. Bruno, Physical Review B **72**, 235304 (2005).